Process Mapping and Optimization of Titanium Parts Made by Binder Jetting Additive Manufacturing

by

Evan Wheat

A thesis
presented to the University of Waterloo
in fulfillment of the
thesis requirement for the degree of
Master of Applied Science
in
Mechanical and Mechatronics Engineering

Waterloo, Ontario, Canada, 2018

Abstract

Additive manufacturing (AM) has recently seen an increase in adoption outside of its traditional role of rapid prototyping and is being used more and more for the production of functional components. The increased adoption is due in part to better systems and a better understanding of the AM process. Binder jetting additive manufacturing (BJAM), however, has seen significantly less adoption compared to other AM technologies and that is likely because there has been comparatively less work done on improving and understanding the process. For BJAM to see more widespread use, a more thorough understanding of the process both during printing and sintering is required.

One area where BJAM can see more substantive adoption is in the medical and dental fields. Porous parts, especially implants, can have highly beneficial properties compared to solid parts. However, the porosity in these components needs to be tailored depending on the application. BJAM allows for this level of control, as the density of sintered parts can be controlled anywhere from around 50% to nearly 100%. Tailoring these properties requires controlling the density of the green parts (through printing) and subsequently the final parts (through sintering), as many part properties are directly linked to density. Previous studies in the group focused on the printing of commercially pure titanium components. This thesis adds onto that work by examining the effects of powder sizes and sintering on green and final densities.

Five sample types were produced to evaluate the sintering process. The powder size distribution was varied between samples while the printing parameters were kept fixed. This was done in order to isolate the effects of the powder size distribution from the printing parameters. Two mono-modal distributions were used (45-106μm and 106-150μm) as well as three bi-modal distributions (0-45μm/45-106μm, 0-45μm/106-150μm and 45-106μm/106-150μm).

The completed work focuses on two main areas. The first area is more traditional sinter theory and sinter structure analysis, which is done to gain insight into how different particle sizes and the specific powder systems seen in BJAM parts affects the sintering process. This analysis is done using computed tomography (CT), where both the green and sintered parts are scanned and compared. Four major features are evaluated from the CT scans, which are bulk porosity, porosity per layer, particle size and pore size. Parts are sintered at 1000℃ and 1400℃ to produce parts that undergo only non-densifying and densifying sintering respectively.

From the results, it was found that samples with the fine powder additions (0-45μm) sintered with substantially higher levels of densification (at both 1000℃ and 1400℃) compared to the other powder types comprised of larger particles. All of the samples showed a periodic density change corresponding to the height of the printed layers. Parts were found to be the most dense within a layer and least dense at the layer interfaces. After sintering, the relative density variation was unchanged for samples with larger particles and exacerbated for samples made with finer particles. Samples with the finer particles were able to achieve bulk densities of 82.7% and 84.6% when sintered at 1400°C. However, the density fluctuated from nearly 100% within layers to approximately 60% at the layer interfaces.

The second area of focus is on the development of a tool to predict the final density of sintered parts. The development of this tool drew heavily from existing information on the sintering of powder metallurgy components. From a literature review, the master sinter curve (MSC), a powder metallurgy technique based on the combined stage sinter theory, was deemed to be an excellent basis for developing a predictive tool. The MSC is constructed using experimental dilatometry results, avoiding the need for a more comprehensive analysis of the powders used. To generate MSCs for each powder type, samples were sintered in a dilatometer from room temperature up to 1550°C at various heating rates and then cooled quickly. The dilatometry results are then processed to create MSCs.

Reliable MSCs could not be made from the dilatometry results. The specific push-rod dilatometry analysis that was used as part of this work (required due to the system configuration) gave poor shrinkage results. These results could not be used to make good quality MSCs and prevented the generation of the predictive tool. However, since the general process has already been made as part of this work, only new dilatometry measurements are required to be able to create proper MSCs.

Acknowledgements

I would like to thank all of those who helped me throughout my thesis work.

First, I would like to thank my co-supervisors Dr. Mihaela Vlasea and Dr. Ehsan Toyserkani for all of their support and guidance during this thesis. I deeply appreciate the confidence you have in me as well as the freedom you gave me during my research. Without you I never would have had this opportunity to not only complete my thesis, but to also see our lab grow into what it is today.

I would like to acknowledge James Hinebaugh and Michael George for all of the assistance they provided for the CT scanning and analysis of my samples. I would also like to acknowledge the help I had from Allan Rogalsky, Ehsan Marzbanrad and Sagar Patel during this work.

I would particularly like to thank Mark Whitney for running my many samples on the dilatometer. With three system breakdowns and seemingly endless correction runs, I still managed to get my data in time.

I would also like to thank both Phil Meszaros and Andre Bodo for putting up with me while I avoided working on and writing this.

Finally, I would like to thank my family for their unending support and encouragement.

Table of Contents

List of Tables

List of Figures

List of Abbreviations

3D Three-dimensional

AM Additive Manufacturing

BCC Body Centered Cubic

BJAM Binder Jetting Additive Manufacturing

CP Commercially Pure

CT Computed Tomography

CTE Coefficient of Thermal Expansion

DED Directed Energy Deposition

DIL Dilatometry

DSC Differential Scanning Calorimetry

FDM Fused Deposition Modeling

HCP Hexagonal Close-packed

MIP Maximum Intensity Projection

MSC Master Sinter Curve

MSP Master Sinter Parameter

MSS Master Sinter Surface

PBBJ Powder-bed Binder Jetting

PBF Powder Bed Fusion

PMMA Poly(methyl methacrylate)

PVA Polyvinyl-alcohol

RMSE Root Mean Square Error

ROI Region of Interest

SLA Vat Photopolymerization

STL Stereolithography

List of Symbols

α Hexagonal close-packed alpha phase of titanium

β Body centered cubic beta phase of titanium

α_l Coefficient of thermal expansion

ρ Density

ρ_r Relative Density

ρ_f Final relative Density

ρ_0 Initial relative Density

D_b Coefficient of grain boundary diffusion

$\delta L_b/2$ DeHoff model - area of diffusion available for grain boundary diffusion

S^b DeHoff model - area at the base of the pyramid representing a portion of a single grain

A_v DeHoff model - area of diffusion available for volumetric diffusion

$\bigtriangledown\mu$ DeHoff Model - chemical gradient of potential for diffusion

K_h DeHoff model - curvature at the neck

λ DeHoff model - maximum diffusion distance

C_a DeHoff model - Geometric scaling parameter for the area at the base of the pyramid

C_b DeHoff model - Geometric scaling parameter for the grain boundary area for diffusion

C_λ DeHoff model - Geometric scaling parameter for maximum diffusion distance

C_h DeHoff model - Geometric scaling parameter for pyramidal height

C_k DeHoff model - Geometric scaling parameter for surface curvature

C_v DeHoff model - Geometric scaling parameter for the volumetric area for diffusion

α_p DeHoff model - Constant of proportionality relating the gradient of the chemical potential for diffusion and the maximum diffusion distance

h DeHoff model - height of the pyramid representing a portion of a single grain

Θ_{iavg} Average master sinter parameter values calculated from dilatometry runs

Θ_i Master sinter parameter predicted by the sigmoidal fitting curve

N number of dilatometry runs

D_v Coefficient of volumetric diffusion

G Mean grain (or particle) diameter

a Initial relative density used for Sigmoidal function fitting

b Sigmoidal fitting constant determined using the Newton-Rhapson method

c Sigmoidal fitting constant determined using the Newton-Rhapson method

κ Surface curvature between two particles

Γ_b Geometric scaling factor for boundary diffusion

δ Grain boundary thickness

Γ_v Geometric scaling factor for volumetric diffusion

γ Capillary stress in a sinter neck between two particles

k Boltzmann constant

L Length - specifically a unit length in a powder system

L_0	Initial length - specifically of a unit length in a powder system
D_0	Diffusion coefficient in the master sinter curve
Φ	Functional value representing the material geometrical parameters of the powder system
Θ	Master sinter parameter representing the work of sintering
Ω	Atomic volume
D_{b0}	Pre-exponential of the coefficient of grain boundary diffusion
D_{v0}	Pre-exponential of the coefficient of volumetric diffusion
Q	Apparent activation energy of the sintering process
Q_b	Activation energy for grain boundary diffusion
Q_v	Activation energy for volumetric diffusion
R	Universal gas constant
$SA : V$	Surface area to volume ratio
σ	Sintering stress developed in a sinter neck between two particles
T	Absolute temperature in Kelvin
t	Time

Chapter 1

Introduction

Additive manufacturing (AM) has recently seen a significant amount growth in both its use and capabilities, with an increased adoption in industrial, commercial and consumer markets. Though there is some variability between processes, the core concept for all AM technologies is very similar. All processes begin with a three-dimensional (3D) model of a part or assembly. This model is then sliced vertically (in relation to the AM system) into thin layers. Each layer is converted into an image or tool path geometry, each corresponding to the layer of the part, which is subsequently sent to an AM system. Each layer is printed, deposited, scanned, etc. until the entire part has been completed. There are a few major benefits to this layer-by-layer build approach. The first is that there is little to no material waste since, apart from support structures, the only material consumed during the build process is that which actually makes up the part. In theory this should reduce the raw material costs of the part. Unfortunately this is not always true since materials for AM systems can be significantly more expensive than those used in traditional processes [1, 2]. Another benefit is that there is no specific tooling required to make the part. Forged, cast and even highly complex machined components all require some form of tooling to be made to produce the parts. Since AM does not require this tooling, those costs are negated. In addition, the lead time to production can be shortened since tooling does not need to be designed, produced and delivered. The final major benefit of AM is the ability to create exceptionally complex parts that could not be made using traditional means. Released from typical design constraints, previously impossible shapes can be made. Design freedom also allows designers to reduce the number of parts in an assembly, or even refine them into a single part, since the ability to machine, forge, cast, etc. does not need to be considered.

One of the major categories of AM is binder jet additive manufacturing (BJAM). BJAM, also referred to as 3D printing and powder-bed binder-jet (PBBJ) AM, was developed at the Massachusetts Institute of Technology in the early 1990's, with the technology being patented in 1993 [3]. The other categories of AM include vat photopolymerization (typically referred to as SLA), fused deposition modeling (FDM), material jetting, powder bed fusion (PBF), sheet lamination and directed energy deposition (DED). All of the processes are similar in concept, in that the part is built up sequentially, with features being added by adding material, rather than removing material.

In BJAM, the layer slices from the CAD file are converted into images. These images are printed onto a powder bed, typically using a ink jet print head, with a liquid-state binder. This binder consolidates the powder within and between layers. Once the printing is done, the part can be used as-is, cured or sintered. One major benefit BJAM has over other processes is that a system can be deployed in various applications for manufacturing metallic, ceramic and polymer parts.

The SLA and PBF technologies behave in a very similar manner, with some minor variations. In both, the sliced layers are converted into tool-paths for a laser to scan. The laser scans over material, solidifying it into a structure, then more material is spread over and subsequent layers are built up. The only difference between the technologies are the lasers and materials. In SLA, the material is a photopolymer resin and uses a relatively low power ultra-violet laser. In PBF, the material is powdered polymeric or metallic materials and typically uses a relatively high power laser or electron beam.

FDM and DED are also somewhat similar in concept. For both, the layer is converted into a tool-path that a deposition head follows. Material is deposited by the head as it moves over the tool-path, building up the part. In FDM a deposition head will extrude a heated polymeric filament that fuses to adjacent material. In DED a deposition head will extrude a metallic wire or spray metallic powder into a melt pool that is generated either by a laser or electron beam.

Sheet lamination is the most unique of all of the technologies. During the process, the geometry of the layer boundaries is applied to a sheet. The sheets themselves are usually either paper or thin gauge sheet metal. The sheets are then bonded together, with the excess material (defined by the previously applied layer boundaries) removed afterwards.

Material jetting is the AM process most similar to BJAM. During printing, the layer is converted into an image and sent to a print head. The material jetting system will then deposit photopolymeric resin on a substrate to build up a part. One main difference between the material jetting and BJAM techniques is that there is no powder bed used in material jetting.

Regardless of the specific technology used, a major reason many companies are apprehensive to purchase an AM system is that they are expensive. One benefit of BJAM systems is that they usually cost significantly less than other systems that can produce metallic parts. In addition to system cost, operating costs are lower as well. BJAM systems tend to consume comparatively little power, which reduces electricity costs [4]. BJAM systems do not operate at elevated temperatures, meaning no complex atmospheric control is required during production. This reduced system and operating cost lowers the barrier to entry significantly, and makes the adoption of the process a much easier proposition. The other major benefit to BJAM is the ability to produce large parts. PBF systems have restrictive build sizes and can take significantly longer than BJAM to make parts of any appreciable size [5]. BJAM can be scaled to as large a size as necessary without any real change to the system design. The process is also comparatively fast, with large parts able to be printed in a matter of hours [5].

BJAM is similar to other AM technologies in that it has historically been used only for the production of non-functional prototype parts. These parts are aesthetically representative, while not having the same functional properties (mechanical, chemical, electrical, etc.) of the actual component. While the production of prototypes is useful, AM processes are capable of producing a wide range of functional components. This shift to functional part production has been facilitated by a greater understanding of the materials and processes involved during AM fabrication and how they affect the final components. This in turn has made the AM processes more stable, controllable and predictable. Unfortunately, BJAM has seen considerably less research and development compared to other AM processes. BJAM has not seen the same expansion in the range of materials and process parameters available for the production of parts compared to other technologies.

In addition to a lack of process parameters and tools to predict final part properties, BJAM has been hindered due to issues surrounding the porosity that is inherent to its parts. Minimizing porosity has been a significant area of interest in AM, especially in PBF and DED. While porosity is highly desirable in many applications such as medical [6, 7], dental [8, 9], light-weighting [5], filtering [10] and many others, it is detrimental in many industrial, load-bearing components. Regardless of whether or not porosity is beneficial or detrimental, it needs to be controlled to ensure part properties are optimal for the desired application. Without a means to control porosity or predict final part properties, BJAM will continue to see lower levels of industrial adoption for the production of functional components.

1.1 Problem Statement

Though BJAM is a highly viable and versatile technology that can be used for the production of functional components, it is hindered by a lack of process parameters and predictive tools that allow for full control of the manufacturing process. For BJAM to see more significant adoption there must be some method or tool that one can use to predict part properties based on process inputs. This method or tool should also work in reverse, allowing one to derive the process inputs from desired part properties. In addition, this tool must be simple and cost-effective to both develop and deploy, otherwise it will not be easily adopted in risk and cost-adverse industries.

1.2 Motivation

The motivation behind this work is the desire to see a more widespread industrial adoption of BJAM, with a direct application in fabrication of biomedical titanium bone and dental augmentation segments. The BJAM process affords many benefits such as reduced material waste, design freedom and the ability to produce low-cost custom parts. In those fields, components are made of expensive bio-compatible materials and would see a great impact in reducing material waste. Many medical implants [7, 6] or dental restorations [9, 11] could benefit from a more bio-mimetic design strategy, but currently cannot due to parts being too difficult or expensive to produce. In addition, it is the medical and dental fields that can take the most advantage of custom parts as each application, namely each patient, is unique. AM enables anatomically correct shapes that can better fit the patient, with custom internal lattice or porous architecture and mechanical properties that mimic natural function. This could enable both higher patient satisfaction and patient outcomes, similar to benefits seen in porous orthopaedic implants [7]. Being able to predict final part properties is critical to manufacture such parts with a high degree of repeatability and accuracy, as well as to enable fast adoption of BJAM technologies in this field.

1.3 Objective and Outline

The scope of this thesis is focused on two major objectives. The first objective is to study the effects of different powder types (sizes and distributions) on the green and sintered densities achieved in titanium BJAM parts. Density is a critical feature of BJAM parts and understanding how different powders affect it (and subsequent part properties) is crucial to be able to tailor parts to specific applications. Density measurements through computed tomography (CT) are used to evaluate the effects of the different powder types on both bulk and localized density. The other main objective of this work is on the development of a tool to be able to predict part density, and subsequently part properties. The tool is based on the master sinter curve (MSC), an adopted powder metallurgy technique.

Chapter 2 of this thesis covers the background information regarding BJAM, titanium, sintering as well as methods and models to predict part density. Chapter 3 of the thesis covers the experiential methods used to evaluate the effects of different powders in both the CT and dilatometry analysis as well as preliminary results that guided subsequent work. Chapter 4 of the thesis presents the results of the analyses as well as discussion of the results. Chapter 5 presents conclusions on the results as well as suggested future work.

Chapter 2

Background Information

Though the concept of BJAM is relatively simple, in practical terms, the technology requires a thorough understanding of materials, powder metallurgy (PM) and sinter theory to be used productively. This is especially true if the entire BJAM process is to be mapped and optimized. This chapter includes the background information required for fully understanding the entire BJAM process, from the stock materials to the finished part with a direct application in fabricating titanium constructs for biomedical applications.

2.1 Binder Jetting Additive Manufacturing

BJAM is one of the seven categories of AM processes [12]. BJAM (also know as powder-bed binder-jetting and three-dimensional printing) was initially developed at the Massachusetts Institute of Technology and patented in 1993 [3]. Though there has been some improvement in the process, the technology has remained very much the same since its inception. The basic BJAM process begins with a three-dimensional CAD file that is sliced into layers.

These layers are printed out as images using an ink-jet print head onto a powder bed. The material that is jetted from the print head acts as a binding agent, joining the loose powder together. It is typical for systems to have a single print head, though some may have multiple heads to impart colour to the powder [5]. After a layer has been printed, more powder is spread over the bed and the process repeats. This general process is very similar to all other AM processes where the part being produced is built up layer by layer. However, BJAM does provide a few distinct benefits over other processes.

One major advantage that BJAM has is that it requires no support structures for any part geometry. While other AM processes can produce parts without the need for supports, in such cases the designs are limited to parts with no or severely limited overhanging features [13, 14]. BJAM does not require support structures for two reasons. The first is that any part is inherently supported by the surrounding powder in the bed. This in and of itself is not enough to preclude supports, since some powder bed fusion (PBF) processes are also supported by a powder bed. The second reason, which works in conjunction with the first, is that BJAM is a non-thermal process. The powder is consolidated using a binding agent, rather than through a directed energy source, such as a laser or electron beam. With no thermal input, there is no thermal stresses induced in the part. In addition, with a lack of melting and solidification or curing, there is a negligible dimensional change in the powder where binder is deposited. These two aspects of BJAM negate the need for support structures during the manufacturing process, unless parts are particularly large and supports are needed simply to support the weight of the part.

While there are benefits to BJAM being a non-thermal process, there is also a fairly significant drawback. The part removed from the BJAM system after printing, referred to as a green part, is not a usable, finished part. The term green part comes from PM and refers to a part that is held together using a temporary binder, compaction force or both. To be fully finished, the part must be cleaned and then either cured, infiltrated or sintered. Curing is the most basic process, simply setting the printed binding agent to make the part more robust. Infiltration with a polymer is typically used when producing parts for aesthetics and geometric representations [15]. This could either be for artistic pieces or non-functional prototypes. The infiltrated polymer is stronger and more robust than the binding agent, though it tends not to be strong enough for functional components in industrial or commercial applications. Infiltration with a low melting point metal or sintering is done for functional components that require significantly higher strength and performance capabilities [16, 17]. Sintering is done when a functional part is required, but a multi-material composite cannot be used or is prohibitive in some way.

Another major benefit that BJAM has is its wide material selection. This too is possible since BJAM is a non-thermal process. Issues surrounding cracking, over heating, segregation, etc., such as those seen in PBF, are not present. With the BJAM process being non-thermal, it also means that BJAM systems can use polymers, metals and ceramics. As long as the materials can spread across the powder beds, there is no fundamental change in the process or the equipment used. Though polymers are typically used in the binding agents, they can also constitute the material that makes up the bulk of the part.

A commonly used polymer for functional BJAM parts is Poly(methyl methacrylate) (PMMA) [18, 5]. This material, also commonly referred to as acrylic, is typically used in the investment casting industry for making masters. Though the BJAM process allows for the use of other powdered polymeric materials, use of them is not particularly prevalent. This is likely due to other AM process, notably PBF, fused deposition modeling (FDM), vat polymerization (SLA) and material jetting, being specifically tailored and more suitable for the processing of polymers. Polymers have also been used in BJAM as additives, most notably for changing the powder bed density either globally [19, 20] or locally [21].

The use of ceramic materials is significantly more prevalent in BJAM compared to polymers. Ceramic materials are particularly suited to BJAM due to their high melting temperatures, which prevent them from being used in most laser or electron beam based systems. The materials are also comparatively inert and inexpensive when compared with metallic particles. Ceramic materials are also the earliest materials used in BJAM, with ceramics used during the development of the process itself at MIT [22, 23, 24]. One of the more common materials currently used is plaster, which is mainly composed of gypsum. The material is typically mixed with large amounts of powder binder to be used for making color parts and/or aesthetically and geometrically representative parts. Another commonly used ceramic material is sand, which includes silica sands as well as more specialty types [25, 26]. This category of materials, being comprised of silica, zircon, chromite, and various synthetic sands [26, 25] is used almost exclusively for the production of sand molds for casting. Materials used for directly making components includes alumina [27, 28], zirconia [29], hydroxyapatite [29, 5], silicon nitride [30] and barium titanate [31] amongst others.

Though not as prevalent in its use, many different metallic or metallic-based materials are used in BJAM to directly make parts. One of the more prevalent materials is stainless steels, mainly 316L [16, 20, 32, 33] and 420 [34]). There has also been work on producing parts with materials as diverse as tungsten carbides [35] to magnetic materials [36, 37, 38]. There have also been works on the printing of titanium [19, 39], copper [40], Inconel 625 [41, 42, 43], and cobalt-chrome [44]. When metal powders are used in BJAM, they are nearly exclusively used for directly making parts, whereas with polymers and ceramics, they are typically used for indirectly making parts.

Though the medical and dental fields could take advantage of BJAM, currently the technology is not in wide use, if at all. This is unfortunate since the inherent porosity seen in BJAM parts can be greatly beneficial for medical applications. Porous parts have been found, in implants especially, to improve implant outcomes since the porosity leads to better bone ingrowth and reduced stress shielding [7, 6]. Porosity has also been seen to give better results for dental restorations as well [9, 11]. As mentioned in Chapter 1, this lack of adoption is likely due to a poor understanding of the process and no simple way to predict part properties. To help facilitate further adoption by the medical and dental fields, a predictive tool is developed for titanium components to determine density after sintering of the printed parts. The density can then be linked to additional part properties. The medical and dental field was chosen as the focus of this work since those industries can most effectively take advantage of both the porosity, design freedom and customization that is inherent to the BJAM process. Titanium was chosen as the material of interest for a few reasons. First, the material is bio-compatible and certified for both orthopaedic and dental parts. Second, titanium is currently used in both orthopaedic implants and dental restorations, giving any tool developed a wider applicability. Lastly, significant work has already been done on printing parameters for titanium, and this work can build on and add to that existing knowledge.

2.1.1 Binder Jetting Process Description

Though there are many ways to produce the final BJAM parts, the focus of this thesis work is on producing titanium parts that are sintered after the printing process. Since there is no infiltration being done on these parts, the final part properties are dependent predominantly on the structure obtained after sintering.

Materials

The materials used in BJAM fall into three main categories for the purposes of this thesis. The first is the material powder. This is the powder that makes up the bulk of the green part and is what remains after the sintering process. The material powder ideally consists of spherical particles with a low surface roughness [24, 43]. The powder size range can vary significantly from around 20μm [40, 20, 34], to around 75μm [40, 37, 19] and even as large as 150μm [21, 19]. Very fine powder (less than 20μm) tends to not be used due to poor spreadabilty [40, 24, 17]

The second category of materials is the binder powder. This is a solid-state binding agent that is mixed with the material powder. The powder binder used in this thesis work is polyvinyl-alcohol (PVA) and is discussed in more detail in Chapter 3.1. The binder powder composes a small portion of the green part, in the range of the 1-4wt% [19, 39], and is burned off during the sintering process. The binder powder tends to be smaller than the material powder to fit into the interstitial spaces between the material powder particles [34]. Generally, with a larger amount of solid binder, green part strength is increased but green density decreases [32, 19, 18]. Though it makes it easier to handle green parts, it increases the amount of shrinkage necessary to achieve the same final density.

Before printing begins, both the material and binder powders must be fully mixed to make a homogeneous mixture. The binder powder typically has a much lower density than the material powder which creates a mixture where segregation can easily occur and mixing is difficult. With materials of a similar size and density, it is difficult to achieve segregation of the two materials during mixing [45, 46, 47]. With significant difference in density, it is fairly easy to over-mix the powders, causing them to separate [47]. Specific mixing procedures are highly dependent on the materials being mixed, and the specific process used for this thesis work is explained in more detail in Chapter 3.1.

The final category of material is the liquid binder. This is the liquid-state binding agent that is deposited by the print head. This material works in conjunction with the solid-state powder binder to strongly adhere the material powder together and form the green part. The liquid binder is composed of a liquid that can dissolve the binder powder during printing. Both aqueous and solvent-based liquid binders can be used. Typically an aqueous binder is used for thermal ink jet print heads, as seen with systems produced by Z-Corporation and subsequently 3D Systems (www.3dsystems.com) after acquiring the company. Solvent-based inks typically include furan and phenolic binders [25, 26]. In addition to the main solvent, other materials, typically surfactants, binding agents and anti-biological agents, are added to create a more optimal liquid binder [17, 48]. The liquid binder can be formulated to improve quality and consistency of the jetting process and/or to have some effect on the printed part. The exact composition of the liquid binder used as part of this thesis is discussed in Chapter 3.1.

Printing

Once the stock materials are prepared, they are added into the system for printing. Since parts in BJAM do not need to adhere to the build plate, they can be printed an arbitrary height above the build plate. However, at the onset of printing, the build bed requires a relatively thick layer of powder to preventing shifting of the layers during the process. The feed bed requires an additional amount of powder to be added to compensate for powder used for compaction or surface filling as well as to facilitate adequate spreading. Depending on the system used, it is generally good practice to have between 20-50% more powder dispensed per layer from the feed bed compared to the specified layer volume.

There should also be powder completely covering the powder spreading surface to ensure there is consistent spreading during the printing process.

Once the beds have been filled, the printing process begins. A schematic of the process is shown in Figure 2.1. First, the roller pushes powder from the feed bed to the build bed. The roller also compacts the powder in the build bed, increasing the powder bed density [17, 49]. Typical commercially available systems utilize a counter-rotating roller to spread the powder. The spinning motion from the roller assists in pushing the excess powder forward during spreading and gives a more equal distribution of powder over the bed.

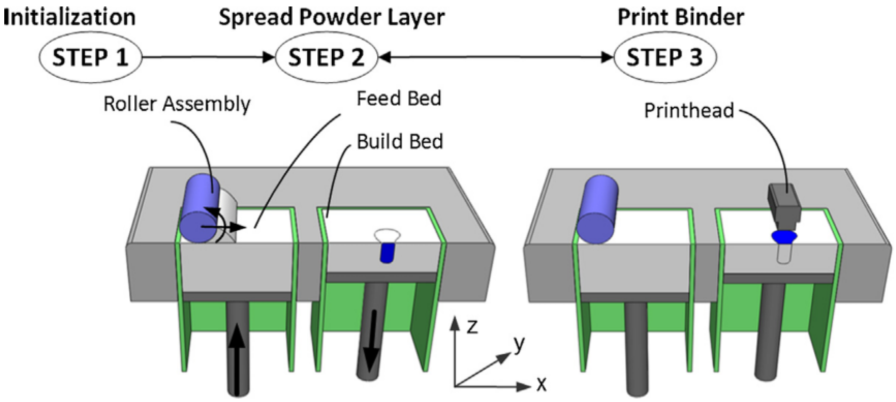

Figure 2.1: Schematic of the BJAM printing process showing powder spreading and binder deposition [50]

After the powder layer is spread, the print head deposits the liquid binder on the powder layer. A general schematic of the interaction is shown in Figure 2.2, where the liquid binder penetrates through the powder layer and is absorbed by the binder powder, adhering the material particles together. The penetration depth of the liquid binder is limited by the amount of solid binder present in the powder [51, 21]. With too much solid binder, the liquid binder cannot penetrate deep enough to adhere layers together. Without good layer adhesion, the green part will be too weak too handle [48, 21]. If too much liquid binder is present (or too little binder powder), the layer can become over saturated, causing bleeding into adjacent areas [18]. In addition, over saturation can cause layer shifting during printing, or the disturbance of particles in the bed [21, 17]. The printing process will cycle through powder spreading and binder deposition for each layer until all layers have been printed.

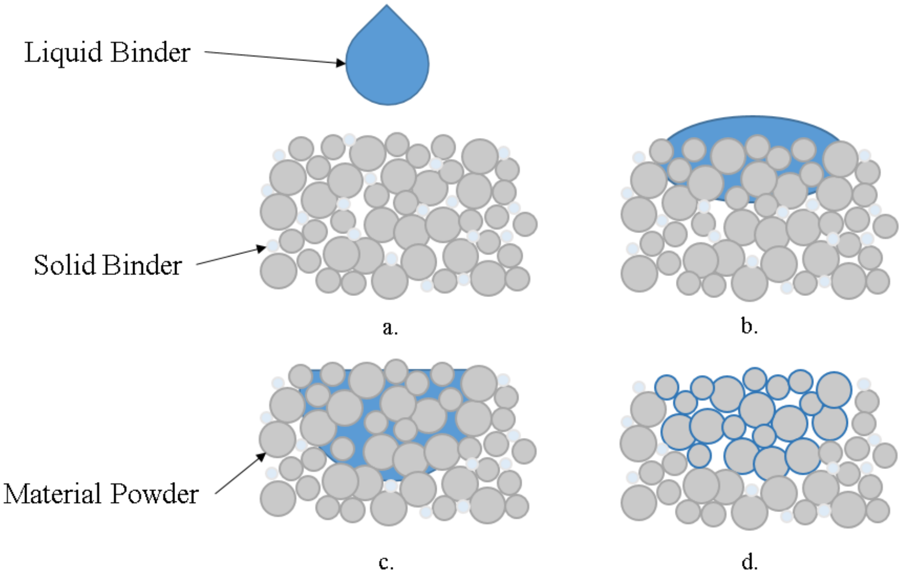

Figure 2.2: Schematic showing the deposition of liquid binder (a.), the initial absorption (b.), spread of the liquid binder in the powder bed (c.) and final adhesion of particles after evaporation (d.)

Part Cleaning and Drying

Once printing has finished, the produced green part must dry before it can be handled. This is especially true if there are small features on the part that can easily be damaged. Parts can either be left in the system or removed to allow the liquid binder to evaporate more quickly. Placing parts in a dry location at an elevated temperature accelerates the process. Once parts have been dried, they must be cleaned to remove any excess powder. The cleaning process for BJAM parts is somewhat simpler compared to other metal AM processes as only the remaining loose powder needs to be removed. However, it can be difficult to ensure that only loose powder is removed, and material making up the part itself is not also inadvertently removed.

Sintering

Once parts have been dried they must be sintered to make a usable part. There are two major steps in the sintering process. The first is the binder burnout step. Binder burnout is, as the name implies, the step in which both the solid binder and remnants of the evaporated liquid binder are removed from the printed part. This temperature is substantially lower than the typical sintering temperatures used for titanium. Binder burnout must be done in a controlled way to ensure that the part is not damaged. The porous nature of the printed part ensures that it is possible for the PVA to be completely removed. However, if the part is heated too quickly, the volatile binder will expand faster than it can exit the part causing the part to swell and crack [52]. To prevent this, the part is heated slowly to the burnout temperature. For parts made with titanium and PVA, the heating rate is typically around 5℃/min, with the binder burnout done at 300℃ [19, 39]. That temperature is then held for a number of hours depending on the size of the part to ensure the burn off is complete. The second step in the sintering process is the sintering itself. Sintering is done to fuse the titanium particles together, ensuring the part is held together through metallic bonds rather than an adhesive. Sintering is typically done between 1000℃ to 1500℃, with the time dependent on the level of density desired. More specific information on sintering is discussed later in Chapter 2.3.

2.1.2 Binder Jetting Process Variables

Ignoring the complexities of sintering, the BJAM process is relatively simple compared to laser or electron beam processes. However, there are still a number of key parameters that must be properly selected to achieve optimal results. One parameter that is common between all AM technologies is part orientation. In general, parts are weaker in the direction perpendicular to the layers. This is because intra-layer strength is typically greater than inter-layer strength [5]. While it is easy to optimize part orientation for simple geometries, an optimal orientation is more difficult to discern with a more complex part.

The parameter with the largest impact on the printed parts is the material powder used, with powder size and morphology being the most critical. Both particle size and morphology have a direct impact on the green part quality and density. Generally, the larger the particle size the poorer the feature resolution. However, larger particles tend to have better spreadability and are easier to print with. Reducing particle size can improve green density, up to a certain point, after which reducing particle size can have a detrimental effect on green density [40, 34, 53]. Smaller particles tend to have more contact points in a powder system with the same volume, increasing friction in the powder system [54, 55, 40]. Smaller particles are also more easily affected by electrostatic forces, causing particles to agglomerate together and stick to system components [5, 56]. The increased frictional and electrostatic forces can cause a decrease in green part density. Rough and irregular particles suffer similar issues as the smaller particles during spreading, typically due to protruding surface features that interlock and prevent good spreading, decreasing green density [49, 57]. Non-spherical particles, especially with high aspect ratios, will also align with the spreading direction, giving parts anisotropic properties [50].

Particle size also dictates the minimum layer thickness that can be used, which is another important process parameter. The minimum layer thickness must be at least as larger as the largest particle [17]. If the layer thickness is smaller, larger particles will be pushed through, and subsequently out of, the powder bed. Layer thickness can also be varied, though only within a relatively narrow band. The maximum layer thickness possible in most powder systems is around 200μm [21], since larger layer thicknesses give poor interlayer adhesion.

Another critical parameter is the binder powder used in the process. Similar to the material powder, the binder powder has a direct effect on green part quality, powder floawability and green part density. From previous works, it has been found that powder binder amounts within the range of 1wt% to 10wt% are feasible to use for the production of parts [19]. While parts can still be cohesive with lower amounts of powder binder, they tend to be weaker. In addition, parts with lower amounts of binder tend to have poorer feature definition. The higher binder levels do give better strength and features, but it comes at a cost of reducing green part density. The final influence that the binder powder has on the process is its ability to improve flowability. As discussed earlier, very small, rough or non-spherical particles tend to have poor flowability. The addition of more binder powder can improve the flowability of the powder system. With smaller particles, the binder powder can act as a carrier, allowing the particles to flow. With rough or non-spherical particles, the binder acts as spacer, preventing the material powder particles from locking together.

In addition to the powder binder, the liquid binder has a significant effect on the produced parts. The liquid binder-to-powder volume ratio can be controlled by increasing or decreasing either the liquid binder amount or the layer thickness. There tends to be an optimal level for liquid binder amounts based on the powder bed density, the surface area of the particles, as well as the amount of solid binder added [51, 34, 40]. Lower ratios of liquid binder tend to decrease green part strength and density [32, 51]. With lower ratios of liquid binder, the liquid binder can be fully absorbed within a layer, giving low inter-layer cohesion. In addition, with low ratios of liquid binder, there is a lower amount of wetting, giving poor intra-layer strength [51]. Generally, an increase in liquid binder, up to the optimal saturation level, increases the green part density [32, 51]. With suitable amounts of binder, good inter-layer cohesion and wetting can be achieved. However, if the liquid binder ratio is too high it is possible to over saturate the powder system, which can cause bleeding or layer shifting [21, 20, 18]. Though it is more common to have a homogeneous liquid binder distribution both within and between layers, the liquid binder content can be altered locally. Other works have discussed the effects of locally varying the binder amount and were able to see significant benefits [21]. Unfortunately, the localized variation of binder amount is not possible on most commercially available BJAM systems. While other parameters also have an impact on the process such as roller speed (both translational and rotational), atmospheric temperature, delay time between layers, etc. [32, 17]) they too are not controllable on most commercially available BJAM systems, such as on the system used to make samples as part of this work (see Chapter 3.2).

2.2 Binder Jetting Material of Focus

Titanium is a light metal with a very good strength-to-weight ratio. Titanium also has a number of other beneficial properties such as the ability to work at both elevated [58] as well as cryogenic temperatures [59]. Titanium also tends to have a substantially better fatigue life compared to other light metals [59]. Titanium is a highly reactive metal and readily forms a stable oxide layer on its surface when exposed to air (oxygen) or water. This highly stable oxide layer gives titanium a good level of corrosion resistance [60, 59].

This oxide layer also provides the material with exceptionally good biological properties, allowing for its use in implants [61, 62].

While titanium has a number of excellent properties, the material also has a two major drawbacks. First, the material is significantly more expensive than other, more common, engineering alloys. The high cost of titanium is predominantly due to the high cost of producing the stock material [60]. Its high reactivity with oxygen, which ensures titanium has a stable oxide layer, also means that when the material is at elevated or molten temperatures it must be processed in a vacuum or inert atmosphere. The other is that titanium is somewhat difficult to process using other conventional means such as forging and machining.

The properties of titanium, as outlined above, make the material an excellent candidate for AM and BJAM in particular. AM in general lends itself well to the production of low volume but high quality parts. With its high cost, titanium tends to be used for those types of applications, predominantly in aviation, defense, and the medical industries, where functional properties tend to be more important than the part cost. The poor formability and machinability of titanium makes producing parts conventionally more difficult and expensive compared to other materials. In addition, due to the fact that BJAM is a non-thermal process, the printed parts can be made at room temperature, negating the need for a controlled atmosphere during printing. While parts must be sintered afterwards, it is significantly easier to control the atmospheric conditions in a furnace compared to forming or casting dies (for conventional manufacturing) or a PBF or DED AM system.

2.2.1 Titanium Alloys

Titanium alloys are broken up into defined categories based on the two phases, or the combination of them, that are present in the material. The two phases that can occur in titanium materials are alpha (α), which has a hexagonal close-packed (HCP) structure and beta (β), which has a body centered cubic (BCC) structure. In elementally pure titanium the alpha and beta phases are stable below and above the alpha-beta transition temperature respectively. Below the alpha-beta transition temperature the alpha phase is stable, but the beta phase can be made meta-stable with the addition of certain alloying elements [59]. The main categories of titanium alloys are divided based on the quantity of alpha and beta contents and are: commercially pure alloys (CP), α alloys (made up of α and near-α alloys) , α+β alloys and β alloys (made up of metastable and stable β alloys) (see Figure 2.3). CP titanium is composed almost entirely of alpha at room temperature, with the alloy having a small amount of alloying elements that cause some beta to be present [59]. With each subsequent category, more alloying elements are added and more beta phase is present (or at least able to be present) in the material at room temperature. Since CP titanium is the material of focus in the present thesis, only it will be covered in more detail.

Alpha and Beta Phase

Below the alpha-beta transition temperature, CP titanium is composed almost entirely of the alpha phase. It is the hcp structure of the alpha phase that causes many of the difficulties in the mechanical forming and machining of titanium [64]. When alpha phase grains grow larger, the material is more easily deformable due to twinning mechanisms [65, 59]. The twinning mechanism and anisotropic effects of the hcp alpha phase are of

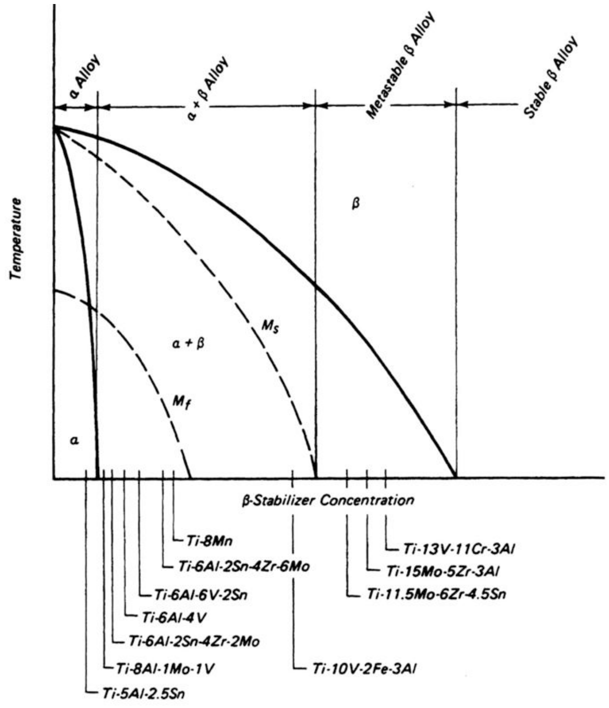

Figure 2.3: Titanium alloy classification based on alpha and beta phase content [63]

more significant interest in forming operations due to the alignment of grains and the anisotropic properties is causes. Since BJAM parts are not produced using any forming there is no preferential alignment of the grains, though there can be alignment of particles. The titanium powder, discussed in more detail in Chapter 2.2.2 has no grain alignment, giving the parts less anisotropic properties.

The thermal properties of the alpha phase are also important to the processing of BJAM parts. The alpha phase has an unusually high diffusivity rate for interstitial elements, with hydrogen, oxygen and nitrogen all easily soluble and diffusible in the alpha phase [59, 65, 66]. This is of particular importance for the processing of titanium since any elevated contents of hydrogen, oxygen or nitrogen will cause excessive embrittlement of the material [5, 58].

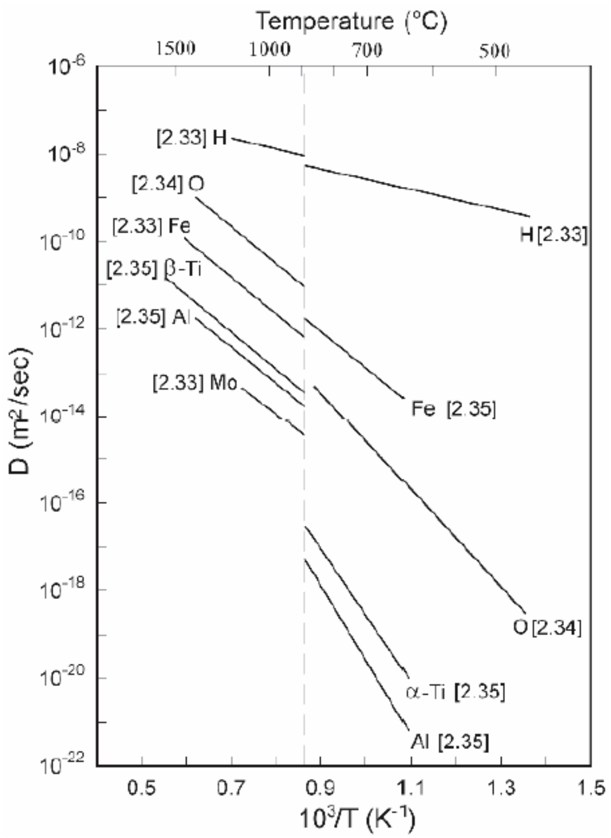

Figure 2.4: Arrhenius plot of volumetric diffusion of elements (H, O, Fe, Al and Mo) and self diffusion (α and β) in pure titanium [59]

The alpha-beta transition temperature of pure Ti is 882℃, and is approximately the same for CP titanium due to the minor amounts of alloying elements. The phase transformation of alpha to beta is similar to other allotropic phase transformations [66, 59]. The bcc beta phase has substantially higher substitutional diffusion rates, being approximately two to three times higher than the alpha phase [67, 66]. This is of particular importance for sintering, since self-diffusion is the major rate controlling factor for sintering of commercially pure titanium [55, 68]. Sintering of titanium must therefore take place above the transition temperature for sintering to occur in any reasonable time. The beta phase shows similarly high interstitial diffusivity of hydrogen, oxygen and nitrogen. The beta phase has significantly higher solubility of hydrogen compared to the alpha phase. This difference in solubility levels leaves CP titanium susceptible to hydrogen embrittlement and cracking [65]. Cracking is at a higher risk of occurring if the titanium material is quenched from high temperatures. When cooling titanium from the beta phase, a martensitic phase can form during very fast cooling rates. This martensitic phase is more susceptible to cracking due to significantly higher stiffness. However, the low cooling rates seen during furnace cooling after sintering prevent the martensitic transformation from occurring [59].

Commercially Pure Titanium

As mentioned previously, the composition of commercially pure titanium, has a very low amount of alloying elemental content. There are ten grades of CP alloys, with three distinct subgroups within the category itself. The first category is composed of grades 1, 2, 3 and 4 (see Table 2.1), the second being composed of CP titanium grades 7, 11, 16 and 17 and the third group composed of grades 26 and 27 (see Appendix A).

Table 2.1: Chemical composition of commercially pure titanium grades 1-4 [69]

	Content (weight %)			
Element	grade 1	grade 2/2H	grade 3	grade 4
Carbon (max)	0.08	0.08	0.08	0.08
Oxygen (max)	0.18	0.25	0.35	0.40
Nitrogen (max)	0.03	0.03	0.05	0.05
Hydrogen (max)	0.015	0.015	0.015	0.015
Iron (max)	0.20	0.30	0.30	0.50
Other (individual - max)	0.1	0.1	0.1	0.1
Other (total - max)	0.4	0.4	0.4	0.4

In the first category, the only alloying elements present in the alloy are oxygen and iron, with increasing quantities of each element as the grades move from 1 to 4. In the second group, oxygen and iron are still present, but very small amounts of palladium are added. In the third group oxygen and iron are still present, but ruthenium is added as opposed to palladium. The specific titanium alloy used as part of this thesis work is CP titanium grade 1, so that group of CP titanium materials is the focus of this background work.

The quantities of oxygen and iron in the grade 1 CP titanium are in very low quantities. Oxygen is an alpha stabilizing element and highly soluble in titanium. Oxygen is present in the alpha phase of titanium and provides solid solution strengthening [65, 64]. Iron is a beta eutectioid stabilizer and has very low solubility in the alpha phase [65, 64]. During cooling from initial processing, the iron will be rejected into diminishing amounts of beta phase. The very low amount of iron causes a similarly small amount of the beta phase to be present at room temperature [64]. This small amount of beta remains around the alpha grain boundaries, pinning them [65, 64]. This pinning mechanism helps to prevent excessive grain growth during recrystallization treatments [65, 64]. This also has the benefit of maintaining smaller grain sizes during the sintering of the titanium particles, contributing to part strength. There are numerous sets of material properties that can be explored, but this background work has been limited to those properties that have a direct impact on the printing and sintering of titanium BJAM parts.

2.2.2 Titanium Powder

The powder properties of titanium have a major influence on the printed BJAM parts in addition to the printing parameters themselves. Titanium powder has two major fields of use which are PM and AM. The material requirements for laser or electron beam AM processes are significantly different compared to those for BJAM. The material requirements for BJAM, and even the process itself, is much more similar to traditional PM processes, which is why information from BJAM specific and PM specific sources are investigated.

Powder Manufacture

Due to the high reactivity of titanium, there is a limited number of methods that can be used to produce titanium powder of a suitable quality. The most prevalent method to produce titanium powder is through reduction methods, with reduction being carried out either chemically or electrochemically [70, 60]. Chemical reduction involves reducing titanium tetrachloride to titanium while electrolytic reduction involves the reduction of titanium oxide. Both chemical and electrolytic reductions produce a titanium sponge that requires further processing to become powder [70, 60]. Powder can be made by either mechanically crushing the titanium sponge, or processing the sponge through a hydride/dehydride process. The hydride/dehydride process involves expanding the titanium sponge by converting it to titanium hydride, causing it to shatter. The material is then de-hydrogenated, using a variety of means, resulting in titanium powder.

The other class of powder production is atomization. During atomization the feedstock titanium is melted and requires an inert atmosphere. Due to the reactive nature of titanium, powder can only be made by gas, plasma and rotating electrode atomization [70, 60]. The electrode rotating process involves rotating a round bar stock of titanium while applying either a standard electrode or plasma torch to generate molten material at the end of the bar [70]. The molten material is then flung off by rotational forces, creating the powder. During gas and plasma atomization process, a high velocity flow (either gas or plasma) impinges of a stream of molten metal, disrupting it and creating powder [71]. For both processes, either argon or helium gas is used [70].

Powder Characteristics

Though there are a number of different methods for producing titanium powder, only two make powder suitable for the BJAM process. The powder produced through reduction methods, using either mechanical crushing or hydride/dehydride are far too small to be used for BJAM [60]. As discussed earlier, the very fine particles have very poor flowability, resulting in unsatisfactory print quality. In addition, the fine powders produced through the methods have a very rough, irregular surface which makes flowability even worse. The other unsuitable method is the rotating electrode process, with either a standard electrode or plasma torch. While the process does make smooth, spherical powder, the particle size range achievable is too large, being in the range of 100μm to 300μm [72, 71].

Therefore, the only two production methods suitable for BJAM titanium powder are gas and plasma atomization. Though both are suitable, plasma atomized powder has a number of benefits over the other possible methods. The first is that the plasma atomized powder tends to be more spherical than gas atomized powder. The improvement in sphericity allows for better flowability and print quality. The sphericity also ensures that there is no preferential alignment of the powder during spreading that could impart anisotropic properties to the final part. The plasma atomized powder also tends to have substantially less satellite particles than gas atomized powder [71]. These satellites (small particles attached to larger particles) can reduce flowability and can cause some form of preferential alignment during spreading. Plasma atomized powder can also be made smaller than gas atomized powder [72, 71]. This is beneficial if the material is still large enough to be printed with as it can increase green part density. Finally, the other benefit that plasma atomization has is the chemical purity of the powder. For the CP grades especially, the control of very small quantities of oxygen, nitrogen and hydrogen is critical to ensure a material is within specifications. Plasma atomized powder has shown to have smaller quantities of dissolved and adsorbed gases, allowing for a higher quality powder [72].

2.3 Sinter Theory

The sintering process is crucial since it connects the titanium particles with metallic bonds through a diffusion process, as opposed to the adhesive used in the printing process. This gives the parts strength, allowing them to be mechanically loaded. In addition to making the part stronger, the sintering process can also be used to control the density of the final part. Density is closely linked to static and dynamic mechanical properties as well as many other part properties. Sintering is fundamentally based on the reduction of surface energy of the system (i.e. the surface energy of the part). There are three stages of sintering, shown in Figure 2.5 that can occur during the sintering process, with each one producing parts with distinct morphologies.

2.3.1 Stages of Sintering

The first, or initial stage of sintering occurs at lower temperatures and is dominated by surface diffusion [54], explained in detail in Section 2.3.3. At the start of the initial stage, there are no sinter necks present and the part will be at its green density. For titanium parts made by BJAM, this is typically in the range of 50%-60% dense. During the initial stage, material shifts on the surface of the particles to contact points, creating sinter necks [54], as shown in Figure 2.5. There is little dimensional change in parts during the initial stage with linear shrinkage being around 3% [73]. The part moves past the initial sinter stage once the sinter necks are approximately 1/3 the diameter of the particles [73]. This usually occurs when the part is approximately 60% to 70% of its theoretical density [74, 75].

After the initial stage, the parts enter the intermediate sinter stage. The intermediate stage occurs at higher temperatures, with the specific temperature being determined by the particle size. The mechanisms present in this stage are dominated by volumetric diffusion, discussed in Section 2.3.3. During the intermediate stage a significant amount of densification occurs. The part will go from being 70% to approximately 92% of its theoretical density [74, 55]. During the intermediate stage the pores of the part are initially smoothened, becoming more tubular as opposed to spherical [74, 73]. Sinter necks grow from approximately 1/3 to 1/2 of the particle diameter and as densification progresses, the long, tubular pores become closed [54].

Once the pores are closed (1/2 particle diameter and 92% dense), the part has entered the final sinter stage. The final sinter stage takes place at approximately the same temperatures as the intermediate stage and similar sinter mechanisms are present. During this stage the enclosed pores are eliminated, if possible, and the part will achieve its maximum possible density. Since the titanium parts are being sintered in systems a little over atmospheric pressure, 100% density is not possible to achieve [58]. During this stage, the grain structure within the part coarsens significantly as well [54].

For each sinter stage, and throughout the entire process, there are two major aspects of the system, which are the thermodynamics (driving force) and kinematics (mechanisms) of sintering. Both aspects work in unison but are fundamentally different. Both aspects of the sintering process need to be considered, understood and controlled to properly manage the sintering process.

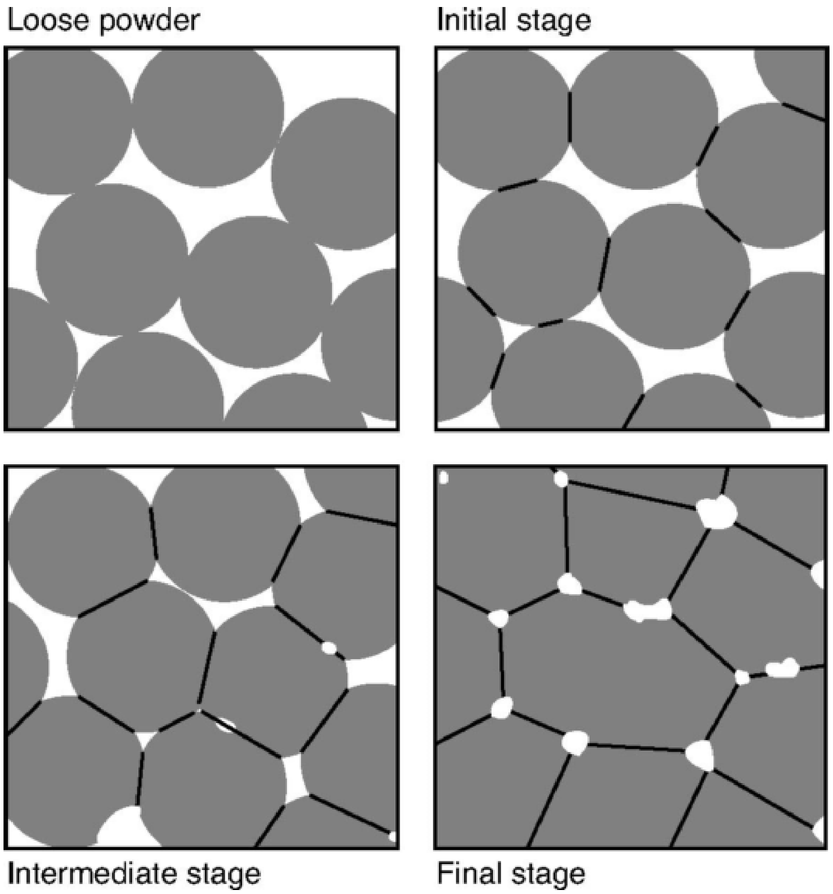

Figure 2.5: Schematic showing the general sintering process for a powder system: unsintered (loose powder), initial stage, intermediate stage and final stage [73]

2.3.2 Thermodynamics of Sintering

In general, the driving force for the sintering process is the reduction in energy of the system. This driving force is dependent exclusively on the powder material and unlike the sintering mechanisms, is not dependent on temperature. The energy of the system is, at a fundamental level, based on the broken or incomplete bonds of the titanium atoms [73]. At any interface, the atoms are not fully bonded, causing them to be in a higher energy state.

The reduction in energy of the system occurs by reducing the number of atoms in a higher energy state. Sintering continues as long as the total energy in the system is decreased and stops once that is no longer possible.

During the initial stage of sintering, necks form between adjacent particles. There is a large driving force to generate necks due to the effects of surface curvature, κ [74]. A curved surface has a higher energy compared to a flat surface. When a surface has curvature there is an uneven distribution of forces on the atoms causing the surface to be in tension if it is concave and compression if it is convex [73]. As the sinter necks form, the total curvature of the surface is reduced, reducing total system energy. This stress is also the reason why material moves from the convex surfaces (particles) to the concave surfaces (necks). When a surface is under tension or compression, the surface will respectively have a higher and lower vacancy concentration [73]. This difference in vacancy concentrations causes a source-sink relationship, where material from the particles preferentially moves to the necks [55]. The exact mechanisms by which this happens is discussed in Chapter 2.3.3. Equation 2.1 describes the relationship between capillary stress (σ) in a sinter neck as being proportional to the surface energy of the particles (γ) and the inverse of the particle radii (r_1, r_2 - for particles 1 and 2). With smaller radii, particles will have a higher curvature, and therefore a higher driving force for sintering. This in turn means that the powder system requires less energy for sintering to occur. As seen in Figure 2.6, smaller particles have a significantly higher stress, and therefore driving force for sintering. While equation 2.1 and Figure 2.6 are specific for sinter stress, many of the driving forces forces based on particle geometry are proportional to the inverse of the particle radii and show a similar trend [73].

$$\sigma = \gamma\kappa = \gamma\left(\frac{1}{r_1} + \frac{1}{r_2}\right) \tag{2.1}$$

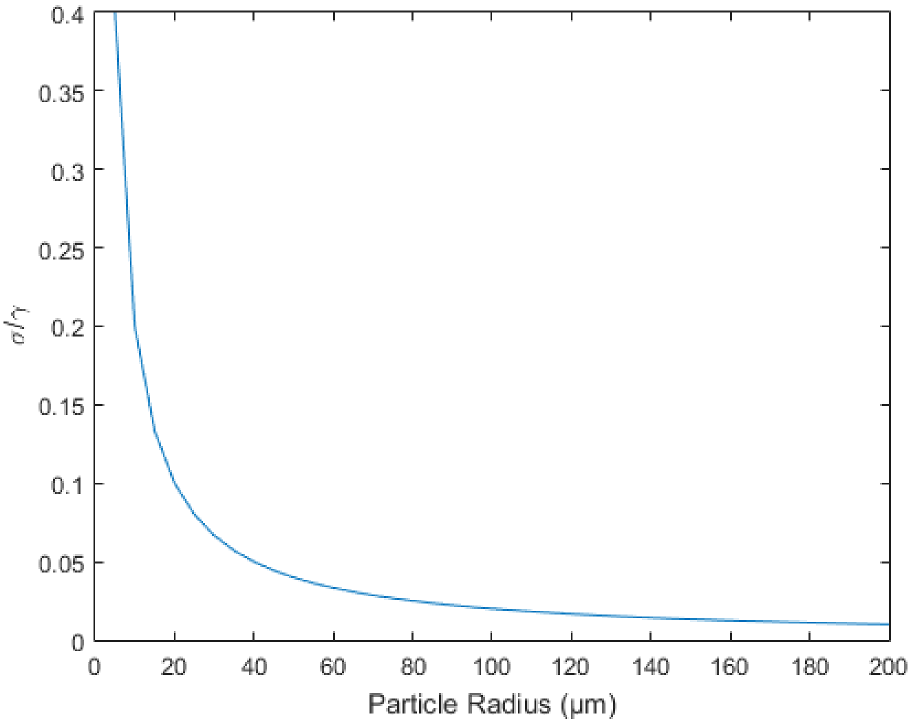

Figure 2.6: Relationship between particle radii and the capillary stress seen in a powder system based on Equation 2.1 and assuming particles of equal size

In addition to reducing surface curvature, the formation of necks also reduces the surface area to volume ratio of the powder system (SA:V), described by equation 2.2. Similar to capillary stress, the surface area to volume ratio is also directly proportional to the inverse of the particle radii (r), following the exact same profile as shown in 2.6. As the size of the particles increases, the total surface area of the powder system decreases, decreasing system energy. This also contributes to the lower energy required for sintering of smaller particles as the comparatively high surface area to volume ratio gives the system a higher driving force for sintering [76].

$$SA:V = \frac{4\pi r^2}{\frac{4}{3}\pi r^3} = \frac{3}{r} \tag{2.2}$$

The final major driving force in sintering for titanium is grain boundary interfaces [54]. During the sintering process, particles will undergo a stress relief (if the process is slow enough) and subsequently a recrystallization process. This recrystallization process generates new grains, which also generates new grain boundaries. These boundaries, though they have a lower energy than a surface-pore interface, increase the total energy of the system. As sintering progresses, the grains will coarsen, to reduce system energy [54].

2.3.3 Kinematics of Sintering

There are three major categories of sintering mechanisms, all of which can be active in some combination during the sintering process. The relative impact of each mechanism depends on the material and sintering conditions. The main categories are solid-state, liquid and viscous sintering. Solid-state sintering occurs with the material in its solid form, and diffusion controlled mechanisms dominate the process. In liquid sintering, some volume of liquid is present, typically in small amounts, which facilitates the sintering process [77]. Viscous sintering, somewhat similar in concept to liquid sintering, occurs in amorphous materials where the material can flow, but is not considered to be a fluid [78]. Liquid and viscous sintering mechanisms have a negligible, if any, effect on the sintering of CP titanium [68] and therefore solid-state sintering is the focus of the following sections.

2.3.4 Solid-state Sintering

As the name implies, solid-state sintering occurs when the material is in a solid state. Depending on temperature, the same part can undergo multiple types of sintering processes. However, as mentioned earlier, only solid-state sintering is applicable to CP titanium parts. The sintering mechanisms that occur with the solid-state method are predominantly based on atomic diffusion. Within the category of solid-state sintering, there are two distinct types of sintering mechanisms that contribute in different ways to the sintering process. The first type is coarsening or non-densifying sintering. These mechanisms typically occur at lower temperatures and are comprised of surface effects [79]. The other type is volumetric or densification sintering. These mechanisms occur at higher temperatures and cause the shrinkage seen in parts [79]. Both mechanisms can occur at the same time, and the prevalence of each one depends on the sintering temperature.

Densifying Sintering

Densifying mechanisms, as the name implies, are those that increase the density of the part. In densifying sintering, mass from the particles will move from the core of the particles to the necks [79]. This movement of mass causes the centers of the particles to move closer together, as shown in Figure 2.7. The particle centers moving closer together is what causes shrinkage during the sintering process. The first to cause this is the typical lattice or volumetric diffusion. This occurs in CP titanium as self diffusion, where the process is caused by vacancies in the lattice structure. The base number of vacancies in the lattice is directly proportional to temperature. The mechanism is only active at higher temperatures (typically above 1100℃) due to the requirement of a large number of vacancies to provide any meaningful mass flow [79]. The other prominent densifying mechanism is grain boundary diffusion. Grain boundary diffusion occurs at lower temperatures compared to volumetric diffusion since it does not rely on the creation of vacancies, with atoms being able to take advantage of the space provided by grain boundary interfaces. Atoms will diffuse from grain boundaries inside the particle to the surface of the particle. The effect is the same as volumetric diffusion though the mechanism is dependent on the quantity of grain boundaries as well as temperature [74]. The final mechanism that causes densifying sintering is plastic flow. Plastic flow occurs from the movement of dislocations in the lattice structure. However, for the mechanism to cause densifying sintering, the dislocation must occur at the surface and move inwards to either a grain boundary or isolated pore [79]. There is some evidence that the surface stresses from surface curvature generate enough stress to form dislocations, however the total effect of the mechanism is questionable [79]. This mechanism can only occur at lower temperatures, since at elevated temperatures the part is weak enough such that dislocations will not form.

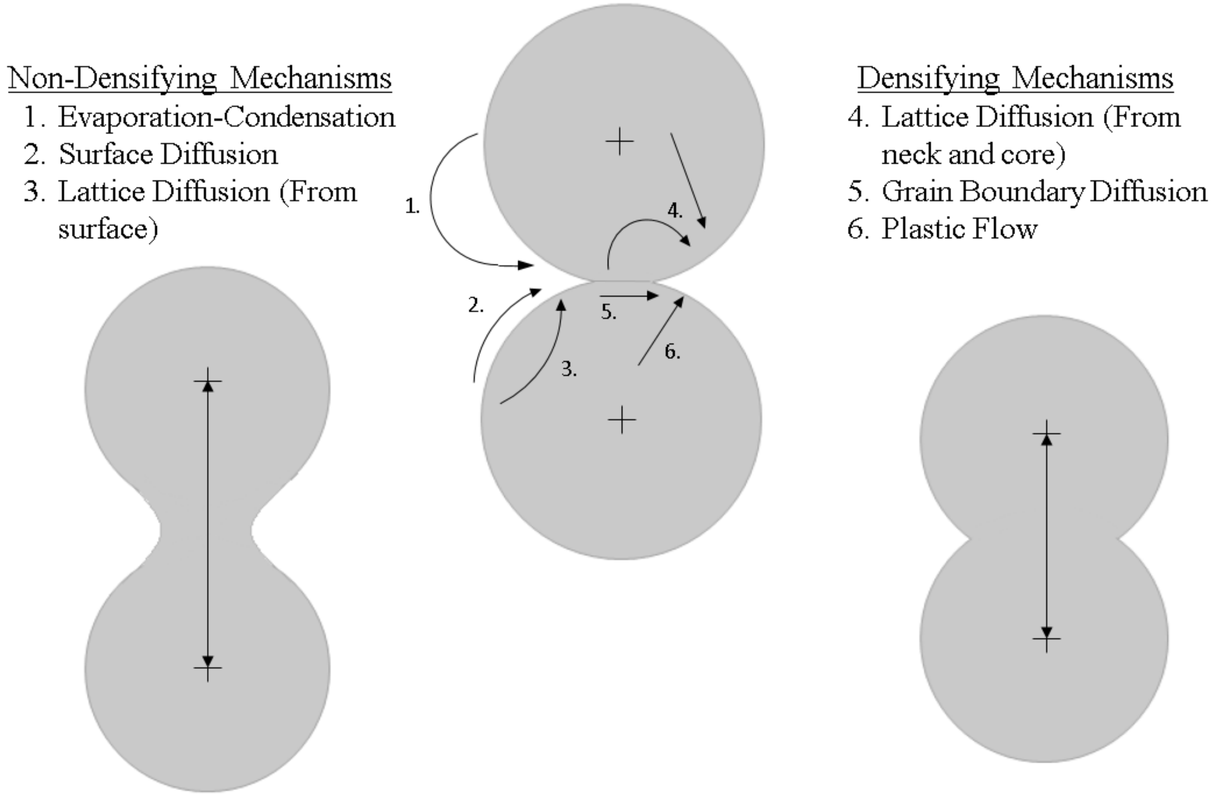

Figure 2.7: Possible transport mechanisms seen during solid-state sintering

For the application of CP titanium, and most metals in general, the only mechanisms that truly cause densifying shrinkage to any appreciable degree are volumetric and grain boundary diffusion [79]. It is important to note that it is the powder system and geometry that determines where material diffuses to. Material properties and temperature only determine how the material diffuses.

Non-densifying Sintering

Non-densifying or coarsening sintering are mechanisms that do not cause the centers of particles to move closer together. Instead, material is redistributed along the particle surface from convex to concave areas [79], as shown in Figure 2.7. Since material is not moved from the core of the particle, there is no appreciable shrinkage of the part. Rather the structure is smoothed (or coarsened) to reduce surface curvature and surface area. The main mechanism that causes this is surface diffusion. Surface diffusion is simply the movement of atoms along the surface of the particle. This mechanism occurs at the lowest temperatures of any of the mechanisms, due to the comparatively high energy of particles on the surface [54] and lower activation energy [66]. The other mechanism that causes coarsening is evaporation and condensation. Through this mechanism, material will evaporate at convex areas and condense at concave areas, allowing material to be transferred across pores rather than simply on or through the particles themselves. Material preferentially evaporates at convex and condenses at concave areas due to a slightly higher and lower vapor pressure at those areas respectively [80]. The effects of this mechanism are typically considered negligible for most materials since the vapor pressure is low at any realistic sintering temperature [79]. Though titanium has a relatively high vapor pressure compared to other metals, the effects of evaporation-condensation are likely minimal.

2.4 Master Sinter Curve

The master sinter curve (MSC) is a relatively new concept that was first proposed in 1996 [81]. The MSC is an empirical model derived from the combined stage sinter theory. The MSC is one of many models that have been used, predominantly in , to predict the results of sintering [55, 79]. The model has been used with good success for a number of metallic materials including 316L [82, 83], 17-4PH [84, 83], titanium [10, 85, 86] and molybdenum [87, 88]. It has also been used for a number of different ceramic materials such as Al_2O_3 [89, 90, 81], ZrO_2 [91, 89], TiO_2 [92, 93, 94] and others. Early sintering models were typically simplistic, representing the sintering process in a single stage with only one sinter mechanism driving the process [55]. Later models, the combined stage sinter theory included, represent the sinter process more closely, being applicable to multiple sinter stages and using multiple sinter mechanisms [95]. The MSC is an empirical model and does not require nearly as many material and powder parameters as compared to theoretical models [81]. While the sintering process is, in general, relatively well understood, the exact mechanisms that occur during sintering and when particular ones are active is not. This makes it difficult to use a theoretical model to accurately predict the sinter process outcome, even if it can represent multiple sinter stages and mechanisms [96]. In addition, to be able to use the theoretical models, a large amount of information regarding both the powder and material are required [95]. This information is typically not available in literature or reference material and is difficult to obtain. Since the MSC is empirically based, the complexities inherent to the process and powder do not need to be explicitly found [81].

2.4.1 Combined stage Sinter Theory

The MSC is based on the combined stage sinter theory. The combined stage sinter theory (equation 2.3), developed in 1992 [95], is a method of determining the instantaneous shrinkage of a powder system (shown by $-\frac{dL}{Ldt}$, with L being the initial length) during sintering, based on a set of material parameters (equations 2.4 and 2.5 and table 2.2), geometric factors (equations 2.6 and 2.7 and table 2.3) and temperature. The combined stage sinter theory is applicable to all sinter stages and determines the shrinkage based on volumetric and boundary diffusion mechanisms [95]. The model generated by the combined stage sinter theory, and its relevant parameters are described in Tables 2.3 and 2.2 respectively.

$$-\frac{dL}{L_0dt} = \frac{\gamma\Omega}{kT}\left(\frac{\delta D_b \mathit{\Gamma}_b}{G^4} + \frac{D_v \mathit{\Gamma}_v}{G^3}\right) \tag{2.3}$$

$$D_b = D_{b0} exp\left(\frac{-Q_b}{RT}\right) \tag{2.4}$$

$$D_v = D_{v0} exp\left(\frac{-Q_v}{RT}\right) \tag{2.5}$$

$$\Gamma_b = \frac{\alpha_p C_k C_b}{C_\lambda C_a C_h} \tag{2.6}$$

$$\Gamma_v = \frac{\alpha_p C_k C_v}{C_\lambda C_a C_h} \tag{2.7}$$

The geometric scaling factors (Γ_b, Γ_v) used in the combined stage sinter theory are derived from a geometric model proposed by DeHoff. The model represents the powder

Table 2.2: Combined stage sinter theory parameters and variables (Equations 2.3, 2.4 and 2.5)

Parameter	Description
L_0	initial length
γ	surface energy
Ω	atomic volume
k	Boltzmann constant
T	absolute temperature
δ	grain boundary thickness
G	mean grain (particle) diameter
D_b	coefficient of diffusion (grain boundary)
D_v	coefficient of diffusion (volumetric)
Γ_b	geometric scaling factor (grain boundary)
Γ_v	geometric scaling factor (volumetric)
D_{b0}	pre-exponential of diffusion coefficient (grain boundary)
Q_b	activation energy (grain boundary)
D_{v0}	pre-exponential of diffusion coefficient (volumetric)
Q_v	activation energy (volumetric)
R	universal gas constant

system using a number of simplified geometric and scaling parameters and is used to represent the sintering process [97, 98, 95]. The DeHoff model represents each powder particle (also referred to as a grain) as an irregular polyhedron, with each polyhedron made up of pyramids [97]. This then allows for the representation and calculation of the location of sinter necks and diffusion distances in a particle.

2.4.2 Master Sinter Curve Creation

As indicated by tables 2.2 and 2.3, the combined stage sinter theory requires a significant amount of information on both material and geometric parameters to properly model the process. The aim of the MSC is to simplify the use of the model. To do this, three

Table 2.3: Geometric factor variables derived from the DeHoff model [97]

Parameter	Equality	Description
$\bigtriangledown\mu$	$\alpha_p K/\lambda$	gradient in chemical potential (for diffusion)
λ	C_λG	maximum diffusion distance
K_h	$-C_k/G$	curvature at the neck
$\delta L_b/2$	$\delta G C_b$	area for diffusion (grain boundary)
A_v	$C_v G^2$	area for diffusion (volumetric)
S^b	$C_a G^2$	area at the base of the pyramid (grain boundary)
h	$C_h G$	height of the pyramid

assumptions are first made [81]. The first is that there is isotropic shrinkage, which allows the uniaxial shrinkage rate to be converted to the densification rate. The second assumption is that there is a single, dominant sinter mechanism during the process (i.e. volume or grain-boundary). The final assumption is that both G and Γ (i.e. material and powder properties) are only dependent on density. Using these assumptions, the combined stage sinter theory can be rearranged as shown in equation 2.8. With the rearrangement, the left-hand side and right-hand side are equal but independent.

$$\int_0^t \frac{1}{T} exp\left(-\frac{Q}{RT}\right) dt = \frac{k}{\gamma\Omega D_0}\int_{\rho_0}^{\rho} \frac{(G(\rho))^n}{3\rho\Gamma(\rho)} d\rho \tag{2.8}$$

Table 2.4: Additional parameters and variables for the combined stage sinter theory after assumptions and rearrangement to create the MSC (Equation 2.8)

Parameter	Description
ρ	density
Q	apparent activation energy of the system
D_0	diffusion coefficient (D_{b0} for grain boundary, D_{v0} for volumetric)
n	exponential diffusion constant (4 for grain boundary, 3 for volumetric)

There tends to be a consensus that the first assumption holds true for this model and most materials. There is some concern that the second assumption may not be true for all materials [84] and there have also been doubts whether the third assumption holds for all cases as well [88]. However, other studies [10, 86, 85] show no detrimental effects on the accuracy of the MSC results for titanium materials. One condition, that can also be considered an assumption, is that for the model to work, the material system is kept constant. The equality between Θ and Φ does not hold if the material parameters (material type, particle size, processing history, etc.) that make up Φ are altered. This means that MSCs made for a specific powder system are inapplicable to others.

The left-hand side of equation 2.8 is the master sinter parameter (MSP), represented by Θ (see equation 2.9), which includes the effects of sintering, with temperature being a function of time during processing. The right-hand side of equation 2.8 is a representative value of all of the material system parameters (shown as Φ) and how they change throughout the sintering process (see equation 2.10). The MSC is technically derived through the relationship between ρ and $\Phi(\rho)$, since it is Φ that is a function of density [81]. However, the equality from the assumption and rearrangement (equation 2.11) allows for the development of the MSC using Θ, removing the need to measure material parameters and simplifying the work tremendously.

$$\theta(t, T(t)) \equiv \int_0^t \frac{1}{T} exp\left(-\frac{Q}{RT}\right) dt \tag{2.9}$$

$$\Phi(\rho) \equiv \frac{k}{\gamma \Omega D_0} \int_{\rho_0}^{\rho} \frac{(G(\rho))^n}{3\rho\Gamma(\rho)} d\rho \tag{2.10}$$

$$\theta(t, T(t)) \equiv \Phi(\rho) \tag{2.11}$$

The MSC can be found using a few different methods, but the most prevalent and simplest method is using a dilatometer [81], though one group did validate the MSC based on material parameters [99]. By using a dilatometer, the shrinkage of the part during sintering is known and with other analysis methods, the final density of the part can be measured. With the final density and shrinkage known, the density of the part at all temperatures and times can be found. The only parameter not known is the apparent activation energy (Q) of the process. Since the material is kept constant, Q will be the same no matter the sintering procedure. Therefore, Q can be found by running multiple experiments, usually sintering parts with different constant heating rates [81]. Constant heating rate dilatometry experiments are typically done for the sake of convenience. The apparent activation energy (Q) of the process is typically found by generating a sigmoidal curve, with one example shown in equation 2.12, that is similar in shape to a general MSC. Other types of curves, such as a piecewise [100, 90] can be used, but generally a sigmoid function matches the shape of the MSC well [81]. This sigmoidal curve is then compared to the measured data to find a curve of best fit. The fitting curve used for this thesis is shown in equation 2.12 [88]. Other fitting curves have been used by other groups and are shown in Appendix A.

$$\rho_r = a + \frac{1-a}{1 + exp\left(-\frac{(ln\Theta - b)}{c}\right)} \tag{2.12}$$

Table 2.5: Sigmoidal constants and parameters for equation 2.12 [88]

Parameter	Description
ρ_r	relative density
a	initial relative density
b and c	constants determined using the Newton-Rhapson method

Regardless of the sigmoidal function used, the end purpose is the same, which is determining the Q. As stated earlier, multiple densification experiments are run on the same part types to get densification curves. Since the materials used for these parts are the same, there should be no difference between these parts if plotted as a function of ln(Θ) versus ρ [81]. Therefore, the sigmoidal curve, and its respective Q value, that best represents the MSC is one that minimizes the error between the multiple densification curves. The most common method for finding the sigmoidal curve is using a mean residual squares (see equation 2.13) method comparing the plotted densification curves and the sigmoidal curve. Both the dilatometry data and the sigmoidal curve are plotted for a specific Q value. The difference between the measured data points and calculated points (from the sigmoidal curve) are found. The comparison is completed for are a wide range of Q values that cover the expected range. The Q value with the lowest mean residual square value is the correct value for the powder system, as this is the value that generates the MSC with the smallest difference between the different heating rate experiments.

$$MeanSquareResidual = \sqrt{\frac{1}{\rho_f - \rho_0} \int_{\rho_0}^{\rho_f} \frac{\sum_{i=1}^{N} \left(\frac{\Theta_i}{\Theta_{iavg}} - 1 \right)^2}{N}} \tag{2.13}$$

Table 2.6: Mean square residual constants for equation 2.13

Parameter	Description
ρ_0	initial relative density
ρ_f	final relative density
Θ_i	Θ value predicted by sigmoidal curve
Θ_{iavg}	average Θ values from dilatometry measurements
N	number of dilatometry runs

2.5 Master Sinter Surface

The MSC is a useful tool for predicting density during sintering, however, it is possible to add a third axis onto the model and expand its use further [101, 102, 98, 87]. The third axis can be any arbitrary property, though for a practical application to BJAM, the third axis would likely reflect one or a combination of printing parameters. By including the influence of printing parameters into a master sinter surface (MSS), both stages of production (printing and sintering), of any arbitrary values, can be used to determine the final part properties. This is useful for being able to predict final properties, but the curve can also be used in reverse, specifying final properties and deriving the necessary processing parameters. By adding the third axis, a great deal of flexibility is afforded to the user to be able to produce parts in any desired way. The general process of developing the MSS is very straightforward, as the MSS is simply comprised of multiple MSCs. The typical application of the MSS has been to plot two part properties (typically density and another measured property) versus the MSP as opposed to one output versus the MSP and another input. The MSS is flexible enough that either approach can be employed.

2.6 Background Summary

The background chapter provided the information required to fully understand the factors relevant to producing titanium BJAM components. The first section covered the BJAM printing process itself. This consists of an overview of the materials used in the BJAM process, including the powder material as well as both liquid and solid binder materials. The BJAM process overview also covered the main steps throughout the BJAM printing process as well as the critical factors and parameters for each. Next, information relevant for titanium, which is the material of focus for this work, was presented. This includes an overview of different titanium alloys, as well as the composition and general properties of each. Material properties important for sintering are also covered in depth. As part of the section, both titanium and more general powder properties are reviewed to understand their impact on the BJAM process. Next, a review of fundamental sintering principles is presented. This covers both the thermodynamics and kinematics of sintering, and how material and powder properties influence expected outcomes. From the sinter theory review, the MSC concept was discovered and was chosen as the basis of the predictive tool that is one of the objectives of this work. The MSC, its theoretical basis and how it can be created are presented to be able to use it as part of this work.

Chapter 3

Experimental Methods

The work done as part of this thesis relies on three general materials. The first is the titanium powder (material powder) that remains as the final part after sintering. The second and third are the binder materials (both solid and liquid) that are used as part of the BJAM process. For part analysis there are three major categories of work. The first is CT scanning for in-depth part and powder structure analysis. The second and third are dilatometry and DSC analysis that are used in the production of the MSC.

3.1 Materials

3.1.1 Titanium Powder

For the work done in this thesis, all titanium powders used were a plasma atomized, grade 1 commercially pure titanium (Advanced Powders and Coatings, Canada). Three stock powder size ranges were purchased for the production of samples. Two size distributions, 0-45μm and 45-106μm, were used in an unaltered, as-purchased state. The third size distribution, 75-250 μm, was sieved to remove particles larger than 150μm and less than 106μm, using 100 and 140 mesh sizes respectively (U.S.A Standard Test Sieve - Brass, Cole-Parmer, USA), to make a 106-150μm size distribution. The sieving was carried out on a mechanical sieving system conforming to ASTM C136 (model D-4325, Dual Manufacturing Co., USA). The five different powder types used to produce samples are listed in Table 3.1. Two mono-modal powders (Types B and C) as well as three bimodal powders (types A, D and E) were used in the production of samples. The three bi-modal powder distributions were made by blending the three mono-modal distributions at equal weight ratios. Weight measurements for making the bi-modal compositions was done using a precision balance (APX-203, Denver Instruments, USA). The mono-modal 0-45μm powder was not used for the production of samples due to spreadability concerns.

Table 3.1: Titanium powder types and size combinations, with powder blends composed of powder types at equal weight ratios

Powder Designation	Powder Size Composition (μm)
Type A	45-106/106-150
Type B	106-150
Type C	45-106
Type D	0-45/106-150
Type E	0-45/45-106

The chemical composition of the three purchased mono-modal powders conforms to ASTM B348 for a grade 1 commercially pure titanium powder. The exact chemical composition for each material and the relevant testing standard for each element is listed in Table 3.2. The chemical testing was carried out by Luvak Inc. (Boylston, MA, USA) and the chemical information was provided by the powder supplier (Advanced Powders and Coatings).

Table 3.2: Titanium powder chemical composition and testing standards used for analysis

	Content (weight %)				
Element	ASTM B348 grade 1	0-45μm	45-106μm	106-150μm	Test Standard
Carbon	0.08 (max)	0.01	0.01	0.01	ASTM E1941
Oxygen	0.18 (max)	0.14	0.11	0.09	ASTM E1409
Nitrogen	0.03 (max)	0.01	0.01	< 0.01	ASTM E1409
Hydrogen	0.015 (max)	0.004	0.001	0.002	ASTM E1409
Iron	0.20 (max)	0.04	0.05	0.07	ASTM E2371
Other (individual)	0.1 (max)	< 0.1	< 0.1	< 0.1	ASTM E2371
Other (total)	0.4 (max)	< 0.4	< 0.4	< 0.4	ASTM E2371
Titanium	balance	balance	balance	balance	ASTM E2371

3.1.2 Polyvinyl Alcohol Powder

PVA was used as the solid state binder for the production of samples. The PVA used was a low molecular weight, 86-89% hydrolyzed polymer (Alfa Aesar, Ward Hill, MA). The material in its as-purchased condition was in the form of large, irregular and jagged particles that could not be used in the BJAM process. The purchased PVA powder was ground using a blade grinder and was sieved to be less than 63 μm in size using the same sieving method used to obtain the 106-150 μm titanium powder.

3.1.3 Liquid Binder

The liquid binder used to print parts was the standard ZB60 liquid binder produced by 3D Systems (3D Systems, NC, USA). While the exact composition of the material is not provided, the binder is an aqueous solution (approximately 85%-95% water) with some additional polymers as binding agents. From previous works done on the printing of titanium powder, this liquid binder was found to give good results [19].

3.1.4 Mixed Powder for Printing

The powder used for printing was made by mixing each of the five titanium powder blends with the PVA powder. The PVA powder was added to make a mixture with a composition of 3 wt% PVA, with the weighing done using a precision balance (APX-203, Denver Instruments, USA). Mixing was carried out using a previously developed process [19] that entailed placing the titanium and PVA powders in a jar and rotating the mixture on a jar-mill (Labmill 8000, Gardco, USA) at 128 rpm for 4 hours.

3.2 Sample Printing

All samples were produced via BJAM using a modified Z-Corporation 310Plus (Z Corporation - acquired by 3D Systems, NC, USA). All components on the system were still in the original configuration, however inserts were made and installed (see Figure 3.1) that reduced the effective build size of the system. Due to the cost of titanium powder, it was not feasible to fill the standard bed size of the 310Plus, nor was it necessary to produce suitable samples for the subsequent analysis.

The general process for printing the samples was the same as the process described in Section 2.1.1. All printing parameters, shown in Table 3.3 were held constant for the production of all samples. Unfortunately, due to the specific system used, all other parameters were inaccessible to be altered. Printing parameters were held constant to be able to isolate the effects of different powder types. As discussed in Section 2.1.2, the effects of different printing parameters has already been explored. A layer thickness of 150μm was chosen since that is the smallest layer thickness that accommodated the largest particle size. The binder and enclosure temperature values were used from previous works [19] as

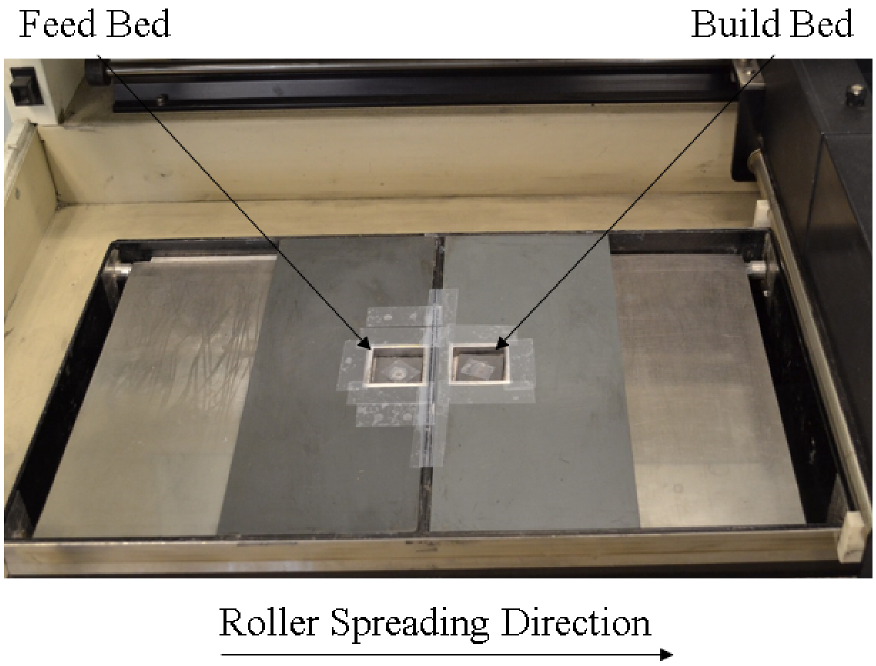

Figure 3.1: Z-Corp 310Plus system showing system modified with bed inserts

they were known to give good print quality by enabling the appropriate rate of evaporation of the liquid binder.

Table 3.3: BJAM printing parameters used in the ZPrint software for sample production

Parameter	Value
Layer thickness	150 μm
Shell binder amount	100 %
Core binder amount	200 %
Enclosure temperature	40 ℃
Drying time (after printing)	1 hour

The stereolithography (STL) file used for the production of samples was also held constant for all prints. The print file consisted of 16 cylinders, each being 5 mm in diameter and 8 mm in height. This sample size was chosen so that one sample type could be used for both sinter structure analysis using computed tomography (CT) as well as for the creation of the MSC using a dilatometer. The cylinders were placed in a 4 by 4 array, with the samples evenly spread out in the build bed. A wall was placed at the back of bed (with respect to the roller spreading direction) since it was found to improve the quality and consistency of the powder layer and spreading over the cylinders during printing. The print file dimensions and its position in the build bed are shown in Figure 3.2.

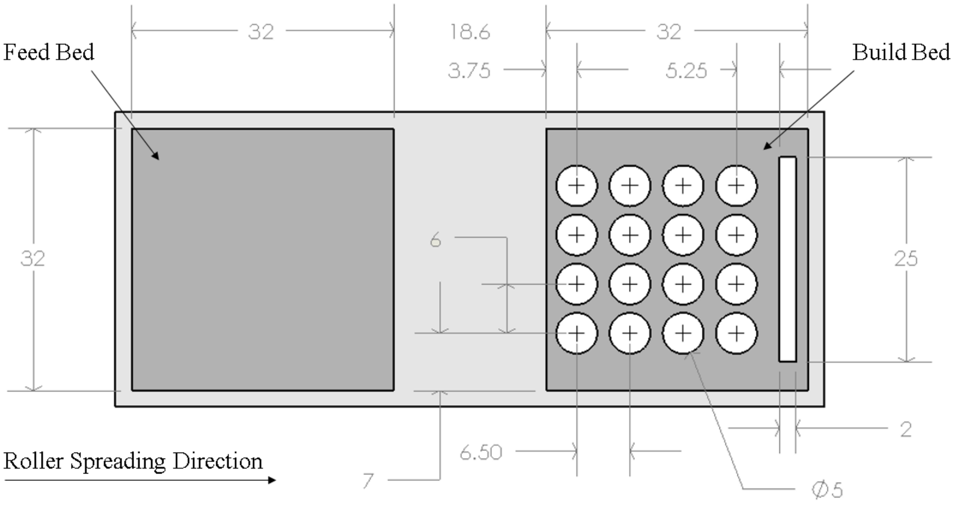

Figure 3.2: Build file dimensions showing the samples and wall in the build bed on the right with the feed bed on the left

All of the green samples, shown in Figure 3.3, had a sufficiently high level of build quality (dimensional accuracy and consistency as well as strength) to be used for further analysis.

Figure 3.3: Qualitative comparison between the build quality of the different sample types made from powder types (from left to right) A, B, C, D and E

3.3 Sinter Structure Analysis

As discussed earlier, the two different types of sintering, densifying and non-densifying, each produce a significantly different sinter structure due to the specific sintering mechanisms active in each. An experiential procedure was carried out to understand the significance of the effects from both types of sintering. Analysis was first performed on a set of green parts that then underwent sintering to produce a specific sinter structure. The same analysis was then performed on the same set of parts (now sintered) to determine the effects of sintering on porosity, sinter neck size, pore size and particle size.

3.3.1 Sintering Parameters

Two different sintering schedules were used to sinter parts either in the non-densifying or densifying domain. The specific schedules for non-densifying and densifying sintering are shown in Figure 3.4. All sintering was carried out using a high-temperature tube furnace (GSL1500X-50, MTI Corporation, USA), with samples placed uncovered in high purity alumina crucibles (EQ-CA-L100W20H20, MTI Corporation, USA). For both sintering schedules (shown in figure 3.4), binder burnout was carried out in air while sintering was carried out under a high-purity argon atmosphere. The samples were brought back down to room temperature after binder burnout to be able to attach end caps on the tube furnace to seal the system for sintering under an argon atmosphere.

Hold temperatures for sintering were chosen as 1000 ℃ and 1400 ℃ for non-densifying and densifying sintering respectively. Sintering of titanium only begins in any substantial way above the alpha-beta transition temperature, approximately 880 ℃ [68]. The 1000 ℃ temperature was chosen to be slightly above that minimum temperature to allow sintering to occur at a reasonable rate but to ideally only allow non-densifying sintering mechanisms to be active. The 1400 ℃ temperature was chosen as it was the highest continuous sintering temperature possible in the furnace. While limited by the capabilities of the furnace, this temperature (268 ℃ below melting) was deemed sufficiently high to perform densifying sintering. A hold time of 10 hours was chosen to ensure the two types of sintering had proceeded sufficiently far enough for analysis.

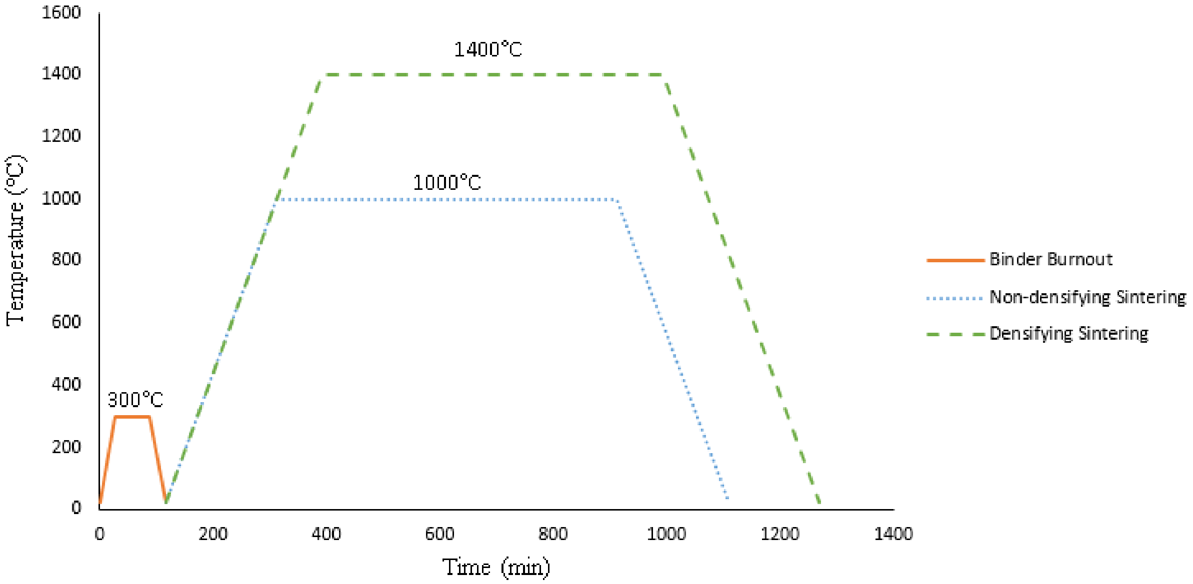

Figure 3.4: Sintering schedule for densifying and non-densifying sintering process

Ten samples were used as part of the analysis, being evaluated in both a green and sintered state. A summary of the parts and their respective sinter schedules is shown in

Table 3.4. The green sample masses shown in Table 3.4 are compensated for the assumed 3wt% of PVA. The differences between the green and sintered sample masses is minimal and likely due to measurement error, variations in PVA amount and the loss of loose powder during handling.

Table 3.4: Sample summary for sinter structure analysis. The CT samples are identified with A, B, C, D and E as the part powder type and H and L representing the 1400℃ and 1000℃ sintering regime respectively.

Sample Name	Powder Type	Green Mass (g)	Sintered Mass (g)	Sintering Temperature (℃)
CT-AL	Type A	0.455	0.456	1000
CT-AH	Type A	0.441	0.447	1400
CT-BL	Type B	0.460	0.462	1000
CT-BH	Type B	0.460	0.456	1400
CT-CL	Type C	0.390	0.391	1000
CT-CH	Type C	0.386	0.394	1400
CT-DL	Type D	0.380	0.404	1000
CT-DH	Type D	0.443	0.450	1400
CT-EL	Type E	0.377	0.377	1000
CT-EH	Type E	0.364	0.380	1400

3.3.2 Computed Tomography

Evaluation of the effects of the different sintering types was carried out using CT. While other, more conventional metallurgical analysis methods, such as scanning electron or optical microscopy were available, they were deemed unsuitable. While these methods do provide useful data, they are limited to small regions of interest and can only provide information on the outer, visible surface of the parts. The CT scanning (Xradia 520 Versa, Zeiss, USA) was performed using the same parameters in the Scout-and-Scan software (see Table 3.5) for both the green and sintered parts. This was done to ensure a consistent voxel size for both scans to be able to perform the same automated analysis both before and after sintering. Due to an operator error, samples CT-CL and CT-CH were scanned at 3.716μm while all other samples were scanned at 3.807μm. This difference in voxel size was deemed to be negligible for the subsequent analysis.

Table 3.5: Scout-and-Scan settings used for CT scanning

Parameter	Value
Source power	10W
X-ray energy	120kV
Filter	HE1
X-ray optic	4x lens
Source position	-15.88mm
Detector position	12.27mm
Exposure time	1.5 s
Number of projections	1201
Binning level	2
Voxel size (approximate)	3.8μm

Samples were scanned two at a time, with the samples stacked vertically in a sample holder. The samples were spaced using paper since the material has a significantly lower attenuation, allowing both samples to be easily distinguished from each other. Samples also had a chamfer cut on the top surface to allow for consistent alignment of the part to the orthogonal axes after being scanned. Once the CT scans were complete, reconstruction of the projection images was completed using the Zeiss Reconstruction software package to produce a series of gray-scale images with 16-bit intensity ranges. Subsequent image processing of these images was performed using ImageJ. The 16-bit images were scaled to an 8-bit range and then byte scaling was applied to normalize the 8-bit intensity values to be between 0 and 255. This was done to be able to apply a single thresholding value for green and sintered parts during segmentation. Before segmentation was done, an edge preserving bilateral filter was applied (spatial radius of 2 and intensity range of 50) to normalize the noise in the reconstructed images. Each of the reconstructed image sets was manually aligned with the orthogonal axes of the scanner. The orientation of the scanner axes with respect to the printed parts is shown in Figure 3.5, with the Z axis of the CT scanner corresponding to the build direction.

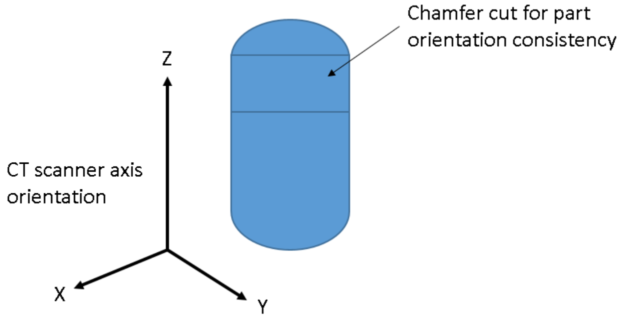

Figure 3.5: Orientation of the printed cylinders with respect to the CT scanner axes

To isolate the parts from any loose powder particles inside the sample holder, a maximum intensity projection (MIP) of each image set was created. This projected the voxel with the highest attenuation value onto a single two-dimensional image for the entire image set. This allowed for the outer profile of the sample to be determined, even though the samples were not perfectly aligned with the Z axis. The MIP, as well as the resulting selection area (red outer boundary), for the CT-BL green parts is shown in Figure 3.6.

Segmentation of the images was completed using the sample masses and material densities. Based on a titanium density value of 4.506 g/cm^3, the segmented sample volumes were multiplied by the density of titanium to obtain the sample mass. The mass was assumed to be 97% titanium and 100% titanium for the green and sintered parts respectively. Due to the significantly lower attenuation value of PVA, the material was not visible in any of the gray-scale images. It was therefore assumed that it would not contribute to the size of

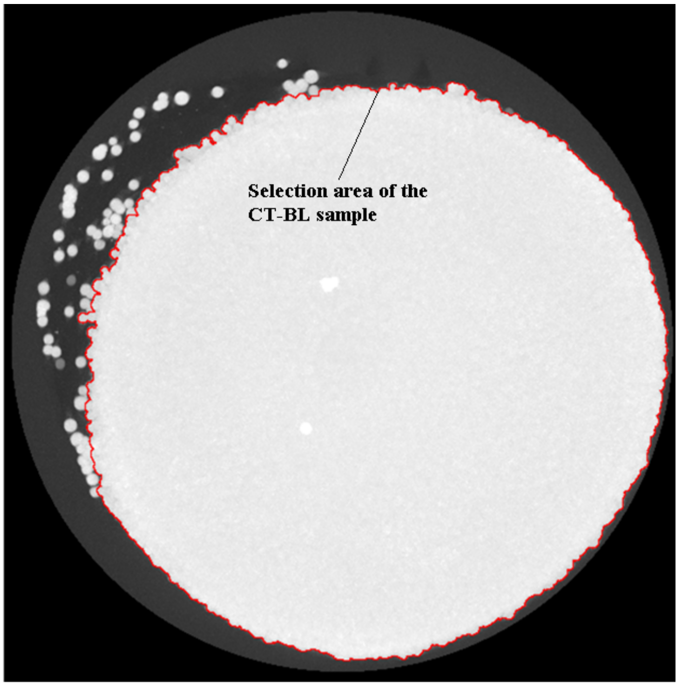

Figure 3.6: Maximum intensity projection image and resulting selection area (red boundary) of the CT-BL green part

the segmented section of the green samples. Determination of the thresholding values was done on samples CT-AH and CT-BL due to larger particle sizes and lower particle density simplifying the analysis. Thresholding values of 138 and 143 were found for the green and sintered parts respectively. Figure 3.7 shows a gray-scale slice of the CT-AH green part and corresponding segmented image. The segmented images were then subsequently used for part analysis.

Analysis of the CT image sets consisted of finding four major parameters: relative density, particle size, pore size and sinter neck size. All values were found on a per-layer basis, with the average of those giving the overall value for the entire part. It was determined to be unfeasible to analyze the entirety of each sample so a 1.25mm x 1.25mm x 2.25mm region of interest (ROI) was used for the green samples. The ROIs were scaled

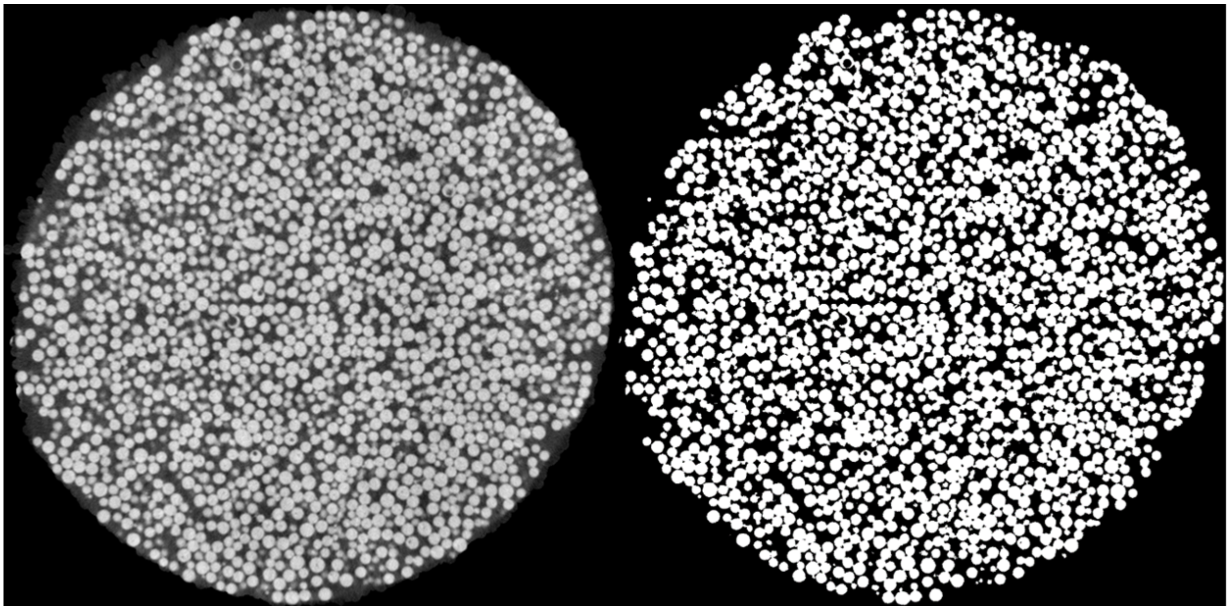

Figure 3.7: Gray-scale (left) and segmented image (right) of a slice of the CT-AH green part

equal to the amount of shrinkage seen in each sample after sintering to capture the same particles in the analysis. The long axis of the ROI was aligned parallel to the build direction (Z axis) to be able to better capture a larger number of layers in the analysis. The relative density was calculated by comparing the area of the particle space (found by segmentation), to that of the overall layer. Analysis used to determine the part features (porosity, pore size, particle size, sinter neck) was carried out by the company Expanse Microtechnologies, with a detailed description included in Appendix F.

Due to the voxel size the parts were scanned at, sinter neck sizes below 50μm could not be reliably detected. Due to this, a measured sinter neck below 50μm, cannot be said to definitively exist and cannot be used in calculations for overall sinter neck statistics. This is problematic since the sinter necks are expected to be significantly smaller than this, especially for the powder blends containing the finer particles (0-45μm) and parts sintered at 1000℃ where limited sinter necks will form. It was decided that, due to the large gap in reliable measurements from the CT analysis, only a qualitative inspection of sinter necks from cross-sections and reconstructions of the CT data would be made.

3.4 Master Sinter Curve

3.4.1 Dilatometry

To create the MSC, samples were measured on a push-rod type dilatometer (DIL 402C, Netzsch, Germany). The specific model of dilatometer used was not fully gas sealed and only provided gas shielding. Before a full experimental plan was run, the adequacy of the gas shielding was tested. To do this, two samples were run in the dilatometer at a rate of 10 ℃/min up to 1550 ℃. The dilatometer was not calibrated and no shrinkage measurements were taken for the sintering runs. One sample was run with only the gas shielding while another sample was placed in a sapphire crucible with a sapphire plug (SP-62400 and SP-C-RD-U, AdValue Technology, USA). The part placed in the sapphire crucible was found to have sintered with minimal oxidation, while the part protected only by the shielding gas was found to be nearly fully oxidized (see Figure 3.8). From the results of this test, all successive dilatometer measurements were performed on the samples placed in the sapphire crucibles.

As discussed in Chapter 2.4.2, multiple dilatometry measurements (each done at a different heating rate) are required to create a MSC. The dilatometer used for measurements has a maximum temperature of 1600 ℃ so a peak temperature of 1550 ℃ was chosen to prevent possible damage to the system. The sintering schedule for the dilatometry experiments is shown in Figure 3.9. Three heating rates of 3 ℃/min, 5 ℃/min and 10 ℃/min

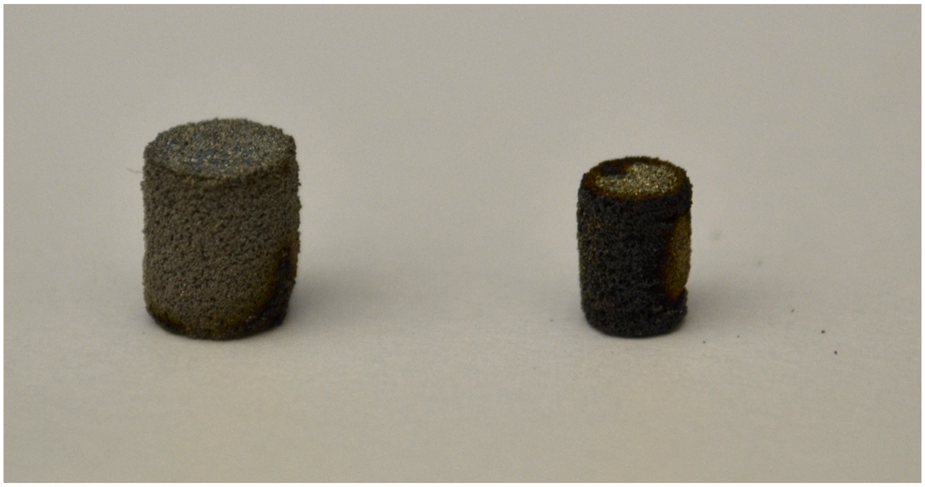

Figure 3.8: Comparison between samples sintered inside a sapphire crucible (left) and with only gas shielding (right)

were chosen for the experiments. The lowest rate of 3 ℃/min was initially chosen to prevent the possibility of parts undergoing excessive surface diffusion (causing coarsening rather than densification to occur) as this violates one of the MSC assumptions and can give inaccurate results [81]. The two other rates were chosen since they were significantly different from the slowest rate as well as each other while still providing a sufficient amount of sintering. The heating rates must create significantly different densification profiles to be able to determine the correct apparent activation energy (Q). If the densification profiles are not sufficiently dissimilar the plotted data will inherently overlap, regardless of the Q value used for the MSC creation. By being significantly different, the correct Q value can be found. A rate of 20 ℃/min for cooling was chosen since it is the fastest cooling rate the dilatometer allows. This fast cooling rate prevents a appreciable amount of sintering from occurring during coo down and allows for the measurement of the coefficient of thermal expansion (CTE), represented as α_l, of the parts [82, 84]. The CTE of the part is required to correct the dilatometer measurements to isolate dimensional change due to sintering.

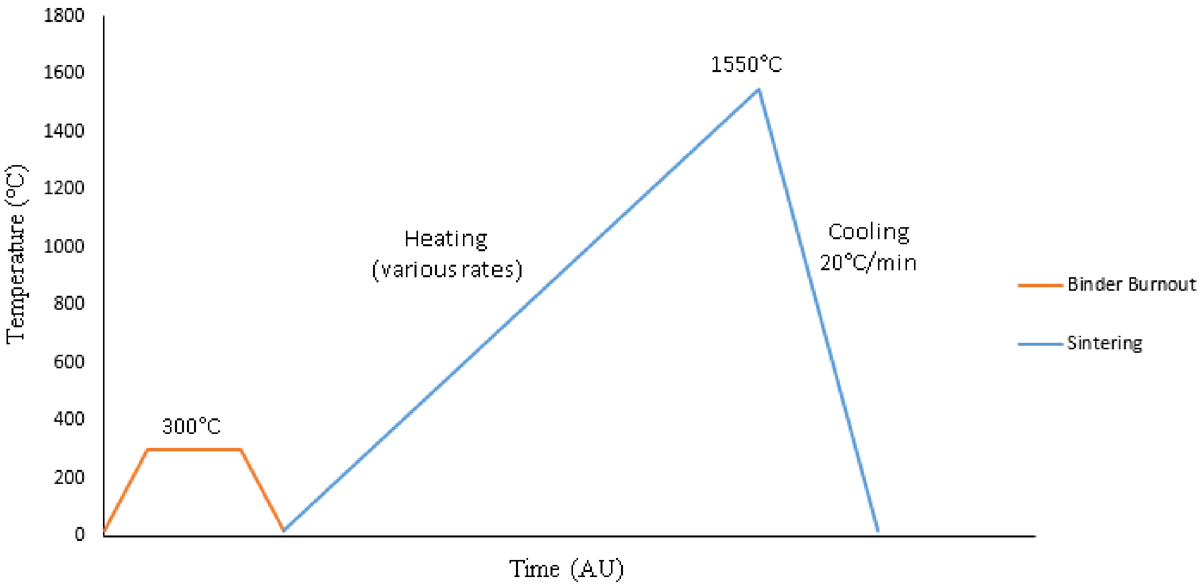

Figure 3.9: Dilatometry measurement sintering schedule

3.4.2 Dilatometry test Run

Before sintering the entire set of samples, a single dilatometry sintering run on samples made using the type C powder was performed to ensure adequate measurements could be achieved with the system for the entire sintering schedule and for all of the heating rates. From these preliminary sintering runs, shown in Figure 3.10, significant issues with the measurements were found. The data in Figure 3.10 shows the shrinkage data versus sintering temperature, with the shrinkage values not corrected to compensate for the CTE. For a specific temperature in the sintering run, it is expected that the 3 ℃/min sintering run would show the highest level of shrinkage, since it takes the most time to reach that temperature (and therefore has been sintering longer). From Figure 3.10 it can be seen that the 3 ℃/min shows the lowest level of shrinkage. It would also be expected that the 10 ℃/min sintering run would show the least shrinkage, since it has had the least amount of time for sintering. Instead, the 10 ℃/min sample shows the highest level of shrinkage, with the 5 ℃/min sample showing only slightly lower amounts of shrinkage. While the shrinkage measurements appeared to be unusable, all three sintering runs showed approximately the same linear slope from a temperature of 1400℃ back down to 227℃, which is where the system stopped taking measurements. This confirmed that it was possible to use this section of the data to compensate for the CTE.

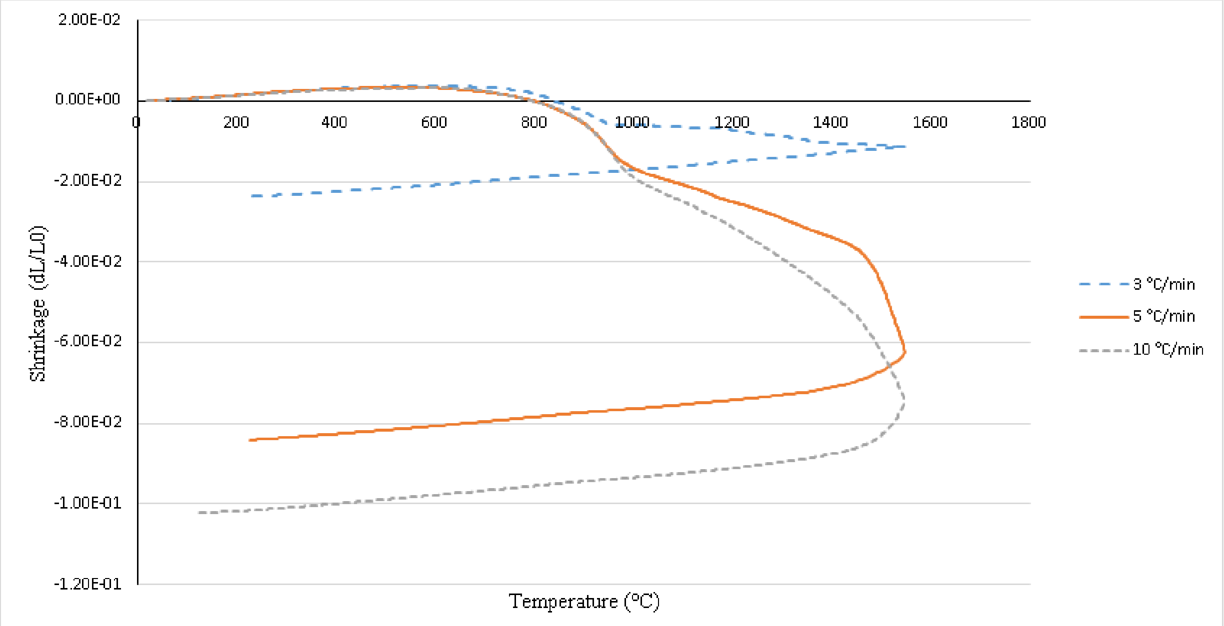

Figure 3.10: Preliminary dilatometry sintering runs at 3℃/min, 5 ℃/min and 10 ℃/min of type C powder samples

To investigate the results from the preliminary dilatometry tests, the data was corrected by calculating and applying expansion caused by thermal expansion. The CTE was calculated over the temperature range of 1400 ℃ to 227 ℃, with 227 ℃ being the temperature that the dilatometer stopped taking measurements at during cool down. The equation used for the CTE calculation is shown in Equation 3.1 with the results summarized in Table 3.6. An average CTE value of 10.67 $10^{-6}k^{-1}$ was found, matching closely to other high temperature titanium CTE values [103].

$$CTE_{linear} = \frac{\frac{dL}{L_0}_f - \frac{dL}{L_0}_i}{T_f - T_i} \tag{3.1}$$

Table 3.6: CTE values found for the type C powder samples during preliminary dilatometry sintering runs

Sintering Run	CTE ($10^{-6}k^{-1}$)
3 ℃/min	9.25
5 ℃/min	11.24
10 ℃/min	11.52

The raw dilatometry data was plotted and corrected for CTE using Equation 3.2 and the converted to density using Equation 3.3, with the results shown in Figure 3.11. A relative green density of 50% was used for three samples for calculating shrinkage during the dilatometer sintering runs. This value was found using a measure and weigh method for ten samples and then averaging the results. This average value was confirmed using CT scanning analysis, as discussed in 3.3.2. The final densities of the parts was also found using a measure and weigh method, with the values compared to the dilatometer measurements in Table 3.7.

From Table 3.7, it can be seen that both the 5 ℃/min and 10℃/min samples showed inaccurate density measurements from the dilatometer. The density values found for the 3 ℃/min sample were the same from both the measure and weigh method as well as the dilatometer. The excessive densification values seen in the 5 ℃/min and 10 ℃/min samples was found, through SEM analysis (Zeiss UltraPlus, Zeiss, Germany), to be due to localized surface compaction from the push-rod during sintering. During the 5℃/min and 10℃/min sintering runs, neither sample would have developed appreciably large, if any, sinter necks before reaching elevated temperatures. This meant that the samples were not rigid enough to withstand the applied push-rod forces when the material became softer at higher temperatures. The 3 ℃/min sample had more sintering time before reaching higher temperatures, allowing for the sample to develop larger sinter necks and therefore be rigid enough to withstand the applied forces. The issue with excessive distortion in shrinkage measurements is not entirely unexpected, as other groups have found difficulties measuring highly porous samples with a push-rod type dilatometer [104].

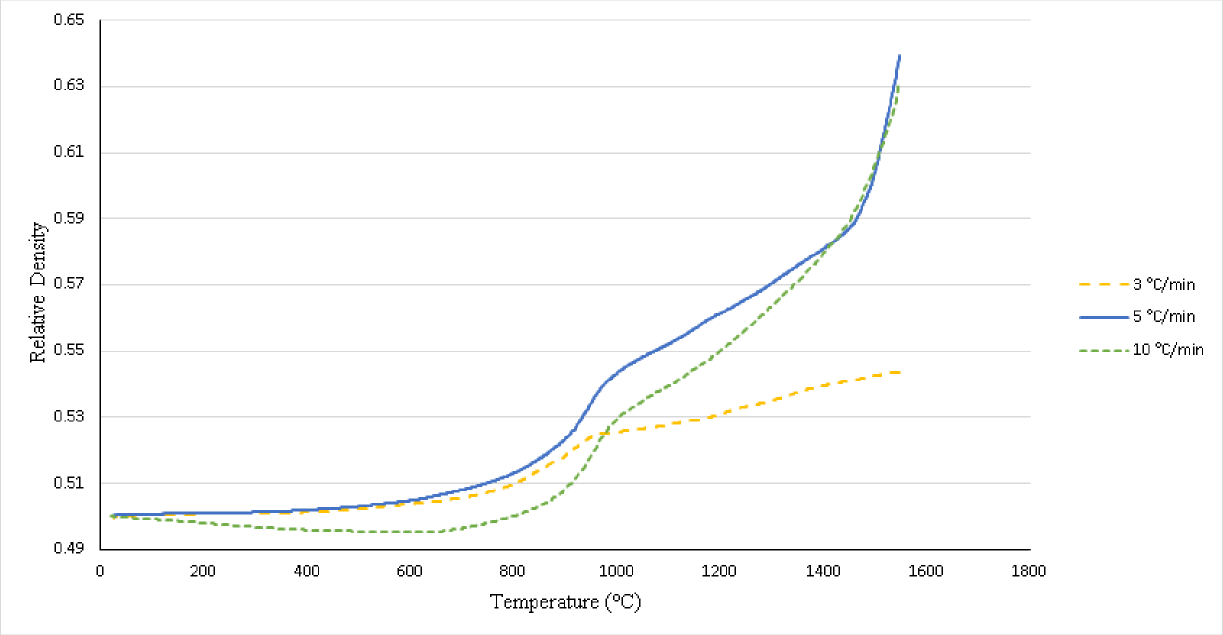

Figure 3.11: Corrected preliminary dilatometry sintering runs at 3℃/min, 5 ℃/min and 10 ℃/min

$$\frac{dL}{L_{0\ s}} = \frac{dL}{L_{0\ m}} - \alpha_l \Delta T \tag{3.2}$$

$$\rho_r = \rho_0 \left(\frac{1}{1 - \frac{dL}{L_0}_s} \right)^3 \tag{3.3}$$

Table 3.7: Comparison between part densities found from dilatometery and measure and weigh method

Sintering Run	Dilatometry density (%)	Measure and Weigh density (%)
3 ℃/min	54.3%	54.6%
5 ℃/min	65.7%	57.3%
10 ℃/min	69.1%	56.5%

As can be seen from Figure 3.12 the 5℃/min sample shows a highly dense and compacted end surface, while the rest of the part is still highly porous. The 3 ℃/min sample on the other hand, shown in figure 3.13, shows a uniform surface with no localized compaction. The 10 ℃/min also showed a significant amount of surface compaction, at similar levels to the 5 ℃/min sample. With two of the three samples providing very poor information, they cannot be used to create the MSC. Due to this, a heating rate of 1℃/min was selected, in conjunction with the 3℃/min heating rate, to create the MSCs. Though it is preferable to use at least three heating rates, as it allows for a more accurate calculation of Q, groups have successfully created MSCs using only two heating rates [94]. Since the 1℃/min heating rate will cause the sample to undergo more sintering than the 3℃/min sample before getting to an elevated temperature, it is expected that there will be no distortion in the shrinkage measurements.

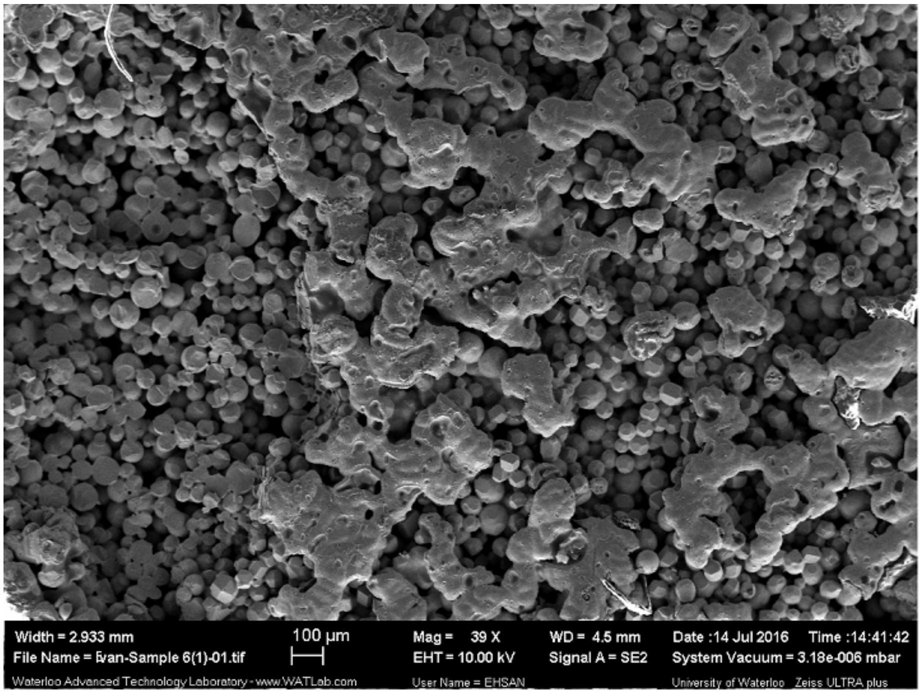

Figure 3.12: SEM image showing the excessive surface compaction of the end face of the 5℃/min sample after sintering

3.4.3 Dilatometry Analysis

From these preliminary experimental results, it was decided that the MSCs for each powder type will be derived from two heating rate experiments performed on the push-rod dilatometer. Table 3.8 shows a summary of the sample names, powder types and respective heating rates used during the dilatometry experiments.

3.4.4 Differential Scanning Calorimetry

As discussed in 2.4.2, the multiple experiments run on the dilatometer are only required to find the correct Q value for the MSC. This method is done predominantly for the sake of

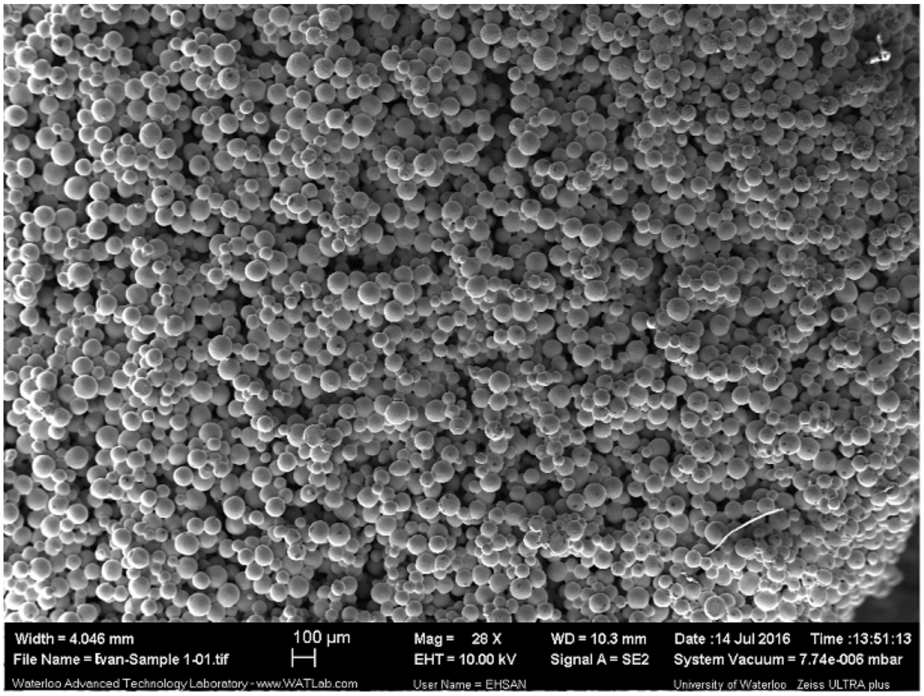

Figure 3.13: SEM image showing no excessive compaction of the end face of the 3℃/min sample after sintering

Table 3.8: Sample summary for dilatometry analysis. The dilatometry (DIL) samples are identified with A, B, C, D and E as the part powder type and 1 and 3 representing the 1℃/min and 3℃/min heating rates respectively.

Sample Name	Powder Type	Heating Rate (℃/min)
DIL-A3	Type A	3
DIL-A1	Type A	1
DIL-B3	Type B	3
DIL-B1	Type B	1
DIL-C3	Type C	3
DIL-C1	Type C	1
DIL-D3	Type D	3
DIL-D1	Type D	1
DIL-E3	Type E	3
DIL-E1	Type E	1

convenience, since only one system (a dilatometer) is required to make measurements. A differential scanning calorimeter (DSC) can also be used to find Q. However, either multiple isothermal [105] or constant heating rate [105, 106, 107] sintering experiments must be run to find an accurate value. Since this technique provides no substantive benefit, and requires substantially more experiments to be run, the DSC was not used to find the Q values for the different powder types. Regardless, samples were run on a DSC to see if there was any noticeable difference in measured energies between the different powder types during sintering.

All samples were run on a DSC (DSC 404C, Netzsch, Germany) inside covered alumina crucibles. Gas flow was supplied to the system through an oxygen scrubber. Though the DSC system was not gas sealed, no substantial oxidation of the parts was observed. Samples were heated at a rate of 3℃/min to mimic the dilatometer sintering experiment. Samples were heated to a maximum temperature of 1200℃ to prevent excessive wear on the DSC. All samples underwent the same binder burnout procedure as the dilatometer samples before being run on the DSC. The same samples used for the dilatometer experiments were used for the DSC, but were cut to have a height of approximately 3.5mm to be able to fit inside the crucibles. These sample masses, measured using the same process as the dilatometer samples and shown in Table 3.9, are significantly larger than what is typically recommended for DSC runs. The larger sample size was chosen to ensure the powder samples remained coherent during handling and binder burnout. A solid piece of grade 2 CP titanium (PartNo. 89145K54, McMaster-Carr, USA) was machined to have the same weight as the average weight of the powder samples and underwent the sample analysis. All of the energies associated with the solid titanium piece should have been due to reversible processes (heating, phase change, etc.), while the powder samples would have both reversible and irreversible processes, namely sintering. The difference between the measurements of the solid and powder samples should isolate all of the measured energy associated with sintering.

Table 3.9: Summary of DSC samples and masses. The DSC samples are identified with A, B, C, D and E as the part powder type and S identifying the solid sample.

Sample Name	Powder Type	Sample Mass (g)
DSC-A	Type A	0.176
DSC-B	Type B	0.163
DSC-C	Type C	0.182
DSC-D	Type D	0.169
DSC-E	Type E	0.192
DSC-S	Solid	0.177

Unfortunately the DSC measurements, shown in Appendix E, were inconclusive. There were an number of thermal processes that were observed but were not fully understood. A significant endothermic process occurred from approximately 400℃ to 800℃, with a peak value at 600℃. The measured thermal values could not be associated with oxidation (an exothermic process), but could possibly be due to evaporation or further degradation of the binder or its decomposed products. An endothermic peak is seen for both the powder and solid samples at approximately 880℃, which is associated with the alpha-beta phase change. For the powder samples, the peak falls on an endothermic ramp, partially obscuring them. Once the phase change is over, the solid sample heat flow values fall and then level out to a stable value. The powder samples still show high endothermic heat flow values past the alpha-beta transition, but with the values showing a downward (exothermic) trend towards the solid part value. The solid part showed significantly larger energy values compared to the powder samples for the alpha-beta transition, with the applied correction giving the powder samples a large exothermic peak at the phase change. Unfortunately, there was no noticeable trend between any of the powder types, nor did the correction using the solid part give any meaningful results. The poor measurements from the DSC were likely due to excessively large samples being used in addition to the sample masses being significantly different.

3.5 Experimental Methods Summary

Five powder types were used to create the samples as part of this work. Two mono-modal (45-106μm and 106-150μm) and three bi-modal powders (45-106/106-150μm, 0-45/45-106μm and 0-45/106-150μm) were made using standard, commercially available powder size distributions. The 106-150μm distribution was made be sieving out the range from a purchased 75-250μm distribution. Printing properties developed from previous studies and work completed in the group were held constant so that only the impact of the powder is analyzed as part of this work. CT analysis was completed on samples in the green state as well as after sintering. This is done so that differences can be seen for the same parts and the same ROI. An analysis of density, particle size, pore size, and sinter neck size was subsequently done using the CT data.

Preliminary tests to create a MSC curve were completed to ensure adequate measurements could be made using the printed samples and the available equipment. It was found that the shielding gas in the dilatometer is insufficient to protect the samples during sintering. A sapphire crucible and plug were used to shield the parts, successfully preventing oxidation. Dilatometry runs at 3℃/min, 5℃/min and 10℃/min were carried out in the sapphire crucibles to evaluate the measurements made on the system. From the results, it was found that the 5℃/min and 10℃/min heating rates provide inaccurate results. The sample ends that were in contact with the push-rod were compacted, making the dilatometer measurements show the samples as having higher density values than they actually did. This excessive compaction is likely due to the samples having smaller sinter necks at the faster heating rates, making the samples weaker and more susceptible to compaction forces from the push-rod. The 3℃/min sample did not show excessive compaction of the ends, providing accurate density measurements. To make the MSC, a second heating rate of 1℃/min was chosen since the sample sintered at this rate would also have sufficiently large sinter necks to mitigate compaction forces. DSC measurements were completed on samples to see if there were any notable differences between the behaviors of the different powders. The results were inconclusive, and not utilized for any subsequent analysis.

Chapter 4

Results and Discussion

The results from the various analysis techniques and subsequent discussion are split into two main themes. The first is the sinter structure analysis, looking at the combined effects of different powder sizes and both densifying and non-densifying sintering mechanisms. Evaluation of the sinter structure results relies predominantly on the CT scan data. The second is the generation of the MSCs for the different powder types. Generation and evaluation of the MSCs is completed using the dilatometry data.

4.1 Sinter Structure

Analysis of both the green and sintered structure was completed on the segmented images, with the segmentation process being discussed in Chapter 3.3.2. Four main features were evaluated for both the entire part and on a per-layer basis and include: porosity, particle size, pore size and sinter neck size. As discussed earlier, the sinter neck size measurements were not used due to poor reliability. Quantitative results are only presented for porosity, pore size and particle size. Overall reconstructions of the samples can be seen in Appendix D. Samples were sintered at both high and low temperatures to be able to see the combined effects of powder size and the two main groups of sintering mechanisms (densifying and non-densifying).

4.1.1 Porosity

The bulk porosity results of the samples in both the green and sintered state are summarized in Table 4.1. All samples of the same powder type show essentially the same green density apart from samples CT-DH and CT-DL, which have a difference in green density of 4.9%. This difference is likely due to inconsistencies either in the powder or printing process. The general trend seen with the samples is that as the average particle size decreases, so does the green density. Powder type B gives samples with the highest green density, followed by type A, type D, type C and finally by type E, giving the lowest green density. This trend is likely due to the number of contact points in the various powder systems and compaction forces during printing. Since all of the parts were printed on the same system with the same settings, all of the parts would have undergone the same applied compaction forces during printing. However, due to the variation in powder sizes, the friction and inter-particle electrostatic forces in the different powder systems are not the same. As discussed in Chapter 2.2.2, powder systems with smaller particles have more contact points, making the powder more resistive to applied forces due to friction as well as being more susceptible to electrostatic forces [54, 55, 40]. Therefore, with the same applied compaction forces (from either a roller or blade spreading the powder), but with larger friction forces, it was expected that the powder systems with smaller particles would see lower density levels. The trend seen from these results is similar to that seen in other works [40, 53, 34].

Table 4.1: Summary of the bulk densities of the CT sample ROIs in the green and sintered state as well as the density changes

Sample Name	Green Density (%)	Sintered Density (%)	Density Change (%)
CT-AL	54.8	57.7	2.9
CT-AH	54.4	64.6	10.2
CT-BL	58.3	59.1	0.8
CT-BH	57.6	71.5	13.9
CT-CL	49.6	53.5	3.9
CT-CH	47.9	70.5	22.6
CT-DL	48.1	60.3	12.2
CT-DH	53.0	84.6	31.6
CT-EL	45.5	57.2	11.7
CT-EH	45.9	82.7	36.8

As expected, the parts sintered at 1000℃ underwent significantly less shrinkage compared to the parts sintered at 1400℃. As discussed in Chapter 3.3.1, it was expected that the samples sintered at 1000℃ would only undergo non-densification sintering and therefore have a maximum shrinkage of around 3%. It was also expected that the parts sintered at the lower temperature would remain in the initial stage of sintering where only non-densifying sintering occurs. From the CT results, it can be seen that this is only true for samples CT-AL, CT-BL and CT-CL, which showed shrinkage levels of 2.9%, 0.8% and 3.9% respectively. For these samples, the sinter necks generally appeared to stay below the 1/3 the particle diameter threshold, as shown in Figure 4.1. Based on sinter neck size and the level of density change, all three of the samples remained within the initial stage of sintering, and only underwent non-densifying sintering.

As discussed earlier, the energy required for sintering decreases exponentially with particle size. This is true both for densification and non-densification sintering. This expected trend is confirmed for the shrinkage levels seen in the samples with CT-BL showing the

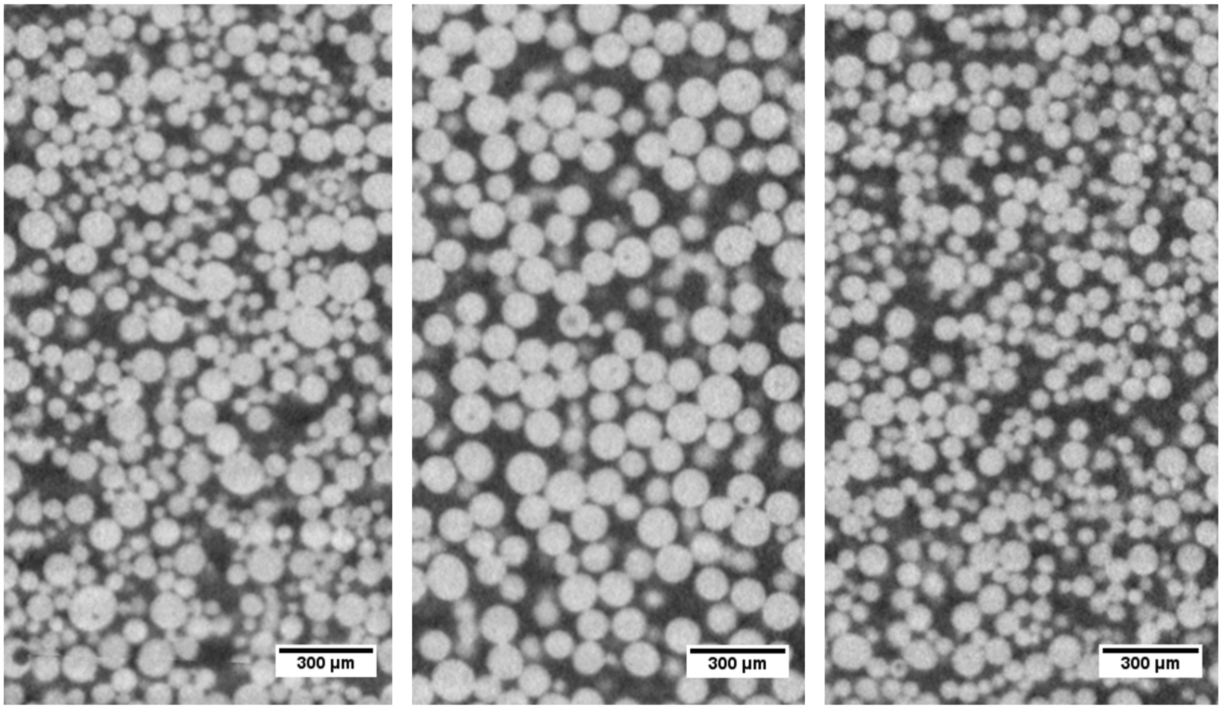

Figure 4.1: XZ plane cross-section images from reconstructed CT data of samples CT-AL (left), CT-BL (centre) and CT-CL (right) in the sintered state showing a qualitative view of the sample sinter necks between particles in the ROI

lowest and CT-CL the highest level of densification of the parts that underwent only non-densifying sintering. The minimal density change of samples CT-AL, CT-BL and CT-CL demonstrate that the titanium BJAM parts can be sintered with minimal dimensional change but still have sinter necks large enough to be distinguished within the powder system. A lack of dimensional change during sintering means that there needs to be either little to no compensation of the part size during printing (to get the desired size after sintering). While it is simple to predict the final size of relatively large and simple parts and features, it becomes more difficult as size decreases and complexity increases. If the green part density can be made high enough to be suitable for a specific application, the parts could be sintered at this lower temperature, negating the need for any form of compensation.

Both CT-DL and CT-EL samples showed significant levels of densification of 12.2% and 11.7% when sintered at 1000℃, indicating the parts underwent densification sintering. This higher level of shrinkage is due to the addition of the very fine particles that require significantly less energy for sintering. Based on the sinter neck sizes of the samples, shown in Figure 4.2, the sample appears to have undergone both densifying and non-densifying sintering, but with each localized to the smaller (0-45μm) and larger (45-106μm and 106-150μm) particles groups respectively. From Figure 4.2, the sinter necks between the larger particles is comparable to those seen in samples CT-AL, CT-BL and CT-CL, indicating only non-densifying sintering. The relative size of the sinter necks seen between the smaller particles is significantly larger. Most of the particles show sinter necks larger than the 1/3 diameter ratio, indicating they have progressed, at least locally, into the intermediate sintering stage where significant densification occurs. This indicates that the majority of the shrinkage seen in the sample was caused only by the smaller particles. It also shows that the very fine particles undergo densifying sintering even at 1000℃.

The sinter results seen for CT-DL and CT-EL are important for two reasons. First, any addition of these very fine particles can cause unanticipated levels of shrinkage. The blending of large and very fine particles is a suitable means of achieving high green density [34, 53]. However, this may be detrimental if the intent is to have little-to-no shrinkage during sintering. The other important aspect shown through these results is that the addition of the fine particles allows for sintering at comparatively low temperatures. Due to the significantly lower activation energy, the very fine particles expands the temperature range in which the BJAM titanium parts can be sintered. Low-temperature furnaces are more common and less expensive than similarly sized high-temperature furnaces, and tend

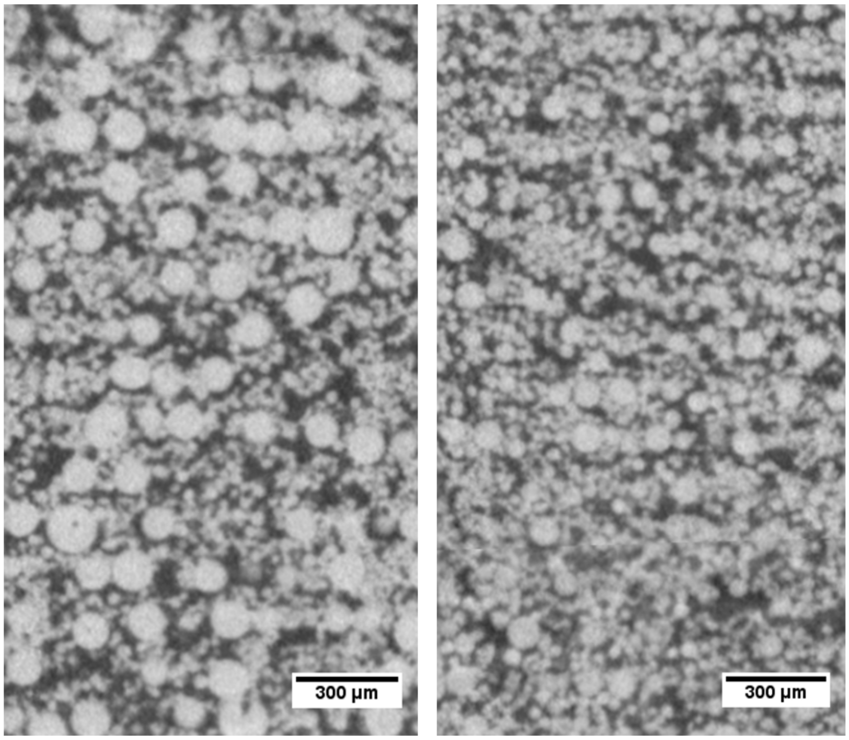

Figure 4.2: XZ plane cross-section images from reconstructed CT data of samples CT-DL (left) and CT-EL (right) in the sintered state showing a qualitative view of the sample sinter necks between particles in the ROI

to be cheaper to operate. This would allow for a more economical sintering process with similar densification results.

The parts sintered at 1400℃ underwent much higher levels of shrinkage during sintering. All of the parts underwent signification levels of shrinkage, indicating that densification sintering mechanisms were dominant. Similar to sintering at 1000℃ however, there were two distinct groups of parts based on the amount of shrinkage seen. Samples CT-AH, CT-BH and CT-CH had densification values of 10.2%, 13.9% and 22.6% respectively, while samples CT-DH and CT-EH had densification values of 31.6% and 38.6%. The 1400℃ sintering treatment brought samples CT-AH, CT-BH and CT-CH either close to, or just above the 70% theoretical density threshold that indicates the samples progressed, or were in the midst of progressing, into the intermediate stage of sintering. This is also indicated by the sinter necks of the samples, shown in Figure 4.3, that are generally in the range of 1/3 to 1/2 the particle diameter.

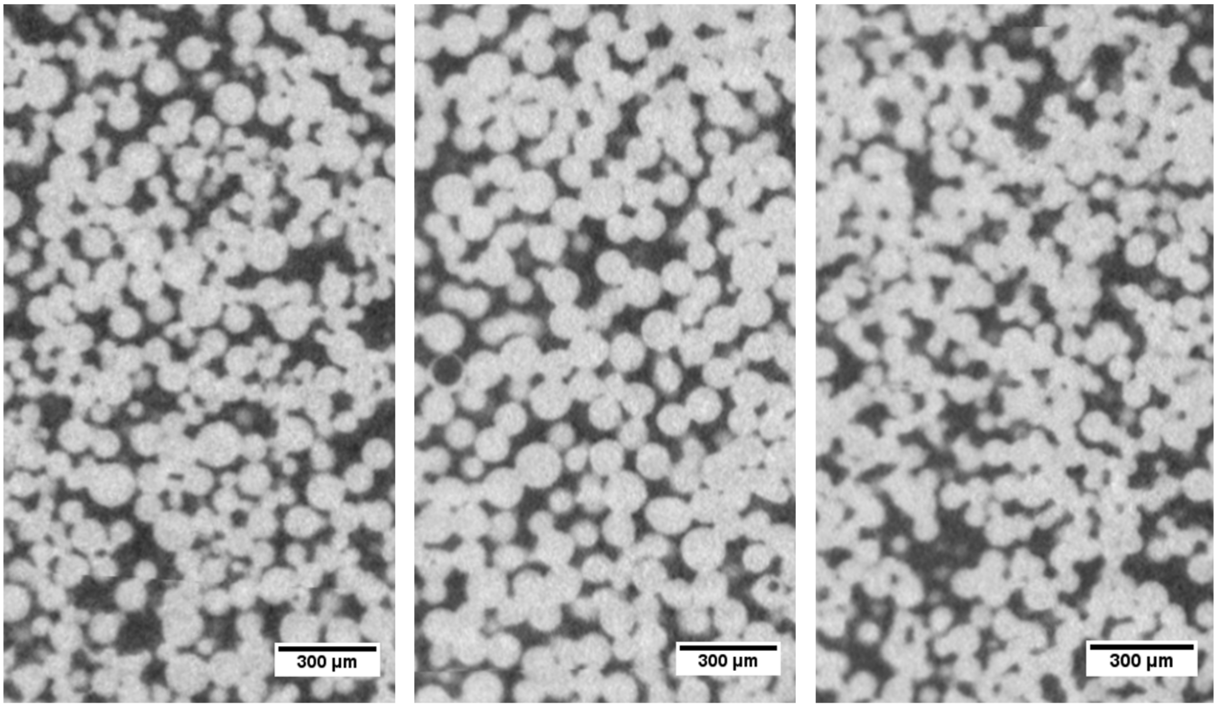

Figure 4.3: XZ plane cross-section images from reconstructed CT data of samples CT-AH (left), CT-BH (centre) and CT-CH (right) in the sintered state showing a qualitative view of the sample sinter necks between particles in the ROI

Even though all of the samples (CT-AH, CT-BH and CT-CH) had similar final densities,sample CT-CH shrunk considerably more than both CT-AH and CT-BH, having nearly double the amount of shrinkage. This substantial increase in densification is due to the higher driving force for sintering seen for particles with a smaller diameter. This demonstrates that using finer, but not necessarily ultra-fine, powder will still give tangible improvements in terms of densification. In addition, due to the finer particle size, the type C powder can give better surface finish and feature resolution compared to the type A and B powders. Generally, the use of the type C powder can be beneficial if trying to achieve near or fully dense parts, but potentially detrimental if trying to reduce shrinkage. To obtain any real benefit with the type C powder, the green density of the parts needs to be higher otherwise the sample will simply undergo more shrinkage to achieve a similar final density.

One unexpected aspect of the sinter results is that sample CT-BH shrunk significantly more than CT-AH, even though CT-BH had the largest particle size. One reason for this could be due to the difference in green density and therefore the number of contact points each particle had. From cross-sections of samples CT-AH and CT-BH in the green state, see Figure 4.4, it appears that CT-BH had a larger number of contact points compared to the more evenly spaced particles in CT-AH. As discussed earlier, a major driving force for sintering is the curvature of the particle system, which only exists if there are contact points. One would expect that since the part had higher levels of shrinkage while sintered at 1400℃, it would also see them at 1000℃, which is not the case. It could be that sample CT-BH was not able to take advantage of the larger driving force when sintered at 1000℃, but was when sintered at 1400℃. It should be noted that the difference in density could be due to the specific ROI that was sampled or variation in the samples themselves.

Samples CT-DH and CT-EH were sintered well past the 70% theoretical density threshold, with considerably more densification than the other samples. These results were generally expected due to the higher driving force seen in the finer particles. While the part as a whole did not technically entered into the final phase of sintering, localized areas within the samples did. This was confirmed with the image analysis of the parts, shown in Figure 4.7. Even without the image analysis, the localized density differences are large enough

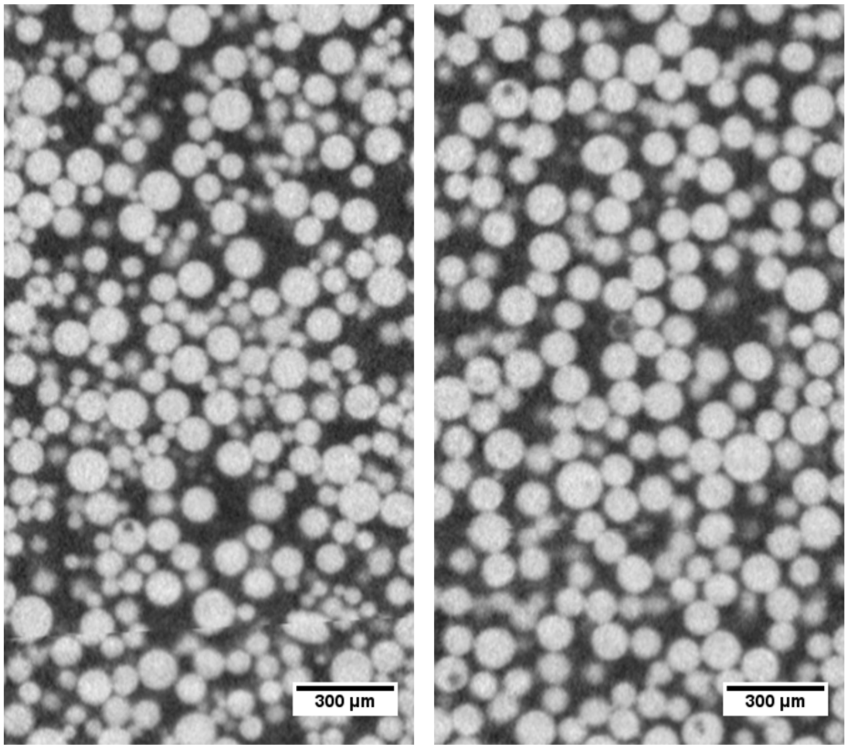

Figure 4.4: XZ plane cross-section images from reconstructed CT data of samples CT-AH (left) and CT-BH (right) in the green state showing a qualitative view of the sample contact points between particles in the ROI

that they can be seen visually in Figure 4.5 where areas that had high concentrations of the finer particles are now almost fully dense. Areas occupied by the larger particles still have more significant amounts of remaining porosity. In addition, the individual small particles in these regions are indistinguishable from each other. This indicates that the sinter necks are larger than the 1/2 particle diameter threshold, also indicating the final stage of sintering. The larger particles and their respective sinter necks are still distinguishable. The results from the CT analysis indicate that if the 0-45μm powder can be successfully printed on its own, it is likely that parts could be sintered into the 90% dense range. It is important to note that the high density that was achieved came at a cost of very large levels of shrinkage. While samples CT-DH and CT-EH achieved the highest final density, they also had the lowest green densities.

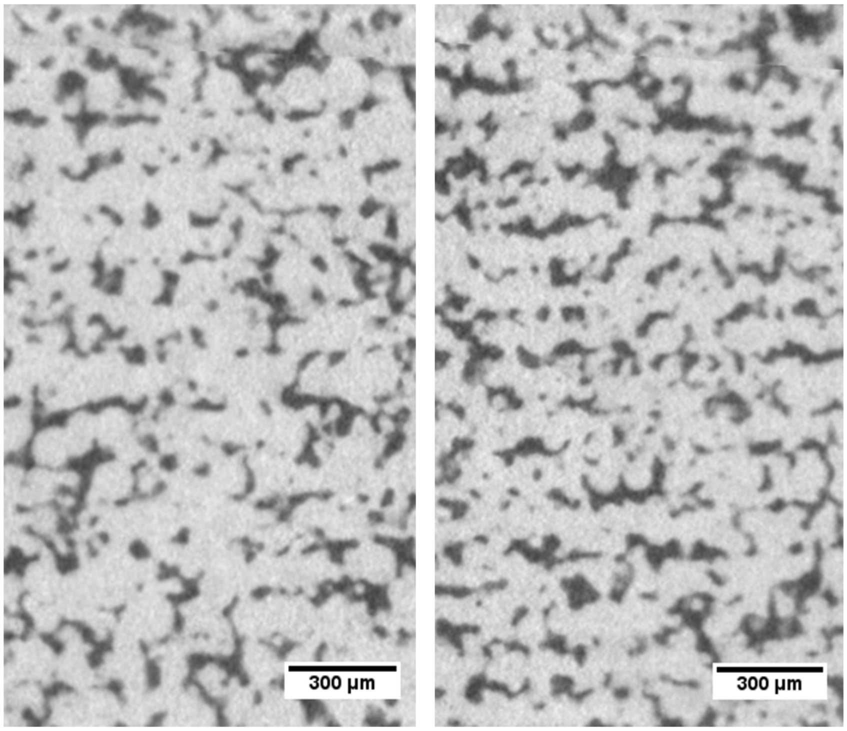

Figure 4.5: XZ plane cross-section images from reconstructed CT data of samples CT-DH (left) and CT-EH (right) in the sintered state showing a qualitative view of the sample sinter necks between particles in the ROI

The porosity of all parts was found as a bulk value but also with respect to height in the Z axis. All BJAM parts have fluctuating porosity in the build (Z axis) direction. The change in density is directly linked to the layers, and subsequently the layer thickness. Though powder spreading is consistent throughout the process, particle interactions between layers is different than within layers. Therefore, the density tends to fluctuate in a sinusoidal manner, with the highest density being the midpoint within a layer, and lowest at the midpoint between layers. This density fluctuation gives the parts some level of anisotropic properties, as both stiffness and strength are directly proportional to density. From the CT scan data all parts were found to generally follow this trend, but the samples had distinct enough results to be grouped into twos sets of parts. Parts from powder types A, B and C showed one general trend while those made with types D and E showed another. The main difference between the sample groups is the amplitude in the desnity profile as well as the change after sintering.

Figure 4.6 shows the density curves for both the green and sintered parts of the first group (powder types A, B and C). From Figure 4.6, it can be seen that the CT-BH sample density fluctuates around a mean density of 57.6% and 71.5% for the green and sintered part respectively. The amplitude of density change for CT-BH in both the green and sintered state is approximately +/- 8%. Both curves also show a spatial period of approximately 150μm, which is equivalent to the layer thickness. From the curves it can be seen that sintering does not fundamentally change the shape of the density profile, but rather changes the absolute values. This is due to the the part undergoing uniform densification during sintering, causing a uniform shift in density values. This effect is seen in samples sintered at both 1000℃ and 1400℃, with the samples sintered at a lower temperature simply seeing a smaller absolute density change. It is important to note that neither sintering method eliminated the fluctuation in density, and therefore parts, even though fully sintered, will still have anisotropic properties.

The second group of parts (powder types D and E), showed a somewhat different response during sintering. Figure 4.7 shows the density profiles of the second group. Sample CT-DL in its green state shows a larger amplitude change in density compared to the first group, but still shows a high-low density fluctuation with a spatial period of 150μm. The density profile of this sample is also not consistent, with a significant increase in the amplitude occurring from approximately 1mm to 1.5mm, before returning back to the

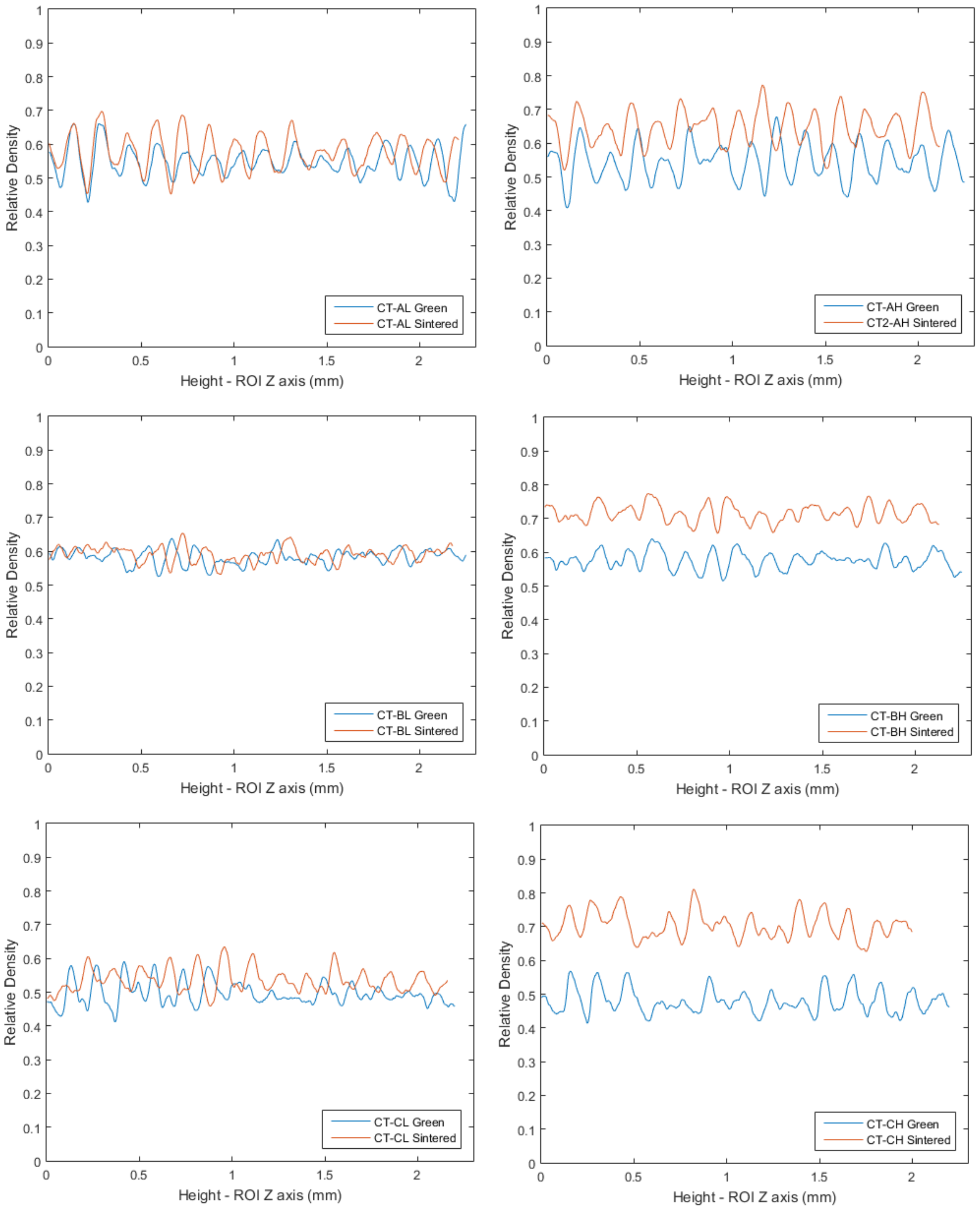

Figure 4.6: Density versus height of samples made from powder types A, B and C in the green and sintered state

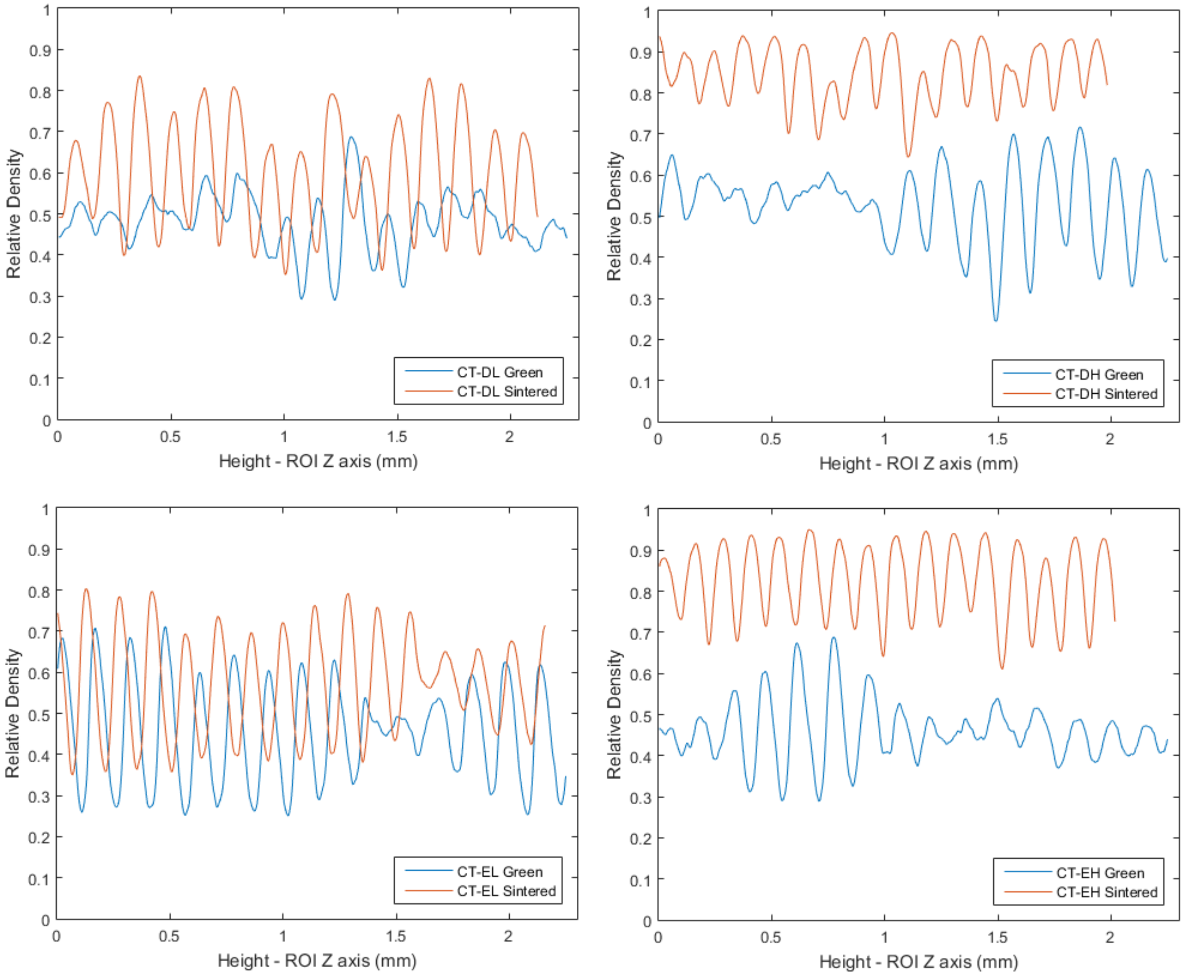

Figure 4.7: Density versus height of samples made from powder types D and E in the green and sintered state

original levels. From Figure 4.7 it can be seen that all of the samples in this second group show some level of significant increase in amplitude throughout the part, with sample CT-EL being almost entirely at this elevated state for the entirety of the ROI that was analyzed. Since the effect is localized, only occurring for a few layers for most of the samples in this group, it is likely due to inconsistencies in the printing process, either from powder not spreading consistently, or the powder not being uniform throughout the print. This is likely due to the inclusion of the very fine particles in these bi-modal powder blends.

The very fine particles tend to have poorer spreadability and could therefore contribute to inconsistent spreading, which would impact the density profile. A localized non-uniformity in the powder blend is also more likely with these powder types since a significant difference in particles sizes makes it easier for bi-modal powder blends to separate. A localized separation of the large and fine particles, could be caused either by insufficient or over mixing during blending. It could also be caused during addition of powder in the BJAM system. As discussed earlier, powder is poured into the system, leveled and then compacted slightly. These actions are fairly vigorous, and could also cause a localized separation of powder, affecting the density profile.

The other defining feature of the second group of samples is the change in density profiles after sintering. The samples still show an upward shift in the mean density (going from 48.1% to 60.3% dense for CT-DL), but also show an associated increase in the amplitude of the density profile. In the green state, sample CT-DL had a density change of approximately +/- 10% while in the sintered state it had a density change of +/- 21%. This density profile change is seen in all of the samples in the second group with the exception of the CT-EL sample, where the density profile remains unchanged. It should be noted though that in the green state (and subsequently the sintered state) CT-EL had a density profile similar to the sintered profile of the other samples in the group. Figure 4.8, shows CT-DL in both a green and sintered state, with the large particles aligned horizontally along the X axis, indicating the part layers. The part appears relatively homogeneous in terms of density in the greens state, but in the sintered state it is clearly visible that the printed layers densified significantly more than the regions between them. A potential cause for this difference in densification (and therefore the change in the density profile) is due the presence of the finer particles and the difference in the number of contact points within a layer compared to between layers. With more contact points within a layer, densification should preferentially occur there, pulling the particles in towards the center of the printed layers. This would then prevent effective sintering between layers as a result. This effect is likely only significant with the powder types with finer particles due to the significantly higher amounts of shrinkage associated with those particle sizes.

4.1.2 Particle Size

While particle size cannot be used to directly identify specific part properties, it is indicative as to the degree of sintering that occurred within the parts. If a part is sintered at low temperatures, and minimal densification and neck formation occurs, then there should also be a minimal change in detected particle size. If sintered at high temperatures, there should be a larger change in measured particle size as necks grow and particles converge together. The mean particle sizes measured using CT for the parts in both the green and sintered state are summarized in Table 4.2. Histogram plots for the particle sizes distributions are shown in Figures 4.9 and 4.10.

Similar to the results seen for porosity, the parts can be grouped based on the sintering temperature and whether fine particles were added into the powder mixture. The parts with only larger particles and sintered at 1000℃ (CT-AL, CT-BL and CT-CL) had effectively no

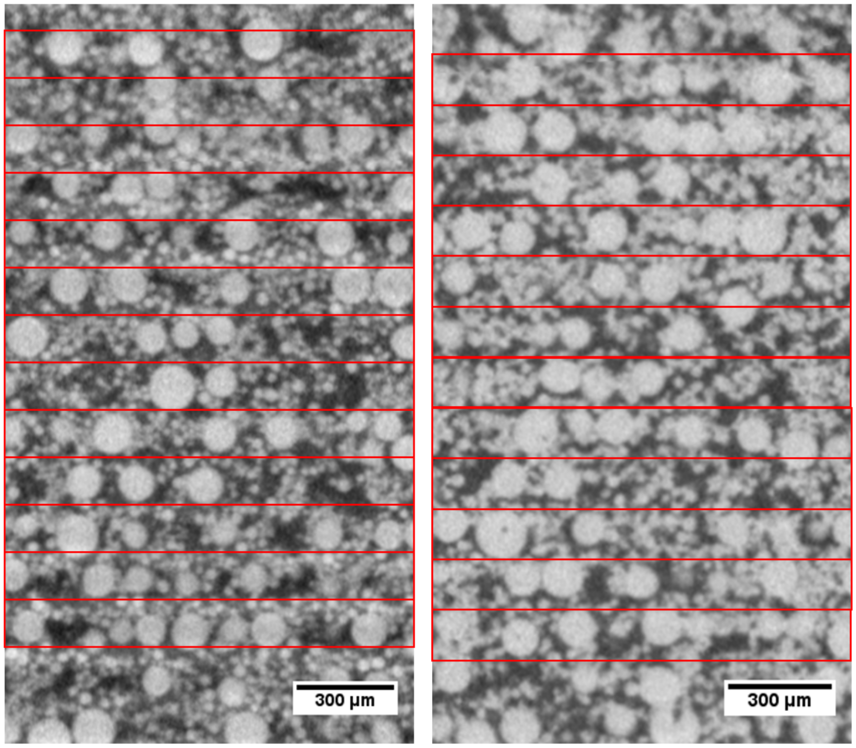

Figure 4.8: XZ plane cross-section comparison of sample CT-DL in the green (left) and sintered (right) state showing the horizontal alignment of larger particles, highlighted by the red boxes, in the ROI from the printing process

change in mean particle size, as was expected. This was due to the limited neck formation and minimal densification. Parts with the same powder types but sintered at 1400℃ (CT-AH, CT-BH and CT-CH) had a more significant change in mean particle size, due to the more significant neck formation seen in these parts. The parts with smaller particles had a more significant increase in particle size compared to those comprised of only larger particles. Even the samples sintered at 1000℃ (CT-DL and CT-EL), though showing a smaller absolute increase, were found to have a larger proportional increase. This is due to the proportionally larger sinter necks seen with the smaller particles even when sintered at the lower temperatures. Parts with the smaller particles and sintered at 1400℃ (CT-DH

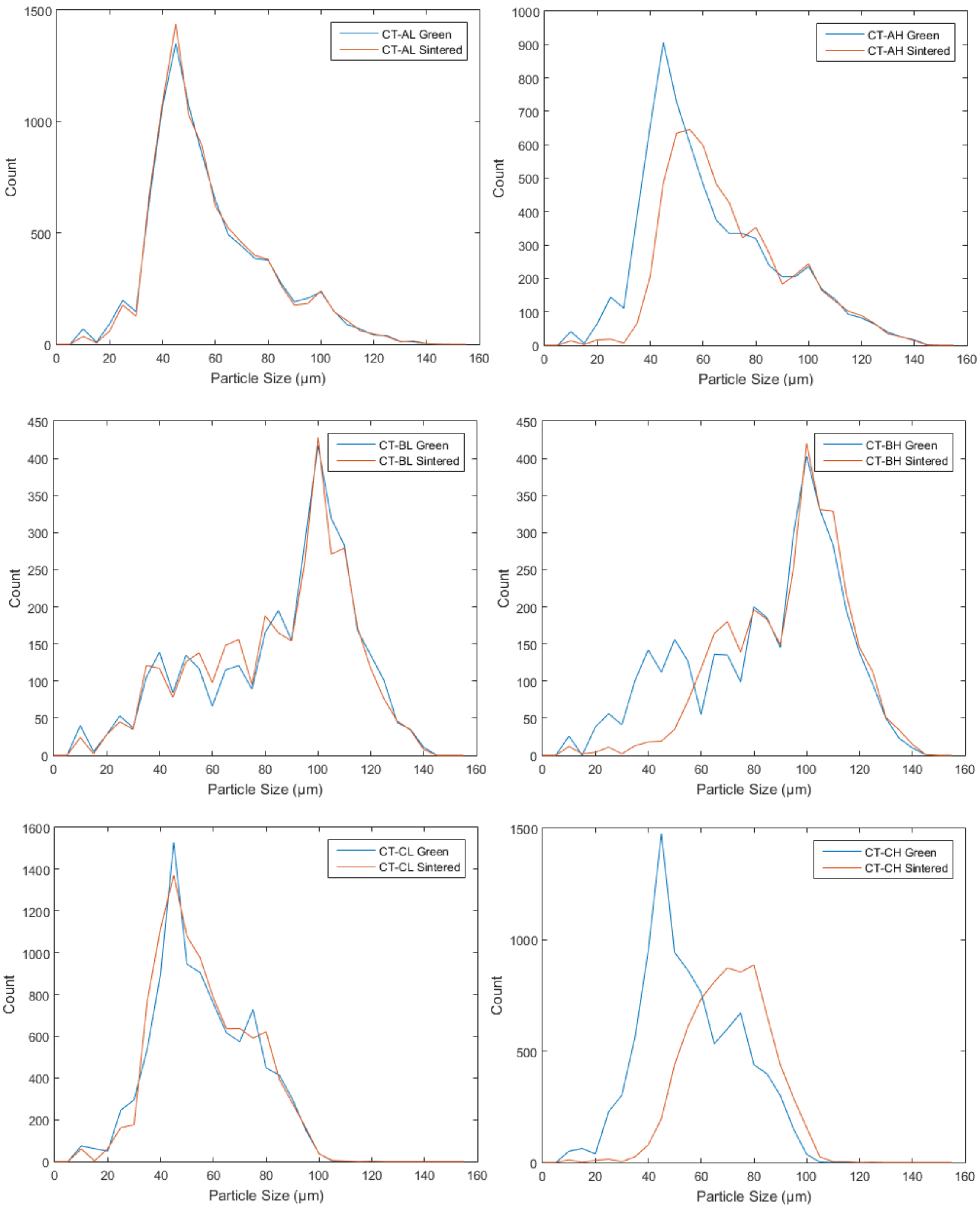

Figure 4.9: Histogram comparison of the particle size distribution of samples made from powder types A, B and C in the green and sintered state

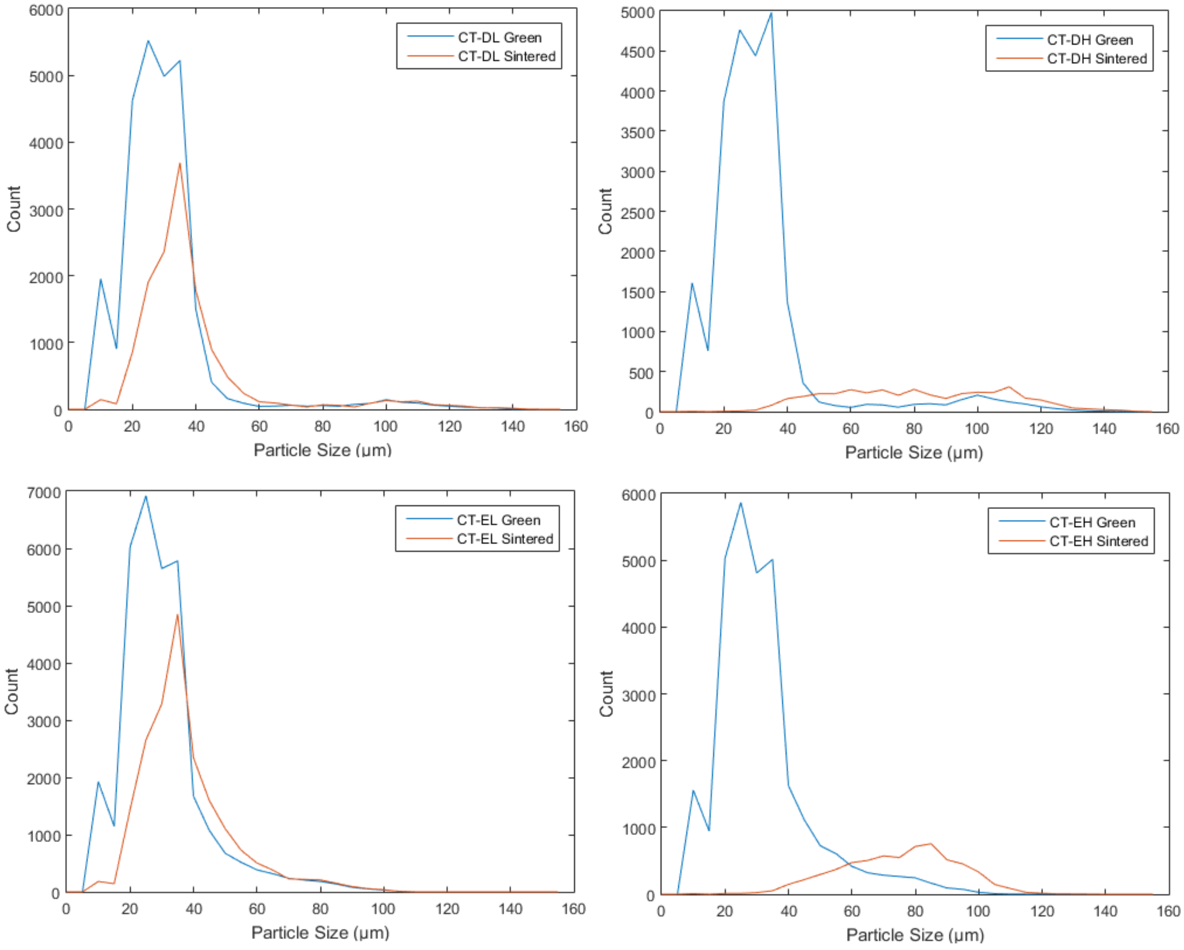

Figure 4.10: Histogram comparison of the particle size distribution of samples made from powder types D and E in the green and sintered state

Table 4.2: Summary of sample mean particle sizes in the green and sintered state

	Mean Particle Size (μm)		
Sample Name	Green	Sintered	Change
CT-AL	55.4	55.6	0.2
CT-AH	60.4	67.5	7.1
CT-BL	82.7	81.8	-0.9
CT-BH	82.1	90.8	8.7
CT-CL	54.7	53.8	-0.9
CT-CH	54.5	68.3	13.8
CT-DL	27.0	31.2	4.2
CT-DH	28.8	78.9	50.1
CT-EL	27.5	35.3	7.8
CT-EH	28.9	72.4	43.5

and CT-EH) have a particularly larger change in mean particle size, with the value nearly doubling for both parts. The substantial change is likely due to the small particles entering the final stage of sintering and those localized areas becoming nearly fully dense. With the smaller individual particles becoming indistinguishable, they would be measured as larger particles, contributing to an increase in the mean particle size.

4.1.3 Pore Size

The mean pore size results of the samples in both the green and sintered state are summarized in table 4.3, with histogram plots shown in Figures 4.11 and 4.12. Similar to the other features examined in the parts, the samples can be split into two groups. Samples made from powders type A, B and C all show a single mode distribution of pore size, with a peak around 40μm, as can be seen in Figure 4.11. Within the first group, the different powder distributions appear to have little effect on the pore size and distribution. Samples sintered at 1000℃ had effectively no change in pore size after sintering, which was due to the limited neck formation. The parts also show a limited change in the number of pores as well. Since these parts predominantly remained in the initial sintering stage, neck sizes are comparatively small and particles have not yet shifted, meaning the pore sizes would not be affected significantly. Samples sintered at 1400℃ had a larger decrease in pore size and pore count, though the change is still relatively small.

Samples made with powder types D and E, show a bimodal distribution with peaks around 10μm and 40μm for all of the samples in the group, as can be seen in Figure 4.12. It should be noted that due to the voxel size used during scanning, only pores with a diameter of 10μm or larger can be reliably detected. Therefore, the counts of pores less than 10μm could potentially be inaccurate. Samples in the second group sintered at 1400℃ (CT-DH and CT-EH) show a significant change in the pore distribution, with a significant portion of the larger pores being lost. While all of the other samples (excluding CT-DH and CT-EH) show some decrease in the number of pores, the distribution profiles stayed effectively the same, only being shifted slightly left and down towards less and smaller pores. Samples CT-DH and CT-EH do however show a substantial change in the distribution profile. This is likely due to the more significant levels of shrinkage seen with these parts compared to the other samples. The small change in pore size seen in the other samples (excluding CT-DH and CT-EH) is likely due to the fact that none of the parts entered into the final stage of sintering. Pore elimination, and therefore a substantial change in pore size, only occurs in the final stage of sintering [73]. The parts as a whole remained within the intermediate stage of sintering meaning only the general pore network structure was altered. As discussed in Chapter 2.3, the pore network is still interconnected, but becomes more tubular during the intermediate stage as sinter necks grow. While this does change the general structure, it had a minimal effect on the actual pore diameters [54]. For a more substantial change in pore size to be seen, parts would have to progress further into the final stage of sintering where pores are isolated and eliminated.

Table 4.3: Summary of sample mean pore sizes in the green and sintered state

	Mean Pore size (μm)		
Sample Name	Green	Sintered	Change
CT-AL	38.8	37.8	-1.0
CT-AH	42.6	40.0	-2.6
CT-BL	45.4	44.2	-1.2
CT-BH	46.0	37.6	-8.4
CT-CL	40.5	38.3	-2.2
CT-CH	42.6	36.5	-6.1
CT-DH	29.7	24.6	-5.1
CT-DL	31.7	29.1	-2.6
CT-EL	30.1	27.8	-2.3
CT-EH	31.4	25.2	-6.2

4.1.4 Overall Considerations

The results from the CT analysis highlight a number of features of powder blends that should be considered for BJAM. From the results, it can be seen that though the finer particles can give very high levels of densification, it does not necessarily guarantee higher densities. This is attributable to the larger frictional and electrostatic forces seen with finer particles. This requires them to have more compaction forces to achieve similar green densities seen with powder blends made of large particles. While higher compaction forces can be achieved, it could require significant adjust of printing parameters or modification of a printer. Without improving the green density for parts made with the smaller particles, sintered parts will have the same final density but with significantly more shrinkage.

The shrinkage of parts is also another reason why the addition of smaller particles should be considered carefully. High levels of shrinkage is difficult to compensate for, especially if

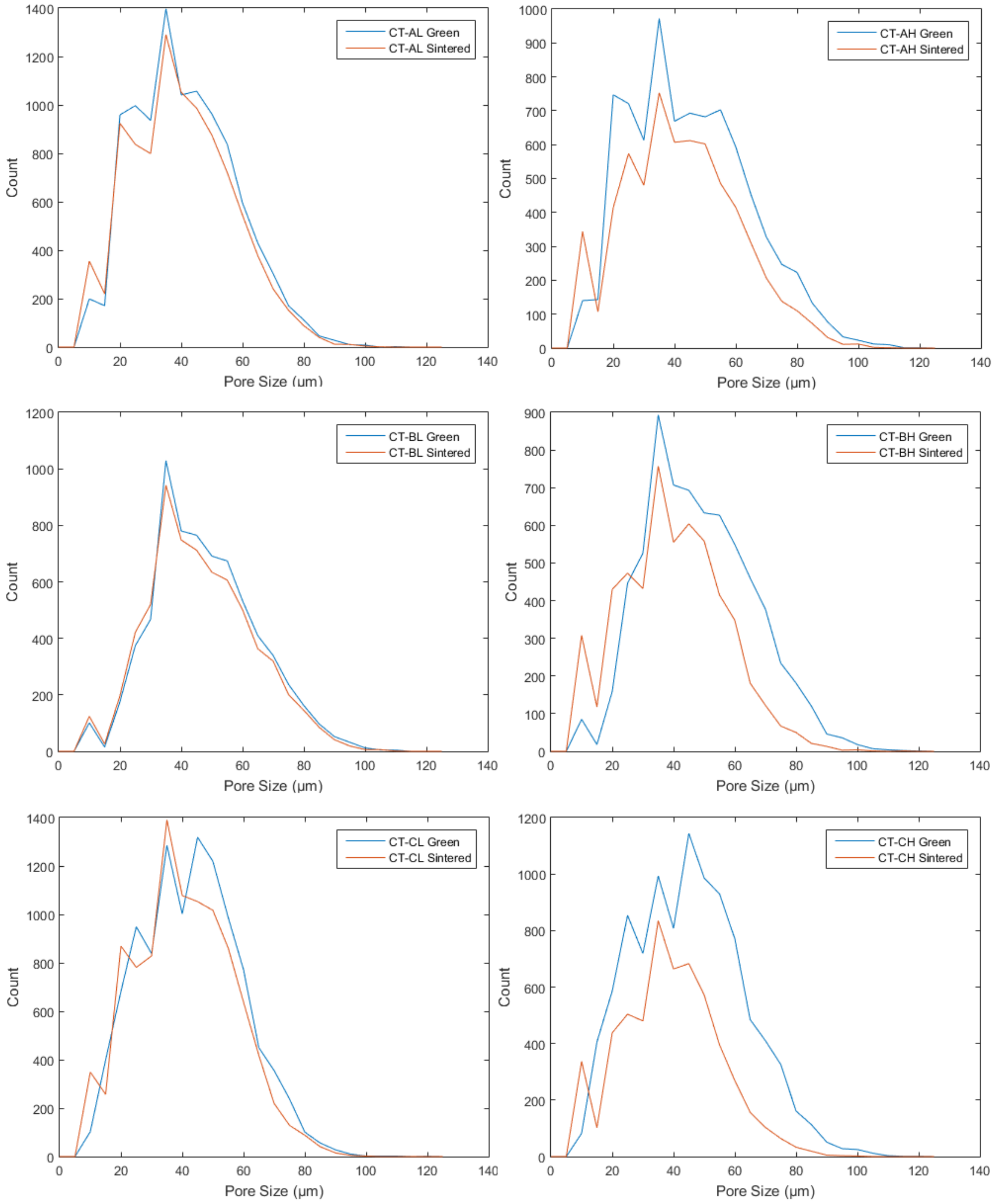

Figure 4.11: Pore distribution of samples made from powder types A, B and C in both the green and sintered state

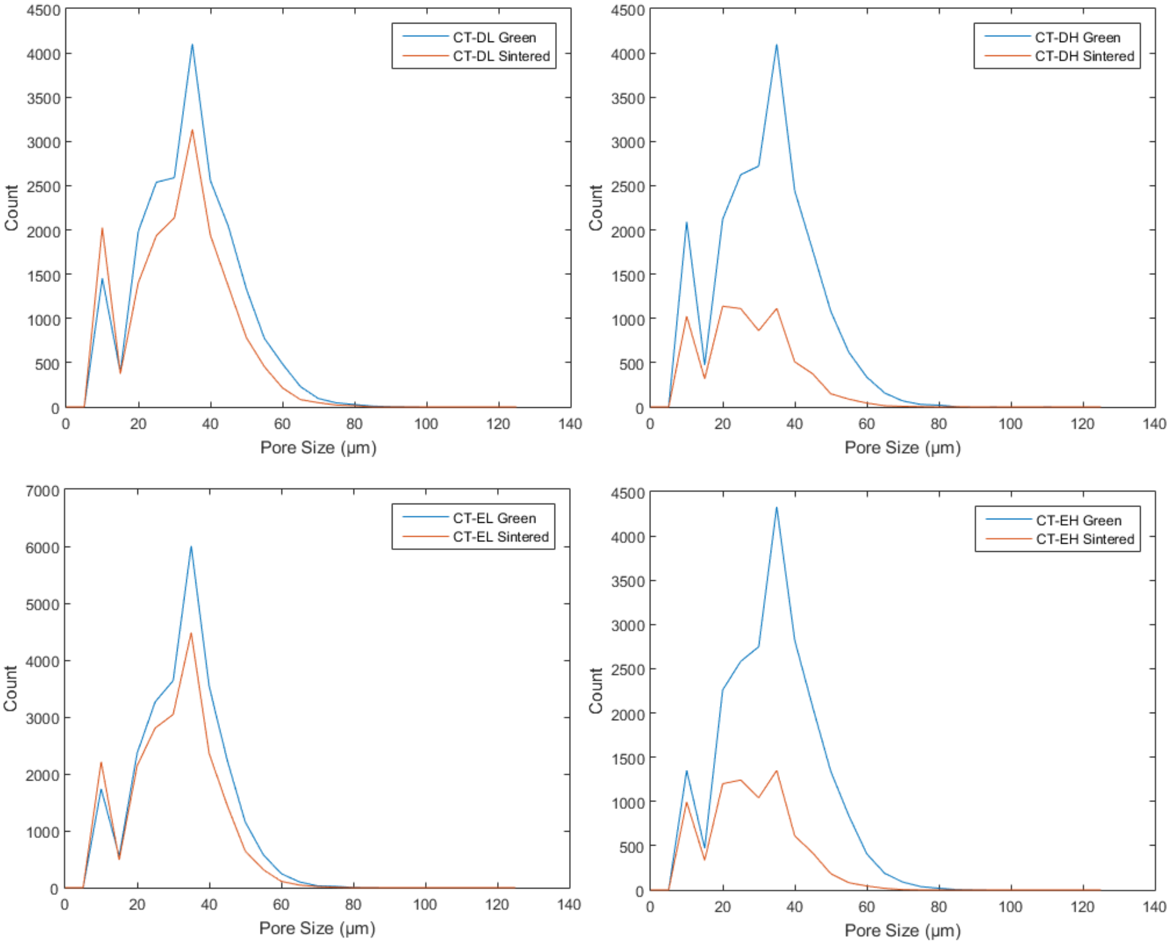

Figure 4.12: Pore distribution of samples made from powder types D and E in both the green and sintered state

the part has very small features. Orthopedic implants tend to be relatively large and simple in shape, meaning the detrimental effects will be somewhat limited. Dental restorations on the other hand, tend to have smaller features to properly mimic teeth and to allow for mounting to implants in the jaw. Dental restorations, especially full-jaw restorations, are long, thin and curved, making distortion from shrinkage very significant. High levels of shrinkage also make it difficult to control the exact position and orientation of mounting features that should perfectly match the positions of implants in a patient.

The final consideration for the addition of small particles is the level of anisotropic properties in the printed parts. From the results, samples made with the smaller particles had significantly larger density differences between the inter- and intra-layer regions. Though the parts had a nominal density of around 80%, intra-layer regions had densities around 95% while inter-layer regions had densities around 55%. Such a large difference in density makes it particularly difficult to predict and control part strength for complex geometries.

While the addition of smaller particles was able to improve sintered density, it caused the parts to undergo substantially higher levels of shrinkage. Therefore, to take full advantage of the finer particles, more consideration should be given to powder compaction during printing to achieve higher green part densities.

4.2 Master Sinter Curve

The analysis for the development of the MSCs began with the collected dilatometry data. This data then underwent a number of steps to be able to create the MSC. First, the data was corrected to compensate for thermal expansion and the shrinkage data was then converted into relative density. Next, the apparent activation energy (represented by Q) for the powder type was found. This involved plotting the part density versus the MSP, along with a fitting curve, for a number of different Q values. From these, an error value was calculated, and the Q value that gives the lowest error was selected. The plot of density versus the MSP for that specific Q value was then used as the MSC.

4.2.1 Dilatometry Data

The data that comes from the dilatometer is a table of time, temperature and dimensional change. While both the time and temperature values are accurate, the shrinkage data needs to be corrected to compensate for thermal expansion. All of the samples showed the expected linear slope during cool down, which was used to generate the CTE for each part. The method for calculating CTE is the same for all samples, as discussed in Section 3.4. The CTE results for each sample are listed in Table 4.4. Due to measurement issues, CTE values could not be obtained for samples DIL-E3 and DIL-E1 during the dilatometry measurements. An average value of 10.90 $10^{-6}k^{-1}$ was used instead. All of the measured values are similar each other as well as those found both in literature [103], and from the earlier dilatometry tests. With the CTE values found for all of the samples, the raw dilatometry data was corrected and then converted into plots of temperature versus relative density, using the methods discussed in earlier. Similar to the initial test samples, the green densities used are taken from the CT results. For creation of the MSCs, the two samples were assumed to have the same green density, which is necessary to conform with the MSC assumptions. Plots of the parts during sintering are shown below for relative density versus temperature with the data truncated from 1050k to the peak of approximately 1823k. This was done since a negligible amount of sintering occurred below this temperature and the data needed to be truncated below that temperature for further processing to create the

MSCs.

Table 4.4: Summary of dilatometry sample CTEs

	CTE ($10^{-6}k^{-1}$)	
Powder Type	1 (℃/min)	3 (℃/min)
A	11.97	10.44
B	11.50	11.47
C	10.11	9.50
D	11.44	9.45
E	10.90	10.90

The raw data gathered from the dilatometer is, unfortunately, not usable for creating the series of MSCs. As discussed earlier, other groups have had difficulties obtaining good quality results from a push rod dilatometer with highly porous samples. Some of the issues seen with the results is also likely due to the use of the sapphire crucible during sintering. Only samples DIL-B3 and DIL-B1 (see Figure 4.19) show the expected densification profiles, where the sample sintered at 1℃/min rate shows a higher density than the sample sintered at 3℃/min. Samples DIL-A3 and DIL-A1 (see Figure 4.18) show profiles that are somewhat similar to the expected, and even though the sample sintered at 1℃/min shows lower densities at some points, it still ends with a significantly higher density. The results from DIL-C1 and DIL-E1 (see Figures 4.15 and 4.17 respectively) are clearly not representative of the sintering process as shrinkage nearly plateaus over the entire sintering run but then suddenly jumps near the end. This profile is likely the result of the crucible plug getting caught on loose powder or getting jammed during travel. This would have stopped or slowed the plug, causing the plateau seen in the density. As the sintering run neared its end, the sapphire crucible would have expanded, allowing the plug to more freely travel and causing the spike in density. Regardless of the cause of the profile, due to the abnormal shape it cannot be used to create a MSC. Sample DIL-D1 (see Figure

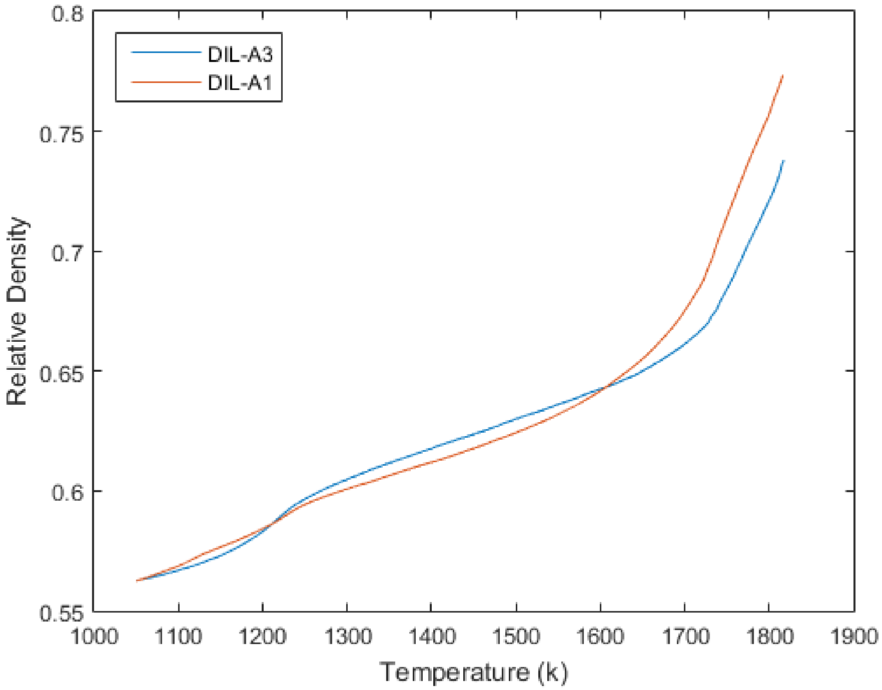

Figure 4.13: Dilatometry results for the type A powder parts

4.16) shows a particularly odd profile in that the sample sintered at 1℃/min is always at a lower density compared to the sample sintered at 3℃/min. In addition, the sinter profile is irregular with some sharp transitions and a non-uniform densification rate. This profile is also likely due to issues with the crucible and plug sintering method required to prevent oxidation.

Though the results appear to not be usable, unlike with the previous preliminary dilatometry runs at 5℃/min and 10℃/min, the samples run at 1℃/min show no excessive shrinkage. This indicates that the samples were strong enough to withstand the forces from the push rod and are not being excessively compacted. In general, though the densification plots are abnormal, the final densities seen with the samples follow the same

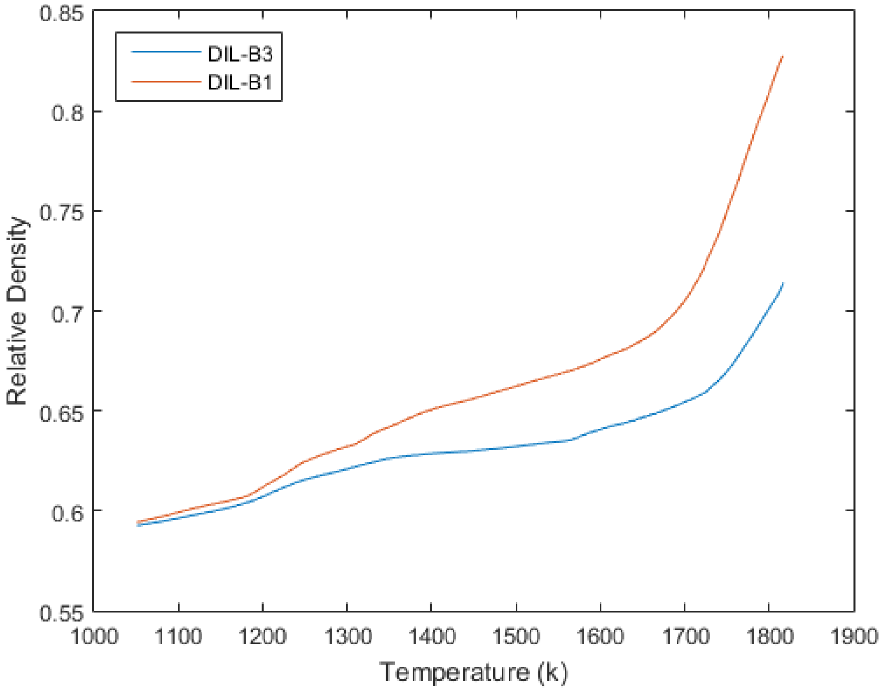

Figure 4.14: Dilatometry results for the type B powder parts

general trends seen from the sinter structure analysis. The powder types with the addition of finer particles start at a lower green density but see much higher rates of densification compared to the other powder blends. This matches what was seen with the CT results, where powder types D and E showed significantly higher levels of densification. The type B powder also shows a higher level of densification compared to the type A, also matching what was seen with the CT results.

Even though the dilatometry results for the samples made with the C, D and E powder types are abnormal, the data was still processed to try and find Q. First, the data is truncated from 777℃ (1050K) to 1550℃ (1823K). Even though sintering can be assumed to start above 880℃ for titanium, it is beneficial to keep a portion of the data just below

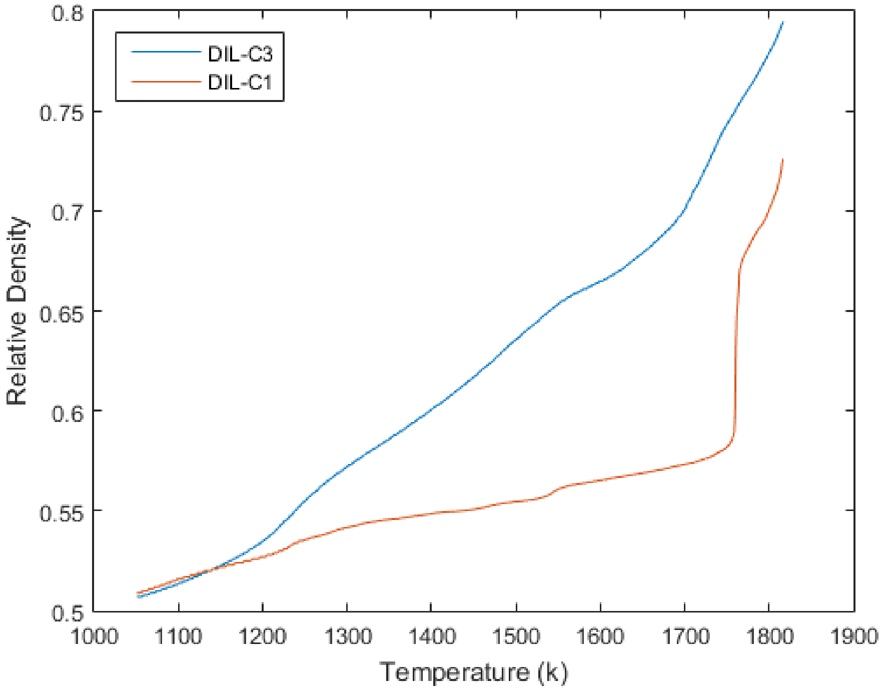

Figure 4.15: Dilatometry results for the type C powder parts

this point to ensure there is enough data for good curve fitting. In addition, the time values for sintering are zeroed at the beginning of the truncated data set. Similar to temperature, time spent at lower temperatures does not contribute to sintering. The data set needs to be truncated and the time values zeroed otherwise the calculated MSP values would be inaccurate.

4.2.2 Apparent Activation Energy

As discussed in Section 3.4, Q is found by comparing various calculated data sets (from the measured dilatometry data) to a fitted curve. The Q value with the lowest error is the most correct and used for the generation of the final MSC. The dilatometry data was

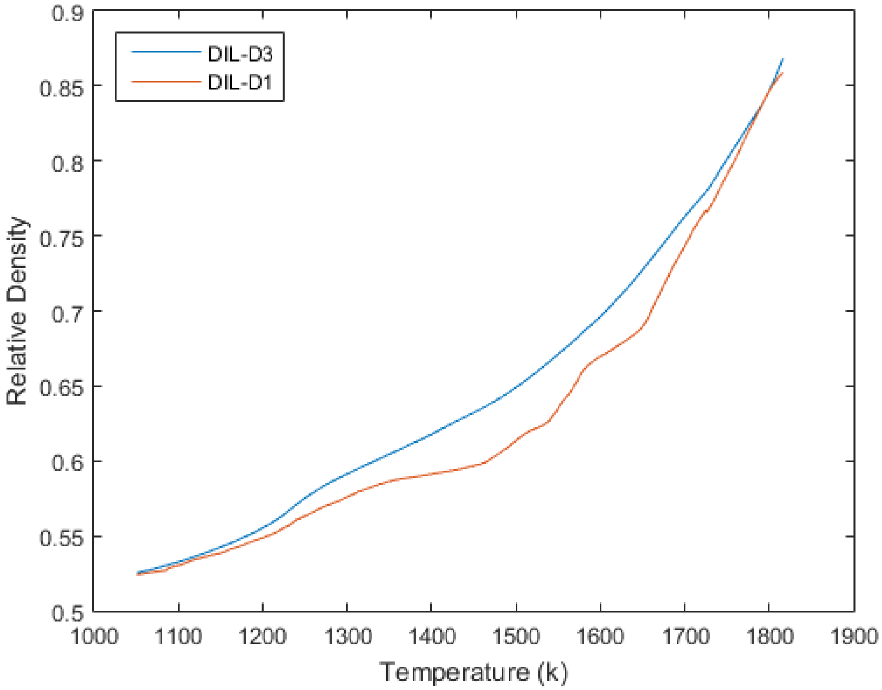

Figure 4.16: Dilatometry results for the type D powder parts

imported and processed in Matlab, and the exact code is shown in Appendix C. MSCs are generated for Q values ranging from 20kJ to 600kJ, in increments of 5kJ. The fitted curve has the same form as discussed in Chapter 2.4.2, except the fit parameters are calculated through the Matlab Curve Fitting Tool using a non-linear least squares method, rather than using the Newton-Raphson method. The root mean square error (RMSE) is also calculated directly using the Matlab Curve Fitting Tool. The plots of Q versus RMSE are shown below for powder types A and B, which were the only sample sets that provided usable dilatometry data.

From the plots of Q versus RMSE, only the samples made with the type B powder (see Figure 4.19) show the expected profile, with an obvious and well defined minimum

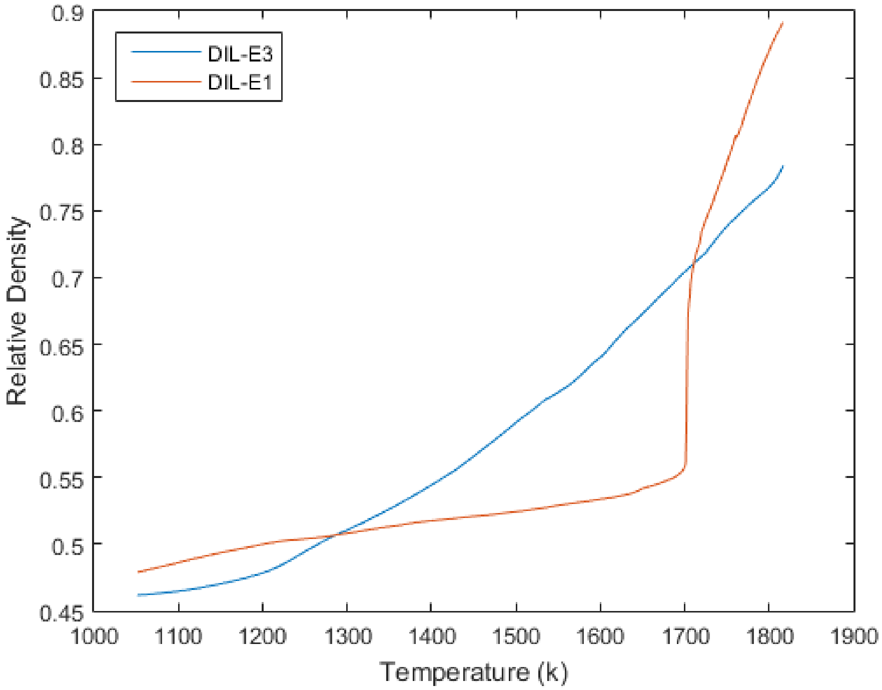

Figure 4.17: Dilatometry results for the type E powder parts

RMSE value. From the plot, an (approximate) Q value of 95kJ is found. While it is on the low end, it is within the range other groups have found when making MSCs for titanium powder [85, 86, 10]. The samples made with the type A powder do have a local minimum at (approximately) 245kJ. However, the minimum is not obvious and the Q value is significantly higher than either the type B powder or other values found in literature. This abnormal value is due to the abnormal dilatometry results where the density values for the 1℃/min and 3℃/min sample runs overlap and cross over each other. This could easily cause the lowest RMSE to be found at an incorrect value since the two densification plots would not properly align over top of each other when cycling through the various Q values. Plots for powder types C, D and E could not be used to find Q. The profiles show

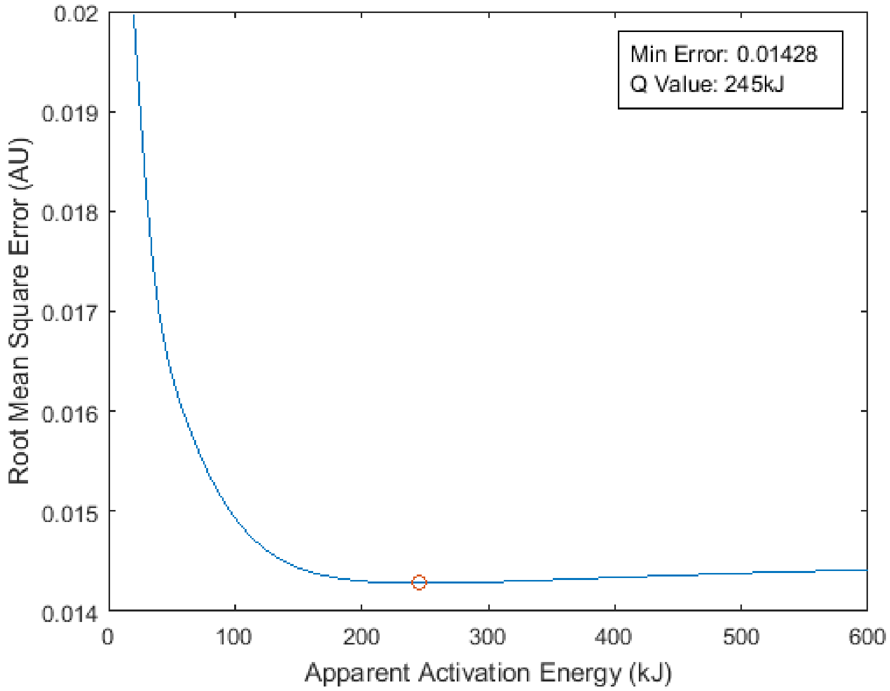

Figure 4.18: Activation energy versus RMSE for the type A powder parts

a higher error over the expected Q value range with the RMSE gradually decreasing as the Q values get larger. These plots do not follow the expected trend, and do not show a local minimum and therefore cannot be used to find Q values for the samples. The plots are shown in Appendix E.

4.2.3 Master Sinter Curves

MSCs were created for both the type A and type B powder samples. Even though the type A powder sample was found to have an abnormal Q value, a MSC was still made regardless. The MSCs for the type A and type B powder samples are shown in Figures 4.20 and 4.21 respectively. In both plots the blue dotted lines represent the measured data

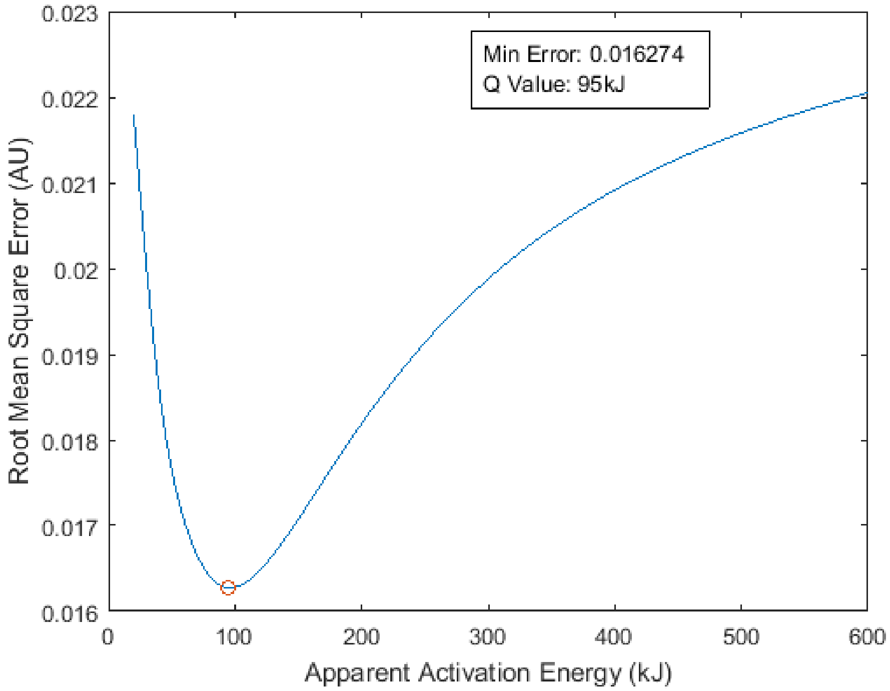

Figure 4.19: Activation energy versus RMSE for the type B powder parts

while the red fitted line represents the actual MSC.

Neither plot shows what would be considered an ideal MSC, where all of the data as well as the fitted curve fully align to make effectively a single, overlapping curve. One major issue with both of the plotted MSCs is that the data does not show the upper asymptote that would define the upper limit of relative density. An approximation of 0.90 was used to be able to generate curves for both of the powder types. The final density values found after sintering for the CT analysis were not used since the final measured density values from the dilatometer were higher. This upper asymptote is critical for generating the proper shape for the sigmoidal fitting curve. The lack of this feature in the dilatometry data indicates that the samples were not sintered to their full density. This could be remediated

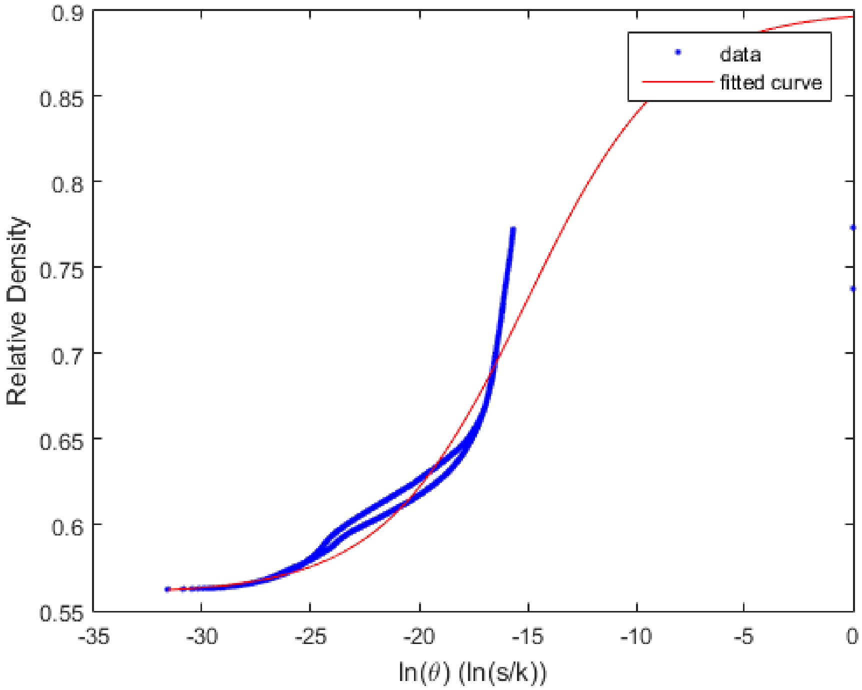

Figure 4.20: MSC for the type A powder parts plotted using a Q value of 245kJ

by simply extending the sintering time at the peak temperature of 1550℃ to ensure the sample is sintered to its maximum density. Another issue that can be seen with the fitted curves is that while the fit is reasonable at lower $\ln(\theta)$ values, as they increase, the fit gets progressively worse. The sigmoidal curve has a significantly lower slope compared to the plotted data at larger $\ln(\theta)$ values. The poor fit at the end of the curve is also likely due to the approximated upper asymptote that was used for fitting. However, the main factor is the abnormal dilatometry curves in general, which makes it difficult to have a good fit.

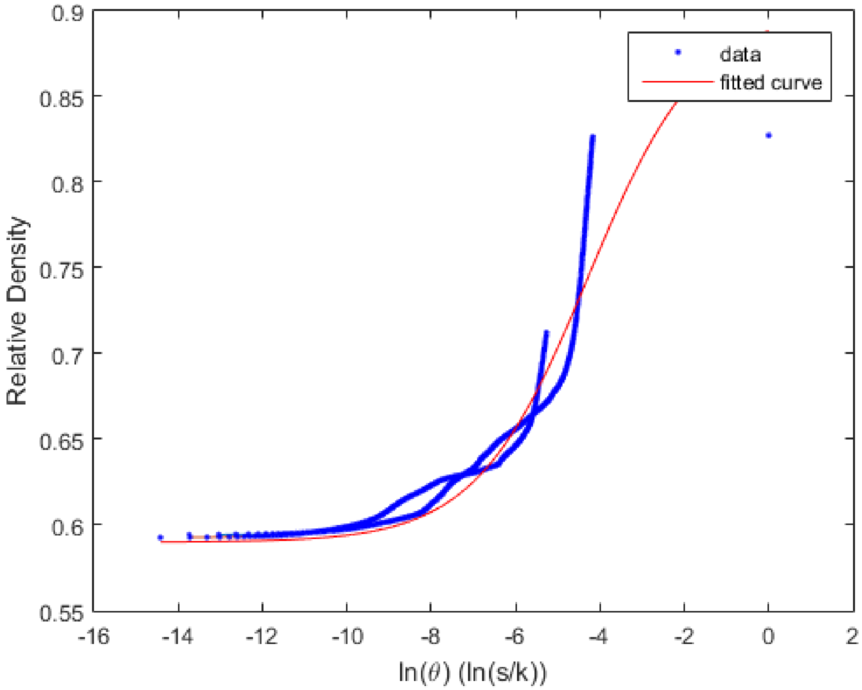

Figure 4.21: MSC for the type B powder parts plotted using a Q value of 95kJ

4.2.4 Master Sinter Surface Creation

Due to the data being unusable to create MSCs for most of the powder types, no MSSs could be created. Ideally, if all of the MSCs had been usable, a third axis could have been generated to create a surface.

Chapter 5

Conclusions and Future Work

5.1 Conclusions

5.1.1 Sinter Structure Analysis

The first conclusion that can be made as part of the sinter structure analysis is that CT is a viable and useful technique for measuring the properties of BJAM parts. The results from the CT analysis showed both bulk properties as well as properties on a per-layer basis. The CT analysis also allowed for these properties to be found for the same sample in both the green and sintered state. While there was a limitation on measuring sinter necks and pores below 50μm and 10μm respectively, the method was able to provide substantially more information compared to other analysis techniques.

The second conclusion that can be made is that the addition of finer particles improves the bulk density of sintered parts, but at the cost of higher levels of shrinkage. The addition of fines decreases green part density, but the higher driving force for sintering compensates for this, allowing the parts to achieve fairly high density levels, around 85%. The large amount of shrinkage seen with these parts, on the order of 40%, would make it difficult to create compensation values for small, complex features.

The third conclusion that can be made is that the BJAM parts have high levels of density change between intra- and inter-layer regions. Parts made with the larger powder blends (types A, B and C) showed the least amount of density variation, with the density changing approximately +/- 5% around the mean. Parts made with the fine powder blends (types D and E) show very high levels of density fluctuations between the inter and intra-layer regions, with density fluctuating approximately +/- 20% around the mean. This high level of fluctuation in density means that though parts with the finer particles have a higher bulk density, they have higher levels of anisotropy.

The fourth conclusion that can be made from the sinter structure analysis is that near full density parts could be obtained if only the fine powder is used. Areas of parts composed predominantly of finer particles and sintered at 1400℃ were nearly fully dense after sintering.

5.1.2 Master Sinter Curve

Unfortunately, due to the poor results obtained from the dilatometry measurements, and subsequently the MSCs, there are few conclusions that can be drawn as to the effectiveness of the MSC for predicting the properties of BJAM parts. The main conclusions that can be made are about the dilatometry measurements themselves.

First, titanium BJAM samples require a gas-sealed dilatometer to obtain reliable shrinkage results. The oxidation levels from the non-sealed dilatometer were unacceptably high. The sapphire crucible used did prevent oxidation, but tended to get caught or stuck during sintering, giving unreliable results.

Second, BJAM parts are very susceptible to compaction from applied forces during sintering. To be able to obtain good dilatometry results, very low or no forces should be applied to samples.

Third, while the MSC curve concept appears to be a very powerful tool for predicting density, and subsequently other properties, the technique is highly dependent on the quality of the empirical data it is made from. The two MSCs produced during this work showed somewhat good correlation at lower Θ values, indicating that the technique has promise. However, the poor correlation at higher values makes the overall MSC results unreliable.

5.2 Future Work

5.2.1 Sinter Structure Analysis

The one major aspect of the sinter structure analysis that requires further work is for the creation of a more optimized powder blend. Powder blends with equal portions (by weight) of the larger and finer particles were used simply to see the effects of powders during sintering, rather than trying to achieve a specific density, or densification value. However, now that there is a better understanding as to the effects the different powder sizes have, more work can be focused on tailoring a blend to achieve specific properties.

5.2.2 Master Sinter Curve

The general process for creating the MSCs has already been developed as part of this work, meaning that only reruns of the dilatometry measurements need to be done in order to create new curves. With the issues seen both from the crucible and the push-rod itself, parts should ideally be measured in an optical dilatometer. The optical dilatometer has the benefit of taking non-contact measurements, eliminating part compaction as a source of error. If the system is also gas-sealed, issues surrounding oxidation are also remediated

Another part of future work that should be done is a thorough validation of the developed MSCs. Validation of the curves was not done due to the uncertainties and potential unreliability surrounding the results. Validation should be completed once MSCs of sufficiently good quality have been developed.

One other important aspect of future work is linking part densities to specific part properties. This needs to be done to expand the usefulness of the curves beyond simply predicting density.

The final aspect of future work for the MSCs is the formulation of a MSS that could also potentially expand the usefulness of the developed MSCs.

References

[1] C. Lindemann, U. Jahnke, M. Moi, and R. Koch, "Analyzing product lifecycle costs for a better understanding of cost drivers in additive manufacturing," *Solid Freeform Fabrication Symposium*, vol. 23, pp. 177–188, 2012.

[2] T. Douglas and S. Gilvert, "Costs and Cost Effectiveness of Additive Manufacturing," *NIST Special Publication*, no. 1176, 2014.

[3] U. S. Patent, S. Haggerty, J. Michael, and P. A. Williams, "Three-Dimensional Printing Techniques," 1993.

[4] X. Xu, S. Meteyer, N. Perry, and Y. F. Zhao, "Energy consumption model of Binder-jetting additive manufacturing processes," *International Journal of Production Research*, vol. 53, no. 23, pp. 7005–7015, 2015.

[5] I. Gibson, D. Rosen, and B. Stucker, "Binder jetting," in *Additive Manufacturing Technologies: 3D Printing, Rapid Prototyping, and Direct Digital Manufacturing*, pp. 205–218, New York, NY: Springer New York, 2015.

[6] B. Levine, "A new era in porous metals: Applications in orthopaedics," *Advanced Engineering Materials*, vol. 10, no. 9, pp. 788–792, 2008.

[7] P. A. Banaszkiewicz, "Porous-coated hip replacement. The factors governing bone ingrowth, stress shielding, and clinical results," *Classic Papers in Orthopaedics*, vol. 69, no. 1, pp. 51–55, 2014.

[8] M. H. Lee, K. B. Kim, J. H. Han, J. Eckert, and D. J. Sordelet, "High strength porous Ti6Al4V foams synthesized by solid state powder processing," *Journal of Physics D: Applied Physics*, vol. 41, no. 10, p. 105404, 2008.

[9] H. Schiefer, M. Bram, H. P. Buchkremer, and D. Stöver, “Mechanical examinations on dental implants with porous titanium coating,” *Journal of Materials Science: Materials in Medicine*, vol. 20, no. 8, pp. 1763–1770, 2009.

[10] I. M. Robertson and G. B. Schaffer, “Some effects of particle size on the sintering of titanium and a master sintering curve model,” *Metallurgical and Materials Transactions A: Physical Metallurgy and Materials Science*, vol. 40, no. 8, pp. 1968–1979, 2009.

[11] L. Le Guéhennec, A. Soueidan, P. Layrolle, and Y. Amouriq, “Surface treatments of titanium dental implants for rapid osseointegration,” *Dental Materials*, vol. 23, no. 7, pp. 844–854, 2007.

[12] ASTM International, “F2792-12a - Standard Terminology for Additive Manufacturing Technologies,” *Rapid Manufacturing Association*, pp. 10–12, 2013.

[13] G. Strano, L. Hao, R. M. Everson, and K. E. Evans, “A new approach to the design and optimisation of support structures in additive manufacturing,” *International Journal of Advanced Manufacturing Technology*, vol. 66, no. 9-12, pp. 1247–1254, 2013.

[14] A. Hussein, L. Hao, C. Yan, R. Everson, and P. Young, “Advanced lattice support structures for metal additive manufacturing,” *Journal of Materials Processing Technology*, vol. 213, no. 7, pp. 1019–1026, 2013.

[15] E. O. Garzón, J. L. Alves, and R. J. Neto, “Post-process influence of infiltration on binder jetting technology,” in *Materials Design and Applications*, pp. 233–255, Cham, Switzerland: Springer International, 2017.

[16] E. Sachs, S. Allen, M. Cima, E. Wylonis, and H. Gu, “Production of Injection Molding Tooling With Conformal Cooling Channels Using the Three Dimensional Printing Process,” *Polymer Engineering and Science*, vol. 40, no. 5, pp. 1232–1247, 2000.

[17] B. Utela, D. Storti, R. Anderson, and M. Ganter, “A review of process development steps for new material systems in three dimensional printing (3DP),” *Journal of Manufacturing Processes*, vol. 10, no. 2, pp. 96–104, 2008.

[18] C. Polzin, S. Spath, and H. Seitz, “Characterization and evaluation of a PMMAbased 3D printing process,” *Rapid Prototyping Journal*, vol. 19, no. 1, pp. 37–43, 2013.

[19] A. Basalah, Y. Shanjani, S. Esmaeili, and E. Toyserkani, "Characterizations of additive manufactured porous titanium implants," *Journal of Biomedical Materials Research - Part B Applied Biomaterials*, vol. 100 B, no. 7, pp. 1970–1979, 2012.

[20] M. Ziaee, E. M. Tridas, and N. B. Crane, "Binder-Jet Printing of Fine Stainless Steel Powder with Varied Final Density," *Jom*, vol. 69, no. 3, pp. 592–596, 2017.

[21] M. Vlasea, E. Toyserkani, and R. Pilliar, "Effect of gray scale binder levels on additive manufacturing of porous scaffolds with heterogeneous properties," *International Journal of Applied Ceramic Technology*, vol. 12, no. 1, pp. 62–70, 2015.

[22] K. A. Williams, *Feasibility Study of Investment Casting Pattern Design by Means of Three Dimensional Printing*. PhD thesis, 1989.

[23] A. Curodeau, *Three Dimensional Printing; Machine Control From CAD Model to Nozzles*. PhD thesis, 1989.

[24] M. E. Jr., *Characterization of the Powder/Binder Interaction in the Three Dimensional Printing Process*. PhD thesis, 1988.

[25] ExOne, "Casting Media Alternatives," 2015.

[26] Voxeljet, "Material data sheet for Furan-Direct-Binding (FDB) sand molds,"

[27] J. Gonzalez, J. Mireles, Y. Lin, and R. Wicker, "Characterization of ceramic components fabricated using binder jetting additive manufacturing technology," *Ceramics International*, vol. 42, pp. 10559–10564, jul 2016.

[28] M. Cima, J. Yoo, S. Khanuja, M. Rynerson, D. Nammour, B. Giritlioglu, J. Grau, and E. Sachs, "Sturctural Ceramic Components by 3D Printing," *Solid Freeform Fabrication Symposium*, pp. 479–488, 1993.

[29] L. Ferrage, G. Bertrand, P. Lenormand, D. Grossin, and B. Ben-Nissan, "A review of the additive manufacturing (3DP) of bioceramics: Alumina, zirconia (PSZ) and hydroxyapatite," *Journal of the Australian Ceramic Society*, vol. 53, no. 1, pp. 11–20, 2017.

[30] L. Rabinskiy, A. Ripetsky, S. Sitnikov, Y. Solyaev, and R. Kahramanov, "Fabrication of porous silicon nitride ceramics using binder jetting technology," *IOP Conference Series Materials Science and Engineering*, vol. 140, no. 1, p. 12023, 2016.

[31] S. M. Gaytan, M. A. Cadena, H. Karim, D. Delfin, Y. Lin, D. Espalin, E. MacDonald, and R. B. Wicker, "Fabrication of barium titanate by binder jetting additive manufacturing technology," *Ceramics International*, vol. 41, no. 5, pp. 6610–6619, 2015.

[32] S. Shrestha and G. Manogharan, "Optimization of Binder Jetting Using Taguchi Method," *Jom*, vol. 69, no. 3, pp. 491–497, 2017.

[33] B. Zhang, Z. Zhan, Y. Cao, H. Gulan, P. Linnér, J. Sun, T. Zwick, and H. Zirath, "Metallic 3-D Printed Antennas for Millimeter- and Submillimeter Wave Applications," *IEEE Transactions on Terahertz Science and Technology*, vol. 6, no. 4, pp. 592–600, 2016.

[34] T. Do, P. Kwon, and C. S. Shin, "Process development toward full-density stainless steel parts with binder jetting printing," *International Journal of Machine Tools and Manufacture*, vol. 121, no. November 2016, pp. 50–60, 2017.

[35] F. Breu, S. Guggenbichler, and J. Wollmann, "Three Dimensional Printing of Tungsten Carbide-Cobalt using a Cobalt Oxide Precursor," *Solid Freeform Fabrication Symposium*, vol. 13, pp. 616–631, 2003.

[36] A. Mostafaei, K. A. Kimes, E. L. Stevens, J. Toman, Y. L. Krimer, K. Ullakko, and M. Chmielus, "Microstructural evolution and magnetic properties of binder jet additive manufactured Ni-Mn-Ga magnetic shape memory alloy foam," *Acta Materialia*, vol. 131, pp. 482–490, 2017.

[37] M. P. Paranthaman, C. S. Shafer, A. M. Elliott, D. H. Siddel, M. A. McGuire, R. M. Springfield, J. Martin, R. Fredette, and J. Ormerod, "Binder Jetting: A Novel NdFeB Bonded Magnet Fabrication Process," *Jom*, vol. 68, no. 7, pp. 1978–1982, 2016.

[38] L. Li, B. Post, V. Kunc, A. M. Elliott, and M. P. Paranthaman, "Additive manufacturing of near-net-shape bonded magnets: Prospects and challenges," *Scripta Materialia*, vol. 135, pp. 100–104, 2017.

[39] E. Sheydaeian and E. Toyserkani, "A system for selectively encapsulating porogens inside the layers during additive manufacturing: From conceptual design to the first prototype," *Journal of Manufacturing Processes*, vol. 26, pp. 330–338, 2017.

[40] Y. Bai and C. B. Williams, "An exploration of binder jetting of copper," *Rapid Prototyping Journal*, vol. 21, pp. 177–185, mar 2015.

[41] A. Mostafaei, Y. Behnamian, Y. L. Krimer, E. L. Stevens, J. L. Luo, and M. Chmielus, "Effect of solutionizing and aging on the microstructure and mechanical properties of powder bed binder jet printed nickel-based superalloy 625," *Materials and Design*, vol. 111, pp. 482–491, 2016.

[42] A. Mostafaei, E. L. Stevens, E. T. Hughes, S. D. Biery, C. Hilla, and M. Chmielus, "Powder bed binder jet printed alloy 625: Densification, microstructure and mechanical properties," *Materials and Design*, vol. 108, pp. 126–135, 2016.

[43] A. Mostafaei, J. Toman, E. L. Stevens, E. T. Hughes, Y. L. Krimer, and M. Chmielus, "Microstructural evolution and mechanical properties of differently heat-treated binder jet printed samples from gas- and water-atomized alloy 625 powders," *Acta Materialia*, vol. 124, pp. 280–289, 2017.

[44] P. Stoyanov, K. Andre, P. Prichard, M. Yao, and C. Gey, "Microstructural and Mechanical Characterization of Mo-containing Stellite Alloys Produced by three Dimensional Printing," *Procedia CIRP*, vol. 45, pp. 167–170, 2016.

[45] Xiaolin Chen, *Particle packing, compaction and sintering in powder metallurgy.* PhD thesis, 1998.

[46] S. J. Park, Y. Wu, D. F. Heaney, X. Zou, G. Gai, and R. M. German, "Rheological and thermal debinding behaviors in titanium powder injection molding," *Metallurgical and Materials Transactions A: Physical Metallurgy and Materials Science*, vol. 40, no. 1, pp. 215–222, 2009.

[47] C. Schade, "Blending and Premxing of Metal Powders and Binders," in *ASM Handbook*, vol. 7, ch. Powder Metallurgy, pp. 88–92, 1998.

[48] E. Sheydaeian, M. Vlasea, A. Woo, R. Pilliar, E. Hu, and E. Toyserkani, "Effect of glycerol concentrations on the mechanical properties of additive manufactured porous calcium polyphosphate structures for bone substitute applications," *Journal of Biomedical Materials Research - Part B Applied Biomaterials*, vol. 105, no. 4, pp. 828–835, 2017.

[49] E. J. R. Parteli and T. Pöschel, "Particle-based simulation of powder application in additive manufacturing," *Powder Technology*, vol. 288, pp. 96–102, 2016.

[50] M. Vlasea, R. Pilliar, and E. Toyserkani, "Control of structural and mechanical properties in bioceramic bone substitutes via additive manufacturing layer stacking orientation," *Additive Manufacturing*, vol. 6, pp. 30–38, 2015.

[51] H. Miyanaji and L. Yang, “Equilibrium Saturation in Binder Jetting Additive Manufacturing Processes: Theoretical Model Vs. Experimental Observeations,” *Solid Freeform Fabrication Symposium*, pp. 1945–1959, 2016.

[52] A. Bose, “Introduction to Metal Powder Injection Molding,” in *ASM Handbook*, vol. 7, ch. Debinding, pp. 823–847, 2015.

[53] Y. Bai, G. Wagner, and C. B. Williams, “Effect of Bimodal Powder Mixture on Powder Packing Density and Sintered Density in Binder Jetting of Metals,” *2015 Annual International Solid Freeform Fabrication Symposium*, vol. 139, no. August, p. 62, 2015.

[54] R. M. German, “Coarsening in Sintering: Grain Shape Distribution, Grain Size Distribution, and Grain Growth Kinetics in Solid-Pore Systems,” *Critical Reviews in Solid State and Materials Sciences*, vol. 35, no. 4, pp. 263–305, 2010.

[55] E. a. Olevsky, “Theory of sintering: from discrete to continuum,” *Materials Science and Engineering: R*, vol. 23, no. 2, pp. 41–100, 1998.

[56] S. Matsusaka, H. Maruyama, T. Matsuyama, and M. Ghadiri, “Triboelectric charging of powders: A review,” *Chemical Engineering Science*, vol. 65, no. 22, pp. 5781–5807, 2010.

[57] T. Kojima and J. A. Elliott, “Incipient flow properties of two-component fine powder systems and their relationships with bulk density and particle contacts,” *Powder Technology*, vol. 228, pp. 359–370, 2012.

[58] E. Eylon and F. Froes, “Products, Properties and Selection: Nonferrous Alloys and Special-Purpose Materials,” in *ASM Handbook*, vol. 2, ch. Titanium Powder Metallurgy, pp. 647–660, 1990.

[59] G. Lütjering and J. Williams, “Fundamental Aspects,” in *Titanium*, pp. 15–52, second ed., 2007.

[60] F. Froes, “Titanium Powder Metallurgy: A Review - Part 1,” *Advanced Materials and Processes*, vol. 170, no. 9, pp. 16–23, 2012.

[61] C. Tkaczyk and M. Tabrizian, “Biocompatibility, Metal Ions, and Corrosion Products,” in *ASM handbook*, vol. 23, ch. Materials for Medical devices, pp. 47–55, 2012.

[62] G. Lutjering and J. Williams, “Special Properties and Applications of Titanium,” in *Titanium*, pp. 383–415, second ed., 2007.

[63] S. Lampman, “Titanium and Its Alloys for Biomedical Implants,” in *ASM Handbook*, vol. 23, ch. Materials for Medical Devices, pp. 223–236, 2015.

[64] F. Campbell, “Titanium,” in *Elements of Metallurgy and Engineering Alloys*, pp. 527–543, 2008.

[65] G. Lutjering and J. Williams, “Commercially Pure (CP) Titanium and Alpha Alloys,” in *Titanium*, pp. 175–201, seconds ed., 2007.

[66] R. P. Elliott, “Diffusion in Titanium and Titanium Alloys: Technical Documentary Report NO. ASD-TDR-62-561,” tech. rep., Air Force Systems Command Wright-Patterson, 1962.

[67] G. Lutjering and J. Williams, “High Temperature Alloys,” in *Titanium*, pp. 259–282, second ed., 2007.

[68] M. Qian, G. Schaffer, and C. Bettles, “Sintering of Titanium and Its Alloys,” in *Sintering of Advanced Materials*, pp. 324–355, 2010.

[69] ASTM, “B348-13: Standard Specification for Titanium and Titanium Alloy Bars and Billets,” *Astm*, vol. 02.04, p. 8, 2015.

[70] V. Duz, A. Klevtsov, and V. Sukhoplyuyev, “Production of Titanium Powders,” in *ASM Handbook*, vol. 7, ch. Powder Metallurgy, pp. 642–649, 2015.

[71] M. Entezarian, F. Allaire, P. Tsantrizos, and R. A. L. Drew, “Plasma atomization: A new process for the production of fine, spherical powders,” *Jom*, vol. 48, no. 6, pp. 53–55, 1996.

[72] O. D. Neikov, D. V. Lotsko, V. G. Gopienko, S. S. Naboychenko, I. V. Frishberg, and I. B. Murashova, “Powder Production Methods,” in *Handbook of Non-Ferrous Metal Powders*, pp. 45–222, 2009.

[73] R. M. German, “Thermodynamics of Sintering,” in *Sintering of Advanced Materials*, pp. 3–32, 2010.

[74] J. Johnson and R. German, “Theoretical modeling of densification during activated solid-state sintering,” *Metallurgical and Materials Transactions A: Physical Metallurgy and Materials Science*, vol. 27, no. 2, pp. 441–450, 1996.

[75] R. M. German, “Sintering Simplified: Surface Area, Density, and Grain Size Relations,” *Materials Science Forum*, vol. 835, no. January, pp. 50–75, 2016.

[76] Z. Z. Fang and H. Wang, "Sintering of ultrafine and nanosized particles," in *Sintering of Advanced Materials*, pp. 434–473, 2010.

[77] R. M. German, P. Suri, and S. J. Park, "Review: Liquid phase sintering," *Journal of Materials Science*, vol. 44, no. 1, pp. 1–39, 2009.

[78] L. De Jonghe and M. Rahaman, "Sintering of Ceramics," in *Handbook of Advanced Ceramics*, pp. 187–264, 2003.

[79] M. N. Rahaman, "Kinetics And Mechanisms of Densification," in *Sintering of Advanced Materials*, pp. 33–64, 2010.

[80] W. D. Kingery and M. Berg, "Study of the initial stages of sintering solids by viscous flow, evaporation-condensation, and self-diffusion," *Journal of Applied Physics*, vol. 26, no. 10, pp. 1205–1212, 1955.

[81] H. Su and D. L. Johnson, "Master Sintering Curve: A Practical Approach to Sintering," *Journal of the American Ceramic Society*, vol. 79, pp. 3211–3217, dec 1996.

[82] D. Y. Park, S. W. Lee, S. J. Park, Y.-s. Kwon, and I. Otsuka, "Effects of Particle Sizes on Sintering Behavior of 316L Stainless Steel Powder," *Metallurgical and Materials Transactions A*, vol. 44A, pp. 1508–1518, 2012.

[83] D. C. Blaine, S. J. Park, P. Suri, and R. M. German, "Application of work-of-sintering concepts in powder metals," *Metallurgical and Materials Transactions A: Physical Metallurgy and Materials Science*, vol. 37, no. 9, pp. 2827–2835, 2006.

[84] I. D. Jung, S. Ha, S. J. Park, D. C. Blaine, R. Bollina, and R. M. German, "Two-Phase Master Sintering Curve for 17-4 PH Stainless Steel," *Metallurgical and Materials Transactions A: Physical Metallurgy and Materials Science*, vol. 47, no. 11, pp. 5548–5556, 2016.

[85] I. M. Robertson and G. B. Schaffer, "Refinement of master densification curves for sintering of titanium," *Metallurgical and Materials Transactions A: Physical Metallurgy and Materials Science*, vol. 41, no. 11, pp. 2949–2958, 2010.

[86] I. M. Robertson and G. B. Schaffer, "Comparison of sintering of titanium and titanium hydride powders," *Powder Metallurgy*, vol. 53, no. 1, pp. 12–19, 2010.

[87] P. Garg, S. J. Park, and R. M. German, "Effect of die compaction pressure on densification behavior of molybdenum powders," *International Journal of Refractory Metals and Hard Materials*, vol. 25, no. 1, pp. 16–24, 2007.

[88] D. C. Blaine, J. D. Gurosik, S. J. Park, R. M. German, and D. F. Heaney, "Master sintering curve concepts as applied to the sintering of molybdenum," *Metallurgical and Materials Transactions A*, vol. 37, no. March, pp. 715–720, 2006.

[89] V. Pouchly and K. Maca, "Master sintering curve - A practical approach to its construction," *Science of Sintering*, vol. 42, no. 1, pp. 25–32, 2010.

[90] O. Guillon and J. Langer, "Master sintering curve applied to the Field-Assisted Sintering Technique," *Journal of Materials Science*, vol. 45, no. 19, pp. 5191–5195, 2010.

[91] R. Caruso, N. Mamana, and E. Benavidez, "Densification kinetics of ZrO2-based ceramics using a master sintering curve," *Journal of Alloys and Compounds*, vol. 495, no. 2, pp. 570–573, 2010.

[92] D. Li, S. O. Chen, X. Q. Sun, W. Q. Shao, Y. C. Zhang, and S. S. Zhang, "Construction and validation of master sintering curve for TiO2 for pressureless sintering," *Advances in Applied Ceramics*, vol. 107, no. 1, pp. 52–56, 2008.

[93] D. Li, S. Chen, Y. Jing, W. Shao, Y. Zhang, and W. Luan, "The master sintering curve for pressureless sintering of TiO2," *Science of Sintering*, vol. 39, no. 2, pp. 103–110, 2007.

[94] D. Li, S. Chen, W. Shao, X. Ge, Y. Zhang, and S. Zhang, "Densification evolution of TiO2 ceramics during sintering based on the master sintering curve theory," *Materials Letters*, vol. 62, no. 6-7, pp. 849–851, 2008.

[95] J. D. Hansen, R. P. Rusin, M. H. Teng, and D. L. Johnson, "Combined-Stage Sintering Model," *Journal of the American Ceramic Society*, vol. 75, no. 5, pp. 1129–1135, 1992.

[96] R. M. German, "Sintering densification for powder mixtures of varying distribution widths," *Acta Metallurgica Et Materialia*, vol. 40, no. 9, pp. 2085–2089, 1992.

[97] R. T. Dehoff, "Path and Kinetics of Microstructural Change in Simple Sintering," in *Sintering of Advanced Materials*, pp. 65–85, 2010.

[98] C. B. Diantonio and K. G. Ewsuk, "Master SinteringCcurve and Its Application in Sintering of Electronic Ceramics," in *Sintering of Advanced Materials*, pp. 130–161, 2010.

[99] S. J. Park, J. M. Martin, J. E. Guo, J. L. Johnson, and R. M. German, "Grain growth behavior of tungsten heavy alloys based on the master sintering curve concept," *Metallurgical and Materials Transactions A: Physical Metallurgy and Materials Science*, vol. 37, no. 11, pp. 3337–3346, 2006.

[100] S. Kiani, J. Pan, and J. A. Yeomans, "A new scheme of finding the master sintering curve," *Journal of the American Ceramic Society*, vol. 89, no. 11, pp. 3393–3396, 2006.

[101] K. An, "Pressure assisted master sintering surface of Co, Cu and Fe powder mixture," *Powder Technology*, vol. 234, pp. 117–122, 2013.

[102] B. Brandt and T. Rabe, "Compilation and Evaluation of the Pressure-Assisted Master Sintering Surface for Low-Temperature Cofired Ceramics," *Journal of the American Ceramic Society*, vol. 98, no. 11, pp. 3503–3508, 2015.

[103] P. Hidnert, "Thermal expansion of titanium," *Journal of Research of the National Bureau of Standards*, vol. 30, no. 2, p. 101, 1943.

[104] C. Ryan, *The Processing and Characterization of Porous Ni / YSZ and NiO / YSZ Composites used in Solid Oxide Fuel Cell Applications by*. PhD thesis, 2006.

[105] R. R. Thridandapani, D. C. Folz, and D. E. Clark, "Estimation of activation energies for sintering 8 mol % Yttria-Zirconia using conventional and microwave heating," *International Journal of Applied Ceramic Technology*, vol. 11, no. 5, pp. 938–945, 2014.

[106] T. T. Fang, J. T. Shiue, and F. S. Shiau, "On the evaluation of the activation energy of sintering," *Materials Chemistry and Physics*, vol. 80, no. 1, pp. 108–113, 2003.

[107] M. J. Starink, "The determination of activation energy from linear heating rate experiments: A comparison of the accuracy of isoconversion methods," *Thermochimica Acta*, vol. 404, no. 1-2, pp. 163–176, 2003.

APPENDICES

Appendix A

Background Information

A.1 Titanium

Table A.1: Composition of commercially pure titanium grades 7, 11, 16 and 17 [69]

	Content (weight percent)			
Element	grade 7/7H	grade 11	grade 16/16H	grade 17
Carbon (max)	0.08	0.08	0.08	0.08
Oxygen (max)	0.25	0.18	0.25	0.18
Nitrogen (max)	0.03	0.03	0.03	0.03
Hydrogen (max)	0.015	0.015	0.015	0.015
Iron (max)	0.30	0.20	0.30	0.20
Palladium	0.12-0.25	0.12-0.25	0.04-0.08	0.04-0.08
Other (individual - max)	0.1	0.1	0.1	0.1
Other (total - max)	0.4	0.4	0.4	0.4

Table A.2: Composition of commercially pure titanium grades 16 and 27 [69]

	Content (weight percent)	
Element	grade 26/26H	grade 27
Carbon (max)	0.08	0.08
Oxygen (max)	0.25	0.18
Nitrogen (max)	0.03	0.03
Hydrogen (max)	0.015	0.015
Iron (max)	0.30	0.20
Ruthenium	0.08-0.14	0.08-0.14
Other (individual - max)	0.1	0.1
Other (total - max)	0.4	0.4

A.2 Master Sinter Curve Creation

$$\frac{100\rho_s}{\rho_{th}} = a + \frac{e-a}{1+exp\left(\frac{(b-ln\Theta)}{c}\right)} \tag{A.1}$$

Table A.3: Sigmoidal constants for equation A.1 [86]

Parameter	Description
ρ_s	sintered density
ρ_{th}	theoretical density
a, b and c	determined from least squares fits
e	maximum relative density

$$\rho = \rho_0 + \frac{1-\rho_0}{1+exp\left(-\frac{(ln\Theta-a)}{b}\right)} \tag{A.2}$$

$$\rho = \rho_0 + \frac{a}{\left[1+exp\left(-\frac{(log\Theta-log\theta_0)}{b}\right)\right]^c} \tag{A.3}$$

Table A.4: Sigmoidal constants for equation A.2 [82]

Parameter	Description	Equality
ρ	relative density	-
ρ_0	green relative density	-
a	work of sintering at sintering midpoint	a$\equiv$ $ln\Theta_{ref}$, Θ_{ref}=Θ when $\rho = \frac{1}{2}(\rho_0 + 1)$
b	inverse of the diffusion coefficient	b$\equiv$1/n, n = 3,4 (volume, boundary diffusion)

Table A.5: Sigmoidal constants for equation A.3 [98]

Parameter	Description
ρ	density
ρ_0	initial density
Θ_0	Θ value at inflection point of fit curve
a	difference between green and maximum densities, a=$(\rho_{max} - \rho_0)$
b and c	curve shape parameters

Appendix B

System Development

As mentioned previously, there has been a significant amount of work done on BJAM process parameters and the resulting effects. The work done in this thesis has expanded the understanding of the sintering process. This combined knowledge is sufficient to allow, in theory, both the green and sintered parts. One persisting issue with BJAM, is that no commercially available system allows users to adjust critical printing parameters to gain full control over part properties. Another issue is that all BJAM systems have large build capacities. This is because the system are either targeted at prototypes or larger, industrial parts. In addition to process control, a BJAM system for the medical and dental field requires a small build volume since the feedstock materials are expensive.

A system has already been developed in the MSAM lab has a small build volume as well as full process parameter control. The printer allows for the use of up to three powder types, the insertion of sacrificial elements, and adjustment of the printing parameters on a per-layer basis. This amount of control gives very good part consistency and allows one to truly optimize the part for a specific application. While the system does perform well, it was designed and built solely as a research platform, making the system large and giving it relatively poor usability. For the knowledge gained through both this and previous works to be implemented, a printer with good usability must be developed, while still including enough advanced features to give meaningful control over the produced parts.

This chapter details the development of a small-scale BJAM printer that includes many of the advanced features of the research platform, but with more of an emphasis on size, usability, and to a lesser degree, aesthetics. The system presented in this chapter was not fully designed as part of this thesis work, but was designed in two distinct stages. The initial system development was done as part of a Capstone Design Project at the University of Waterloo. The Capstone Design Project group was comprised of five additional students (six total) and the work done includes the full system design, including electrical, sensing, firmware and software. The printer made for the Capstone Design Project was subsequently improved as part of this thesis work to make the system in its current form. The work done during the Capstone Design Project constitutes iteration one of the system. Evaluation of the iteration one system and development of the iteration two system constitute the work done as part of this thesis.

B.1 Iteration One System

As previously mentioned, the general idea behind the printer was to make a small-scale BJAM system for the medical and dental field. It was anticipated that this system could be deployed by dentists or dental technicians who were already making custom dental restorations. From this anticipated locale, it was assumed that this system could be used by general staff, as opposed to highly trained and experienced technicians. Being in a commercial space, the system has to be fully enclosed to prevent powder, a possible health and fire hazard, from entering into the environment. Some consideration also has to be put towards the aesthetics of the system, since it is more likely to be seen by customers or the general public. Since the system was also intended to be used by less technically trained staff, the system had to be user-friendly. The principles of safety, aesthetics and usability were the driving factors behind many of the design choices.

Before proper design choices began, some aspects of the system were predefined due to time and cost limitations. One major aspect of the printer that was predefined was the print head used to deposit the binder. The print head was chosen as the Mark 610 print head from ImTech. This print head is currently in use in the aforementioned research platform, and its performance and interfacing is well known. In addition, the controller for this model of print head was available for use. Purchasing another controller was not possible due to limited funds. ImTech is an OEM reseller for Hewlett-Packard (HP), and the Mark 610 print head is based around the HP 45 print head and its corresponding print head seat. The (HP model no) print head and ImTech controller combination meant that the image resolution for printing was set as 600 DPI. In addition, the print width of the (HP model no.) is 0.5in (12.7mm). The Mark 610 is intended for industrial printing applications, and its outer case is quite large, making the system fairly robust. This specific design is unsuitable and unnecessary for the envisioned small-scale BJAM system and the outer case from ImTech was removed. The removal of the outer case significantly reduced the print head size B.1 case and removed HP seat], making it more reasonable to use in the system.

Another predefined aspect of the printer was the inclusion of automated features, specifically for bulk powder dispensing (into the feed bed) and powder collection. This was to be incorporated to make the system more user friendly for users with less technical expertise. It was also done in an attempt to reduce powder exposure. By automating the

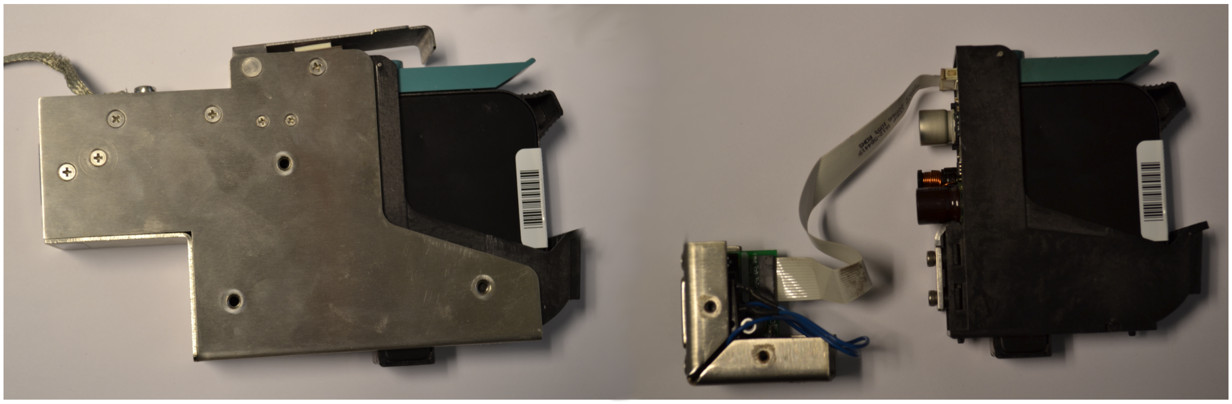

Figure B.1: Comparison of the IMTech print head inside of the provided case (left) and removed to reduce overall size (right)

powder dispensing and part cleaning, the system would only need to be opened to retrieve the final part. Taking into account the predefined aspects of the printer, some specifications were developed based on anticipated use and knowledge gained from experience using other systems. The specifications include both design constraints and design objectives. The constraints reflect what had to be included in the printer based on previous experience while the objectives reflect the performance and capabilities that were desired in the system. The objectives and constraints for the system are listed in Table B.1.

Table B.1: Iteration One System Objectives and Constraints

Subsystem	Objectives	Constraints
1.Gantry	• +/- 50μm movement accuracy • Should have +/- 50μ accuracy for print head location • Should be able to move from dock position to print position in 1 second	• Must be able to move print head to print bed • Must be able to move material from material bed to print bed • Must be able to dock print head for cleanup process • Must not be able to drive out of bound • Must be able to collect finish part
2.Material Dispensing and Cleaning	• Store 5 full feed beds of material in cartridge • Binder cartridge stores enough material to use at least an entire powder cartridge	• Powder must be contained (move from cartridge to feed bed without spreading to rest of printer) • Part cleaning system must not damage green part

Table B.1: Iteration One System Objectives and Constraints

Subsystem	Objectives	Constraints
3.Main Printer Structure	• Small footprint (less than 50cm x 50 cm) • Small height (less than 50cm) • lightweight (less than 25kg) • Easy to manufacture, assemble and maintain • Highly aesthetically appealing to the user	• All powder is contained within the printing area (cannot spread to other parts of the printer or outside of the printer) • Reasonable footprint to fit on a desk (less than 75cm x 75cm) • Reasonable height (less than 75cm) • Light enough to be easily carried by two people (less than 50kg) • Allows access for maintenance of all parts of the printer

Table B.1: Iteration One System Objectives and Constraints

Subsystem	Objectives	Constraints
4.Printer Beds	• No powder escapes either bed during motion • Bed positional tolerance of +/- 5μm	• Beds must be sealed to contain powder to a reasonable amount (lose less than 1%) • Beds must have a positional tolerance of +/- 25μm
5.Firmware and Interface	• Processing of images should take less than 5 minutes • Some form of interface is on the system	• Provide suitable interface between PC and microcontroller • Provide suitable interface between microcontroller and low level drivers • Generate printing paths from images sent by the PC • Microcontroller must accept sensor I/O and deal with them accordingly

Table B.1: Iteration One System Objectives and Constraints

Subsystem	Objectives	Constraints
6. Powder Dispensing	• Accuracy of +/- 5% for dispensing • Accuracy of +/- 5% for storage sensing	• Must dispense sufficient material for the part printing • Must include mechanism for refill • Must be able to sense the amount of stock material in container and notify user for in sufficient amount for printing
7.Software and User Interface	• User computer can connect to printer via wifi • All print data stored on the printer (do not need constant connection to user computer)	• Software must be able to import standard 3D file formats • Software must send layer-by-layer information to firmware • Software must run on mainstream, off-the-shelf operating systems

Table B.1: Iteration One System Objectives and Constraints

Subsystem	Objectives	Constraints
8. Power and Wiring	• All printer systems run off a single power supply unit • Electrical components located to minimize the amount of wiring	• Printer must be able to run off of 120V AC wall plug • All of the sensors must be connected to the printer microcontroller • All of the electronics must be tied to a common ground • Printer must be safety grounded • No exposed leads on any of the wiring

Both the objectives and constraints include information on the software, sensors and power distribution of the system. This information is included to give a better overall representation of the developed system. Since the work on the electrical, firmware and software was completed by others, it will not be discussed in detail. Those different aspects of the printer will be mentioned only when they impact the design of the mechanical architecture, which is the focus of the work in this thesis.

From preliminary design discussions with the group for the iteration one design, it became apparent that none of the electrical or control systems would have a serious impact on the overall size of the system. Though some accommodation would have to be done for larger electrical components, mainly the motors and power supplies, these systems would be substantially smaller than all of the mechanical systems in the printer. From these discussions, it was decided that the mechanical system would be designed first, with the electrical aspects included after. Based on the design requirements, the mechanical system was split into four major subsystems. These subsystems are: powder handling, gantry, bulk material handling and system frame. The powder handling subsystem includes the portions of the printer that come into contact with and control and contain powder during the printing process. Included in this subsystem is the main powder spreading surface, the powder bed shafts and the beds themselves. The gantry subsystem is made up of, as the name implies, the main gantry in the printer. The gantry is the main moving system in the printer which spreads powder and moves the print head, allowing it to print. The bulk material handling subsystem is comprised of the containers and feeding systems that deliver powder and binder for printing, but also collect waste powder and binder during and after the printing process. The system frame is made up of structural components that support all of the the other systems as well as the outer case.

The breakdown of the mechanical subsystems was done since it provided a good design flow for the full development. The powder handling subsystem determined where the beds were and how the powder would move during printing. This subsystem is also the most critical in determining the size of the parts that can be made and the vertical layer resolution. This layout determined the size, orientation and location of the gantry, since both the roller and print head have to move in relation to the beds and printing surface. Both the powder handling and gantry in turn determine the design of the bulk material handling subsystem. The powder handling subsystem determines where the bulk material must be delivered to and removed from while the gantry determines some spacial constraints (the bulk material handling cannot interfere with the gantry motion) and any motion aspects of the bulk material subsystem. With all of these subsystems designed, the frame and outer case can be designed to fix the necessary components in place and enclose the entire printer. While not specific to the design process, the break down of the main mechanical design also allowed for an easier allocation of work to different members in the iteration one design group.

In general, the system met all of the requirements that were specified before work began. The developed system is shown in B.2. It was chosen to orient the beds along the x-axis, see, making the system wider than it was deep. The gantry was split into two distinct sections, the section on the left was used for printing, while the section on the right was for powder cleaning. A standard lead screw and piston design was chosen for the bed motion [image reference]. Though alternative options were considered early on, they were deemed too difficult to implement within the alloted project time. The bulk material feed was located above the gantry, and the bulk material collection below the main build plate, allowing for gravity to assist with material distribution. The x-axis drive was mounted below the main surface plate to prevent powder contact. All other major electrical controllers and drivers were also mounted below the main surface plate to prevent powder intrusion.

The major deviation from the initial design specification for the iteration one design was with regards to the bulk material handling subsystem. Though included in the printer, it was never fully implemented. The bulk binder feed and collection portions were functional but were found to be detrimental to print quality. The inlet to the print head is located on the bottom of the cartridge, meaning the feeding tube and connector were located between

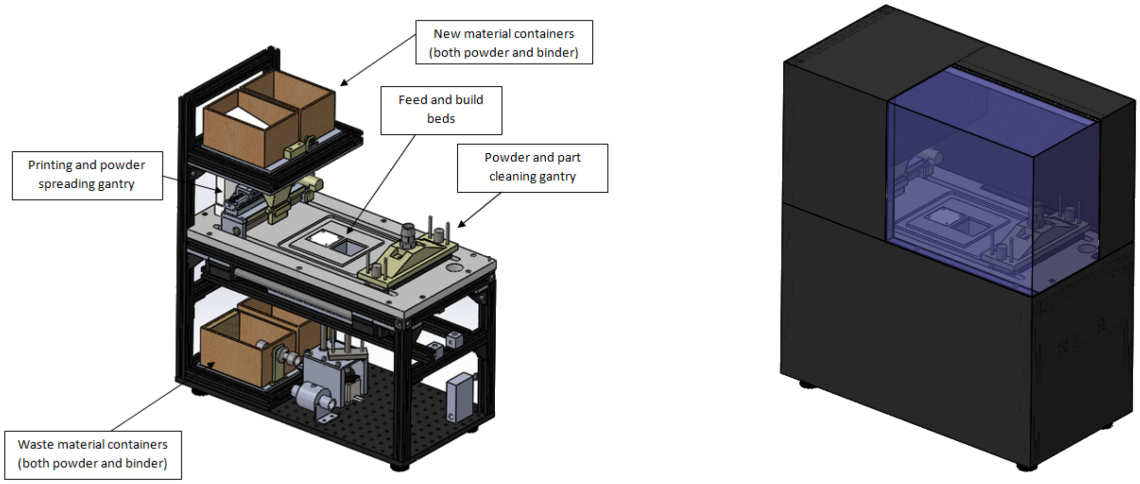

Figure B.2: Iteration One system overview with and without the outer case

the print head and the powder on the main surface plate, see B.3. The location of these connections caused disturbances of the powder during the printing process, reducing build quality. In addition, it was found the print head itself had a large enough reservoir to allow for large prints without needing refilling.

The bulk powder feed portion also worked, but to allow for consistent feeding, a significant amount of space in the cartridge had to consist of angled surfaces to give consistent feeding, see B.4. Due to size limitations, the powder supply container held a relatively small amount of material. The powder collection system was never made to work as intended. The issue with the system was mainly due to poor design. The system could not be troubleshooted and fixed due to time constraints during the initial system design, construction and evaluation.

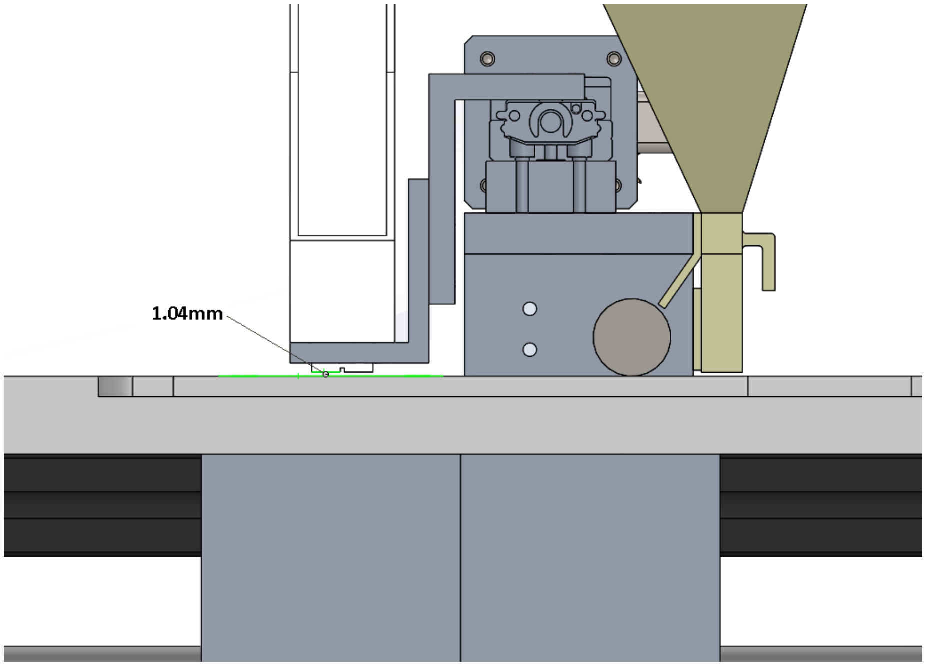

Figure B.3: Spacing between the print head and powder spreading surface

B.1.1 Evaluation of the Iteration One System

Though the iteration one system was functional, there were found to be a number of issues with the system. Some of the issues were self imposed due to time and cost considerations, some were inherent to the design and some were simply due to poor part quality, manufacture and assembly. The major failings with the system were primarily with the mechanical architecture. This area of the system is where the major improvements were focused for the iteration two system. Due to limited funds, a full system re-design could not be completed, so a targeted retrofit of the existing system was done instead.

The major area of the printer that was addressed was the x-axis motion of the gantry. The x-axis had fairly poor motion for three major reasons. The first issue is due to the actual design of the guide rods and mounting. The gantry is mounted using bushing blocks,

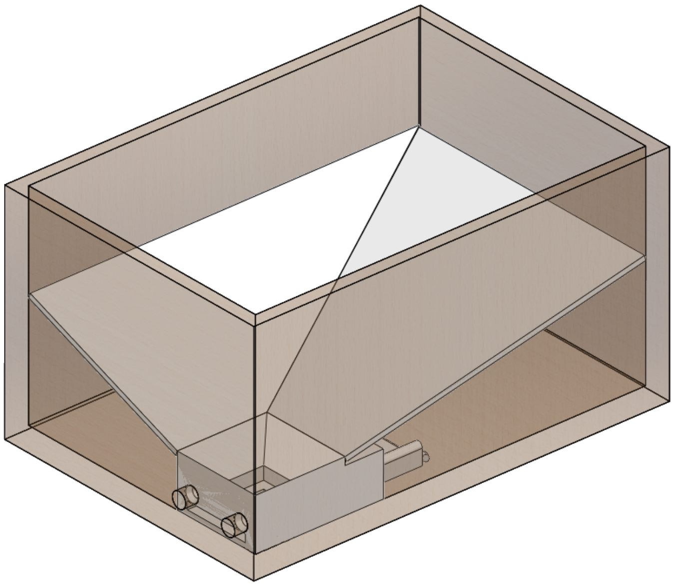

Figure B.4: Interior space of the powder supply container showing the limited capacity due to the required sloping surfaces

both of which ride on guide rods. During motion, the gantry is located using the two axes of the guide rods, shown in Figure B.5. Each guide rod and bushing block is a cylindrical joint, allowing for a degree of freedom (DOF) of 2. In addition, the gantry acts as a closed kinematic chain since each end of the gantry is connected to the ground. from the analysis of Figure B.5 the number of links in the system is two (N=2), the number of joints is two (j=2), and each joint has a DOF of two (f_1=f_2=2). The Mobility formula, Equation B.1 is evaluated, and the DOF of the system is found to be negative two (M=-2).

$$M = 6(N - 1 - j) + \sum_{j}^{i=1} f_i \tag{B.1}$$

Since the gantry has a negative DOF, but can still move in one direction (parallel to the

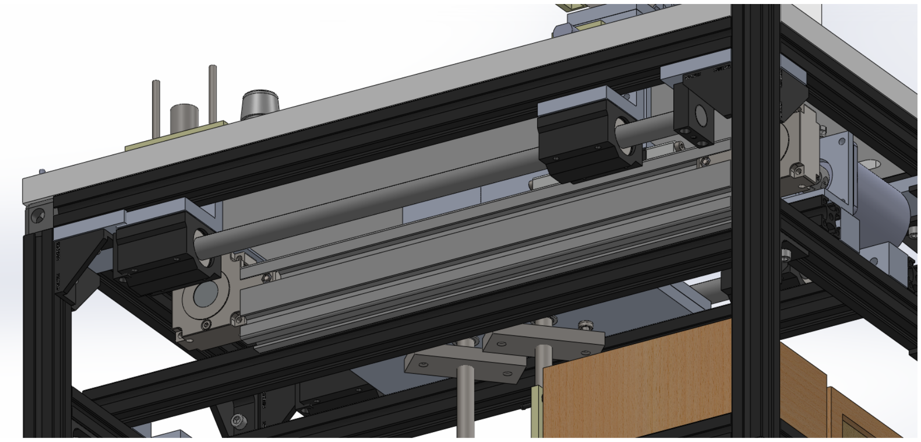

Figure B.5: Schematic showing the x-axis guide-rod and bushing block mounted to the extrusion-based system frame

rod axes), the gantry is an overconstrained system. The issue of overconstraint is overcome as long as the two guide rods are perfectly cylindrical, perfectly spaced and perfectly aligned. The motion of the system relies explicitly on this exact geometry. Some minor deviation is allowable since the ball bearings inside the bushings are spring-loaded, and will still function even if there is some misalignment. Unfortunately, the second issue with the x-axis gantry, namely the relatively poor machining quality and selection of mounting components, caused more misalignment than what the bushings could compensate for. Even with careful assembly and alignment of the parts, consistent motion could not be achieved over the full travel length of the x axis. Though unrelated to the mechanical design, the control architecture of the x-axis motor was also found to not have any ramp-up during motion. This lack of extra torque during the initial motion, while not directly responsible, exacerbated the issue.

The next major issue observed with the system was with the top surface plate. The plate was machined within specifications, but the plastic material was weak enough that two major issues occurred First, the plate deflected during the printing process when the beds moved. Though the plate was strong enough to support its own weight, the frictional forces from the felt seals in the beds causes the plate to deflect, both up and down, in the direction of bed motion. Figure B.6 shows a 100N loading applied to the surfaces retaining the shafts with the edges of the plate fixed. As can be seen in Figure B.6, this relatively low level of applied force is enough to deflect the plate fairly substantially. While this motion was not consistent, it was detrimental during builds when it occurred. When the shafts (and subsequently the plate) moved up, it was possible for the roller to hit the top surface plate, preventing good motion. When the shafts were moved down, the roller was not able to contact enough powder during spreading to properly fill the build shaft. The other issue with the top surface plate was that the soft material scored easily. While there were no significant effects when printing with titanium, there was concerns that if other, harder materials were used, it would scratch the top surface plate excessively.

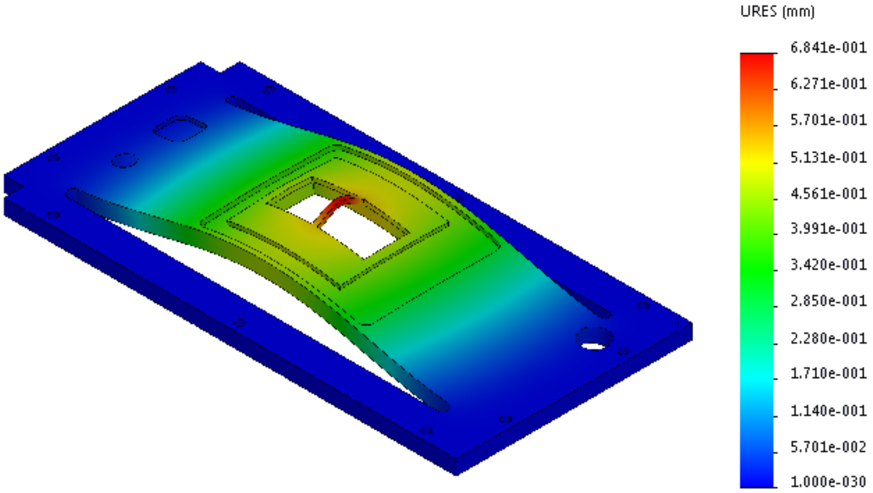

Figure B.6: Iteration One system top surface plate deflection from to 100N loading

Another major issue with the printer concerns powder control and isolating critical components. The cut outs and mounting of the x-axis motion components below the top surface plate effectively shielded them from powder during the printing process. Unfortunately, during part cleaning and powder removal, it was found the powder could easily fall down these cutouts and get onto the electrical board covers, shown in Figure B.7. Though still technically shielded from the powder, this spread of powder into the internal areas of the printer was concerning. If powder was able to get into the electronics, it could easily damage the printer or cause a fire hazard. In addition, the bottom of the printer is effectively open, since it is a breadboard with tapped holes. It is therefore possible for the powder to fall down, all the way through the printer, and out through the bottom plate. This powder leakage can pose a health hazard, especially since it is difficult to detect if powder is escaping the machine.

B.2 Iteration Two System

With the identification of these major issues in the iteration one system, a second system was developed. In iteration two of the system, many components were redesigned and were made with proper tolerances and surface finishes. Apart from the main gantry, it was part quality, rather than the actual design that was the cause of performance issues. In general, most of the issues surrounding the mechanical system of the printer were resolved simply by improving the machining quality of the parts. However, the aforementioned areas of the mechanical system required a more thorough reworking.

The first major aspect of the system that was addressed was the bulk material handling subsystem. The subsystem was never fully implemented in the iteration one system since parts of the subsystem either did not work, or made it less convenient to use the printer. It was decided to fully remove the material handling subsystem, rather than fix it. The material handling subsystem, even if it had worked reliably, made using the printer more

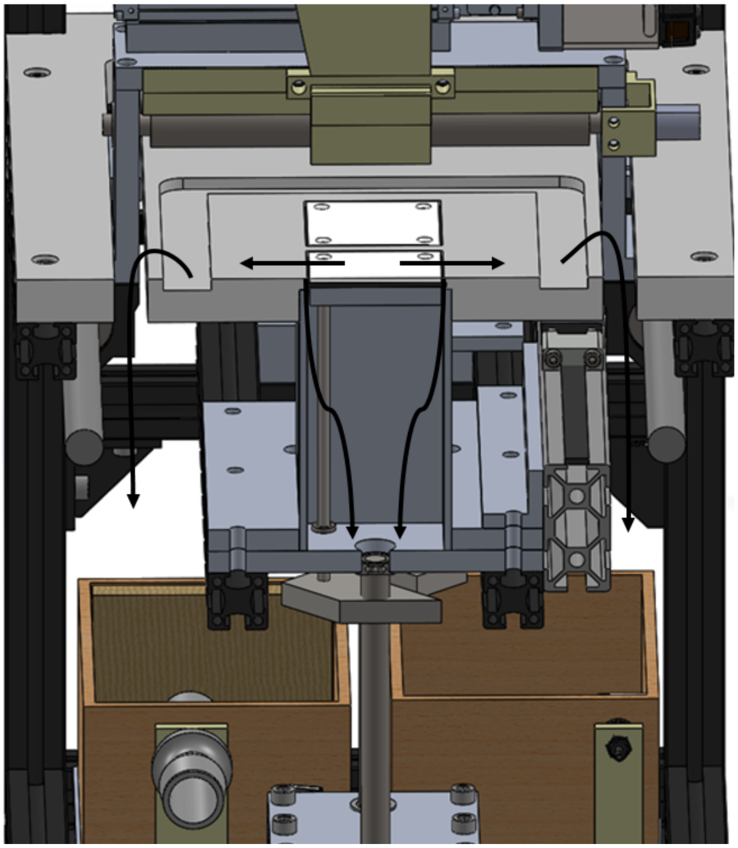

Figure B.7: Powder infiltration route into the iteration one system interior

onerous. In addition, the improvement of reliability likely would have come at the cost of an increase in system size to fully implement the automated features in a practical way. With limited resources, and a focus on making the printer as easy to use as possible, it was decided that there was no major benefit in improving the material handling subsystem to a usable level, and it was therefore removed. The removal of the subsystem was a relatively easy task since it was never fully implemented. The only major change to the system was to the frame, shown in Figure B.8. Initially, the frame extended above the main surface plate to support the material containers. The frame could now be cut down, which reduced system size, cost and made the design simpler.

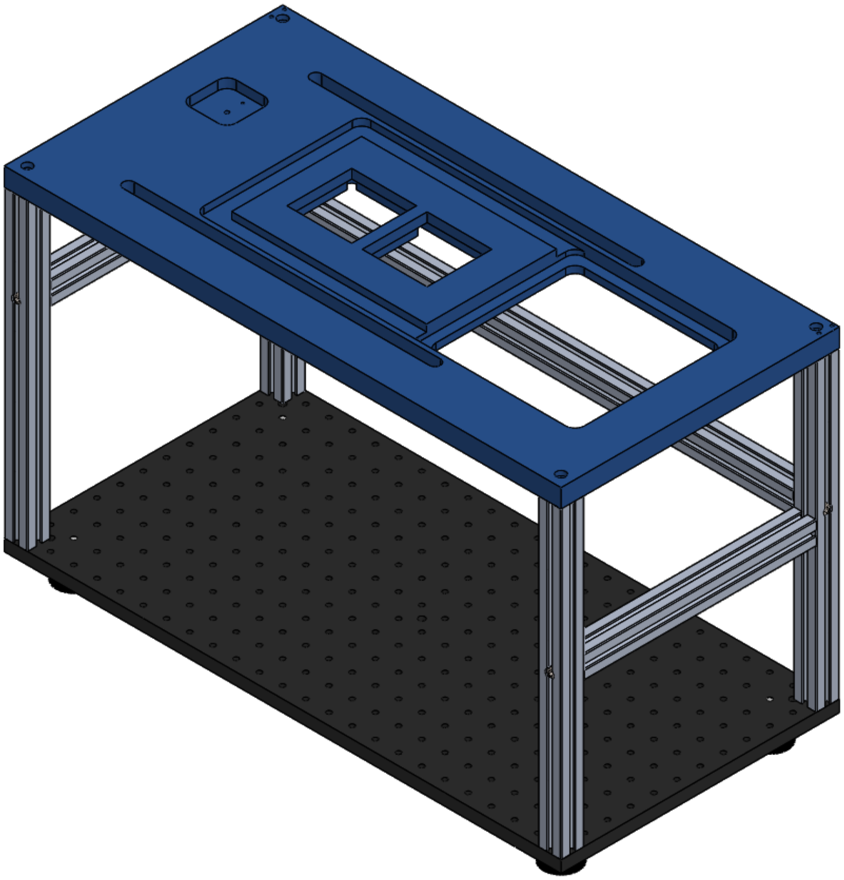

Figure B.8: Schematic showing the overall change in frame design after removing the bulk material handling subsystem

The next aspect of the printer that was addressed was the x-axis gantry. The design of the gantry was not fundamentally changed, but the mounting location was. Mounting was moved from the extruded frame material to the underside of the top surface plate, shown in Figure B.9. The initial mounting design made mounting fairly simple, but made proper locating impossible. The new method of mounting directly to the top surface plate is less flexible, but it gives consistent and reliable mounting. The improvement in part quality, and the proper locating and mounting means the guide rods are located close enough that the bushings can accommodate the overconstrained design. The other fix to the subsystem was the addition of a ramp up of the x-axis motor. This provides more torque at the onset of motion, allowing the gantry to overcome static frictional forces more easily and give more consistent motion.

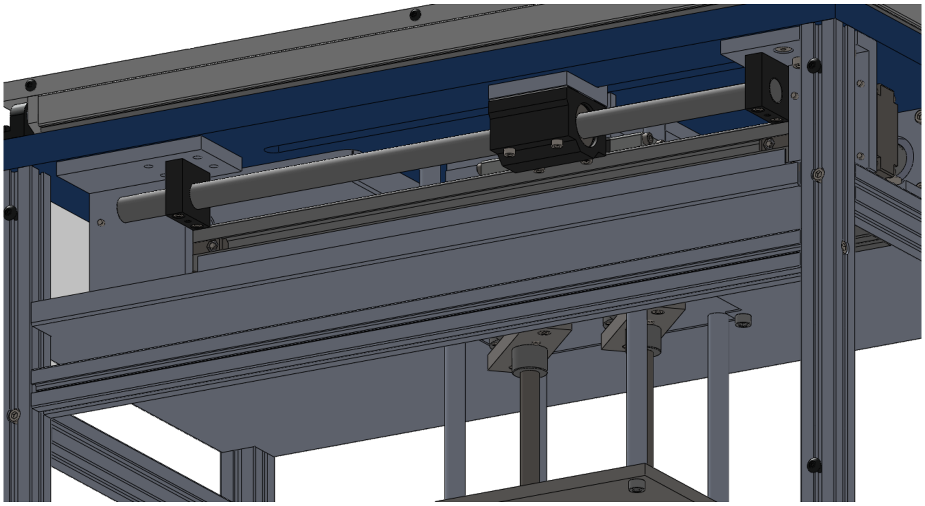

Figure B.9: Schematic showing the change in the x-axis guide-rod and bushing block mounting, with components now mounted directly to the top surface plate

Another major aspect of the printer that was addressed was the top surface plate. As mentioned previously, there was no major issues with the design, or manufactures of the plate in the iteration one system. The issue was with the plastic material being too weak to resist the forces applied to it from the bed shafts during bed motion. The solution was to replace the plastic top surface plate with a machined aluminum plate. The aluminum plate has significantly higher rigidity than the plastic, which removes the issue of deflection, as shown in Figure B.10. To prevent possible issues with scratches, the top surface plate is to be hard anodized.

The final major deficiency that was addressed with the iteration one design was the infiltration of powder into the system interior. With no resources to complete a major

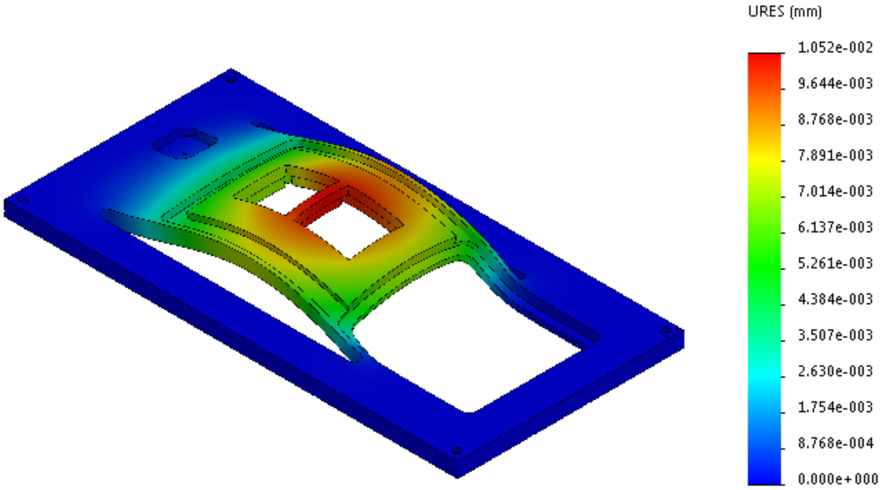

Figure B.10: Iteration two top surface plate deflection from 100N loading

redesign, the gantry design was fundamentally the same. This also meant that the cutouts for the gantry mounting brackets were also still present in the iteration two design. Since the cutouts could not be closed, the only other solution was to sufficiently catch the powder after it has fallen through to prevent it from reach the sensitive areas of the printer. This was done by integrating a catch pan into the system interior, see Figure B.11. The pan is mounted just below the pistons for the beds, with all of the bed motors and system electronics being shielded from powder. Though it does not prevent powder infiltration, it does reduce the associated hazards significantly. The powder can no longer reach electrical systems and damage the printer or cause a fire. The powder is also retained inside the printer where it cannot present a health hazard. There is concern that powder build up in the catch pan could become excessive, but this can be mitigated simply by cleaning the pan as part of routine maintenance.

The other main aspect of the printer that was changed is the outer case. This change

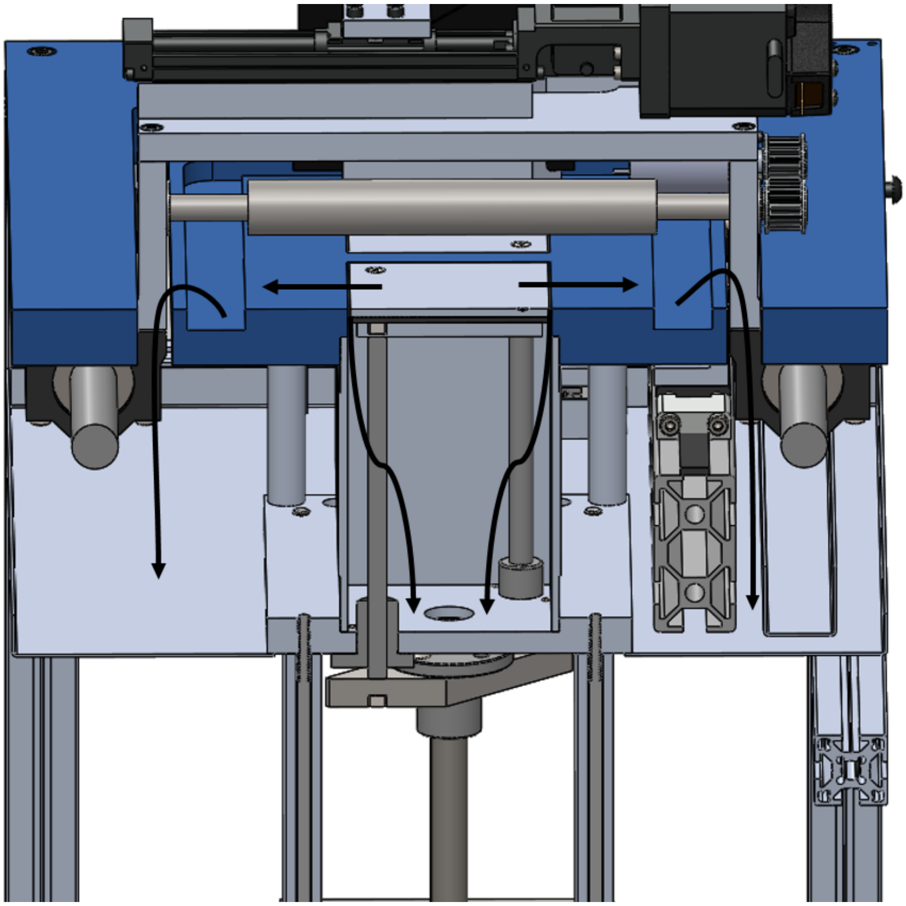

Figure B.11: Overview showing the system powder catch pan a the subsequent blockage of the powder infiltration route

has no affect on the actual production of parts on the system but was done to improve the usability of the printer and the general aesthetics. With the removal of the material handling subsystem, the outer case could more easily be split into two main components, an upper and lower case shown Figure B.12. The lower case is composed of a u-shaped front piece and a back panel.The lips on the u-shaped front piece allow it to grip the printer frame using sprint tension. With the front panel held on by spring tension, it does not require bolts at the front of the system, improving aesthetics. The second major component of the case is the top cover. The top cover is a basic rectangular frame with a clear lid. Again, while this change has no impact on the actual printing process, it makes accessing the entirety of the printing area very easy and gives a full view of the printing process even when the lid is closed.

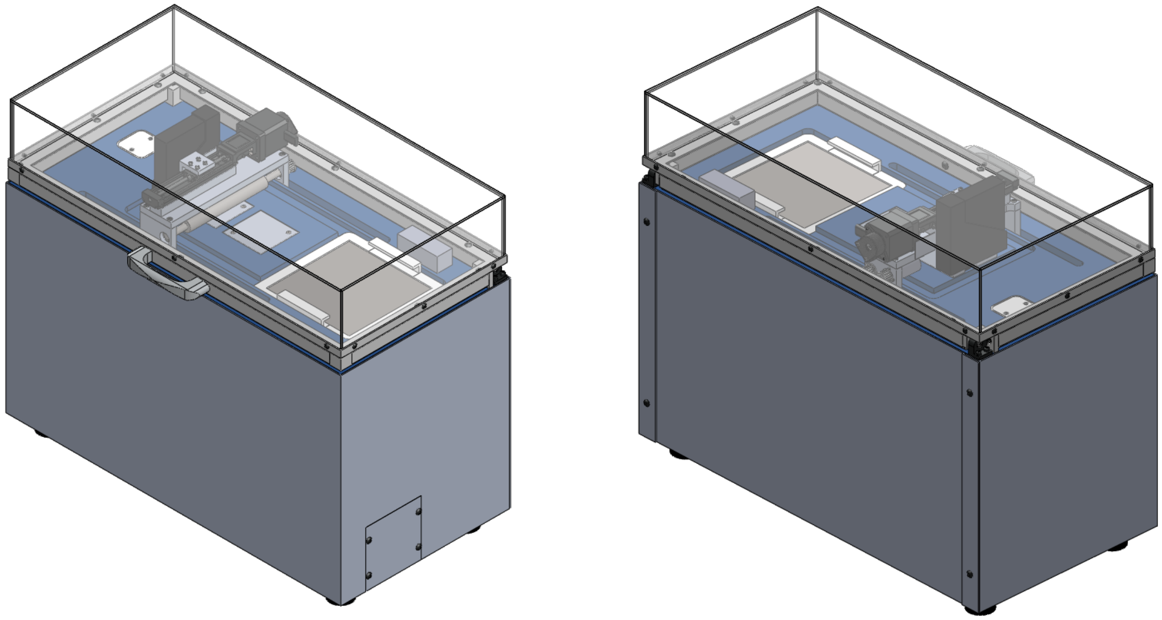

Figure B.12: CAD rendering of the Iteration two system outer case

B.2.1 Iteration Two System Overview

In addition to the major changes done, most of the mechanical system components were remade to improve fit and finish. Some components were modified slightly in either design or mounting orientation, but were not fundamentally altered.The changes provided a significant benefit to the overall system usability. The system as it is currently configured is shown in Figure B.13. The system still requires some further work. First, the top surface plate needs to undergo the hard anodizing treatment. The system was assembled before anodizing to allow for modifications if required. Another aspect of the system that needs to be modified is the software. Only minor changes to gantry positioning need to be completed to account for changes in the top surface plate. Once those two items are addressed, the system will be fully operational for printing.

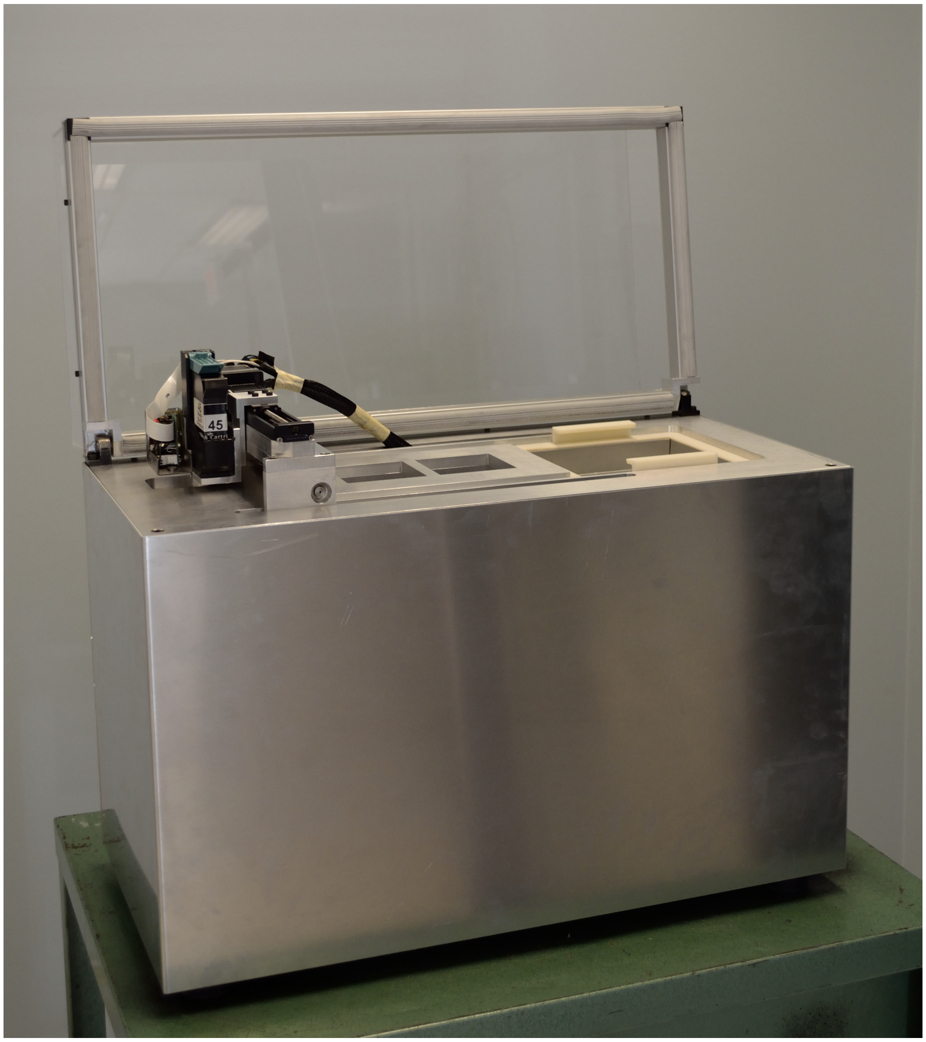

Figure B.13: Overall image of the constructed Iteration two system

Appendix C

Matlab Code for Making a Master Sinter Curve

C.1 Description of the Code

The Matlab code was generated and run in Matlab R2015a. The code imports two text files of the corrected and zeroed data for processing. The code is modified for each powder type to select the correct folder location and individual files located within. The code generates the integrand and subsequently the MPS for both heating rates. The code processes the data for a range of activation energies. From the results, a plot of error versus Q is found, allowing for the construction of the MSC. The MSC is generated using the same code, except the code is run for a single Q value, as opposed for to the full range of initial values.

C.2 From the Command Line

Finding apparent activation energy:

```
%function MSC_Q_Calc()
%General notes:
%The code requries already corrected (CTE) and zeroed (time) data to work.
%The tool runs through the Q values for a specific range, but can be done
%for a single value by manually enetering it (replace Q(k)) and commenting
%out the main loop.

R = 8.314;%J/mol k
Q = [20:20:600]%kJ;

cd 'file location';%file location

fid = fopen('1C/min file');
A = textscan(fid, '%f%f%f','Delimiter','\t');
c1 = cell2mat(A);

fid = fopen('3C/min file');
A = textscan(fid, '%f%f%f','Delimiter','\t');
c3 = cell2mat(A);

length1 = length(c1);
length3 = length(c3);
```

```
lengthq = length(Q);

Err = zeros(lengthq,1);

for k=1:lengthq
%generate integrand values for finding MSPs
for j=1:length1
c1(j,4)= ((1./c1(j,2)).*exp(-(1000.*Q(k))./(R.*c1(j,2))));
end

for j=1:length3
c3(j,4)= ((1./c3(j,2)).*exp(-(1000.*Q(k))./(R.*c3(j,2))));
end
%sum the integrand values and multiply by time (trapazoidal
%integration)
for j=1:length1-1
c1(j,5)= (c1(j,4) + c1(j+1,4))./2.*(c1(j+1,1)-c1(j,1));
c1(j,6) = log(sum(c1(1:j,5)));
end

for j=1:length3-1
c3(j,5) = (c3(j,4) + c3(j+1,4))./2.*(c3(j+1,1)-c3(j,1));
c3(j,6) = log(sum(c3(1:j,5)));
end
```

```
%remove inf/-inf/0
c1 = c1( ~any( isnan( c1 ) | isinf( c1 ), 2 ),: );
c3 = c3( ~any( isnan( c3 ) | isinf( c3 ), 2 ),: );%remove inf/-inf/0

%update lengths
length1 = length(c1);
length3 = length(c3);

%create a single x and y value set for curve fitting
xx = [c1(:,6)];
xx = [xx; c3(:,6)];

yy = [c1(:,3)];
yy = [yy; c3(:,3)];

%curve fitting - use Matlab curve fitting toolbox
[xData, yData] = prepareCurveData( xx, yy );
ft = fittype( ’0.59+((0.9-0.59)./(1+exp(-(x-a)./b)))’, ’independent’, ’x’, ’dependent’
opts = fitoptions( ’Method’, ’NonlinearLeastSquares’ );
opts.StartPoint = [-10 1];

[fitresult{5}, gof(5)] = fit( xData, yData, ft, opts );

%Save error value (root mean square error)
Err(k) = gof(5).rmse;
```

```
end

plot (Q,Err(:,1));

%end
```

Generating the MSC:

```
%function MSC_Run()
%General notes:
%The code requries already corrected (CTE) and zeroed (time) data to work.
%The tool geenerates the MSC for a single Q value

R = 8.314;%J/mol k
Q = 100%kJ;

cd 'file location';%file location

fid = fopen('1C/min file');
A = textscan(fid, '%f%f%f','Delimiter','\t');
c1 = cell2mat(A);

fid = fopen('3C/min file');
A = textscan(fid, '%f%f%f','Delimiter','\t');
c3 = cell2mat(A);
```

```
length1 = length(c1);
length3 = length(c3);
lengthq = length(Q);

%generate integrand values for finding MSPs
for j=1:length1
c1(j,4)= ((1./c1(j,2)).*exp(-(1000.*Q)./(R.*c1(j,2))));
end

for j=1:length3
c3(j,4)= ((1./c3(j,2)).*exp(-(1000.*Q)./(R.*c3(j,2))));
end
%sum the integrand values and multiply by time (trapazoidal
%integration)
for j=1:length1-1
c1(j,5)= (c1(j,4) + c1(j+1,4))./2.*(c1(j+1,1)-c1(j,1));
c1(j,6) = log(sum(c1(1:j,5)));
end

for j=1:length3-1
c3(j,5) = (c3(j,4) + c3(j+1,4))./2.*(c3(j+1,1)-c3(j,1));
c3(j,6) = log(sum(c3(1:j,5)));
end
```

```
%remove inf/-inf/0
c1 = c1( ˜any( isnan( c1 ) | isinf( c1 ), 2 ),: );
c3 = c3( ˜any( isnan( c3 ) | isinf( c3 ), 2 ),: );%remove inf/-inf/0

%update lengths
length1 = length(c1);
length3 = length(c3);

%create a single x and y value set for curve fitting
xx = [c1(:,6)];
xx = [xx; c3(:,6)];

yy = [c1(:,3)];
yy = [yy; c3(:,3)];

%curve fitting - use Matlab curve fitting toolbox
[xData, yData] = prepareCurveData( xx, yy );
ft = fittype( ’0.59+((0.9-0.59)./(1+exp(-(x-a)./b)))’, ’independent’, ’x’, ’dependent’
opts = fitoptions( ’Method’, ’NonlinearLeastSquares’ );
opts.StartPoint = [-10 1];

[fitresult{5}, gof(5)] = fit( xData, yData, ft, opts );
f = fit( xData, yData, ft, opts );

plot (c1(:,6),c1(:,3));
```

```
hold on
plot (c3(:,6),c3(:,3));
hold on
plot (f,xData,yData);
hold on

end
```

Appendix D

Sinter Structure Analysis Results

D.1 Overall Part Comparisons

These are orthogonal views of each of the CT samples in the Green and sintered state where the image size has been fixed to show the relative size between samples before and after sintering.

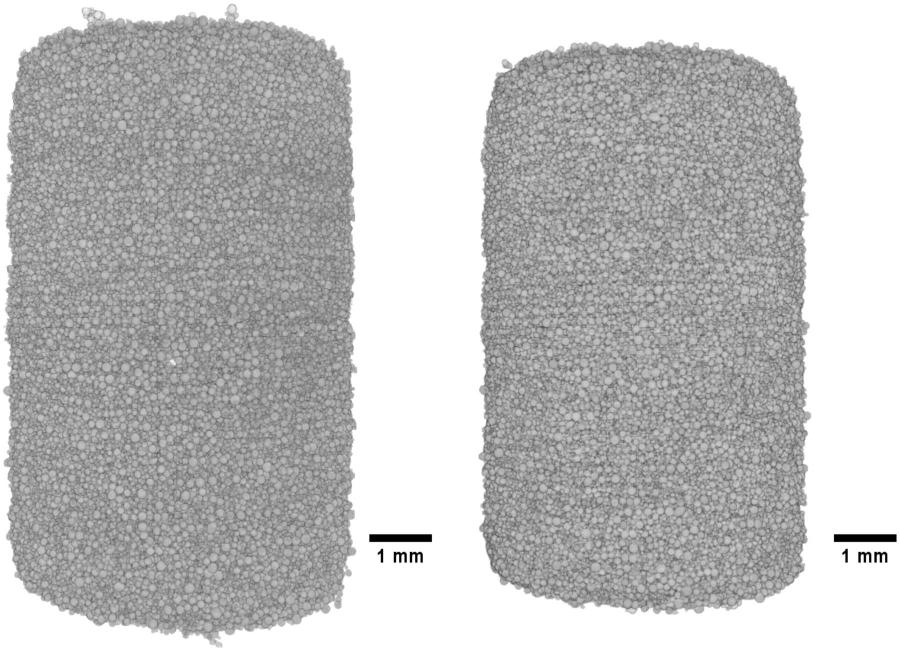

Figure D.1: Orthogonal view comparison between sample CT-AL in the green (left) and sintered (right) state

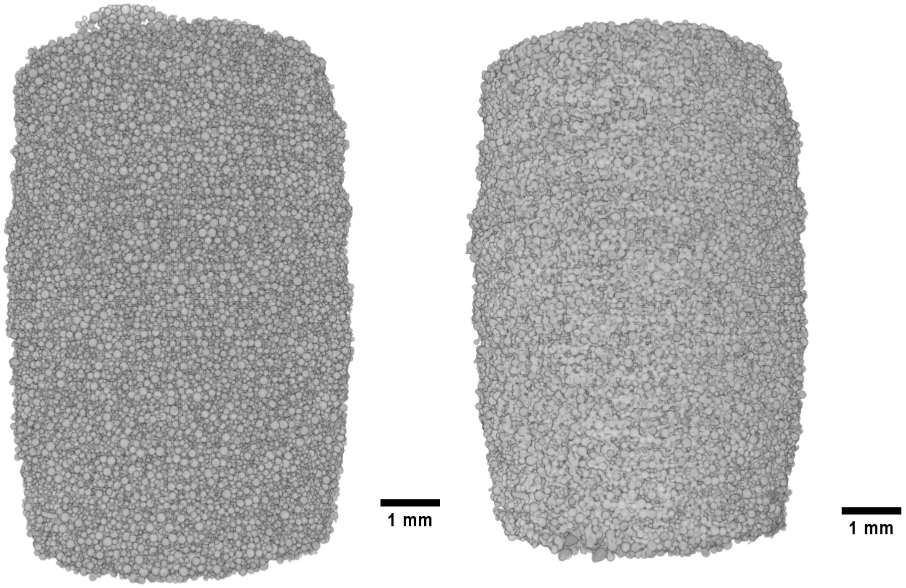

Figure D.2: Orthogonal view comparison between sample CT-AH in the green (left) and sintered (right) state

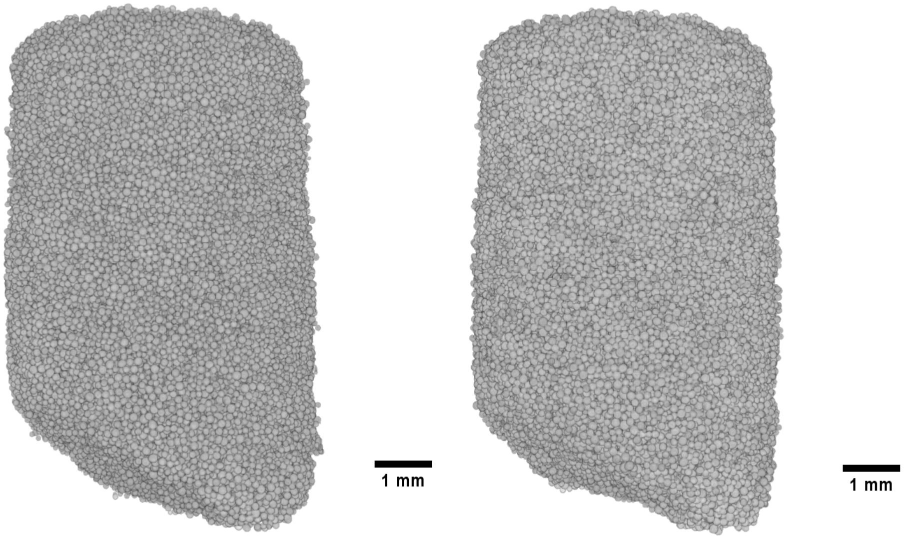

Figure D.3: Orthogonal view comparison between sample CT-BL in the green (left) and sintered (right) state

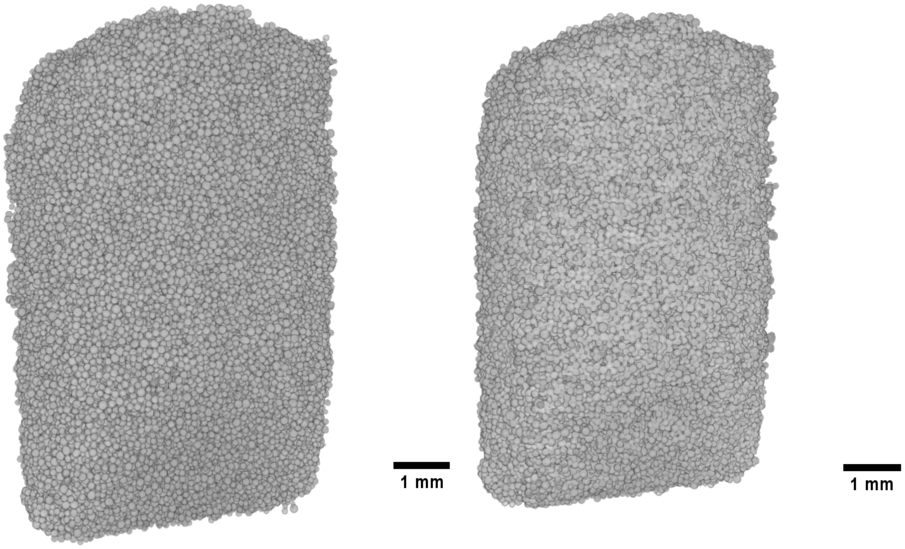

Figure D.4: Orthogonal view comparison between sample CT-BH in the green (left) and sintered (right) state

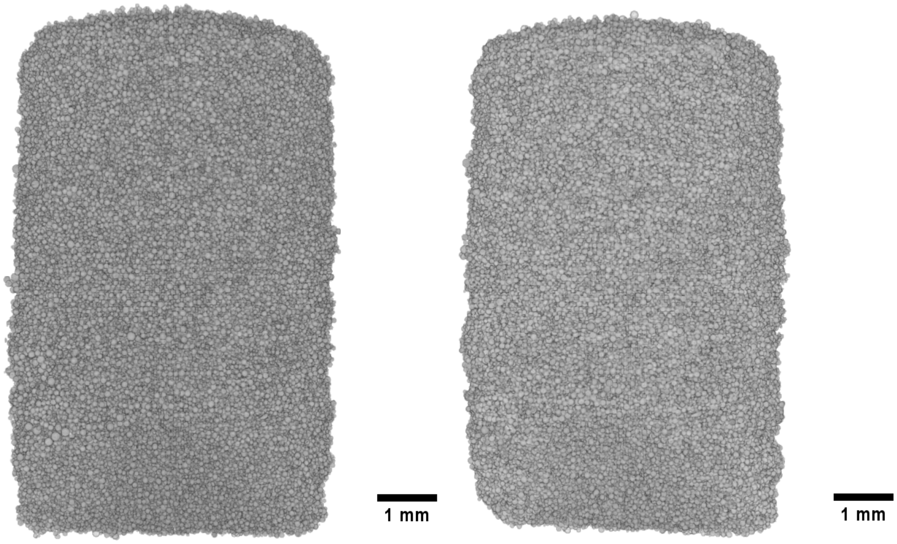

Figure D.5: Orthogonal view comparison between sample CT-CL in the green (left) and sintered (right) state

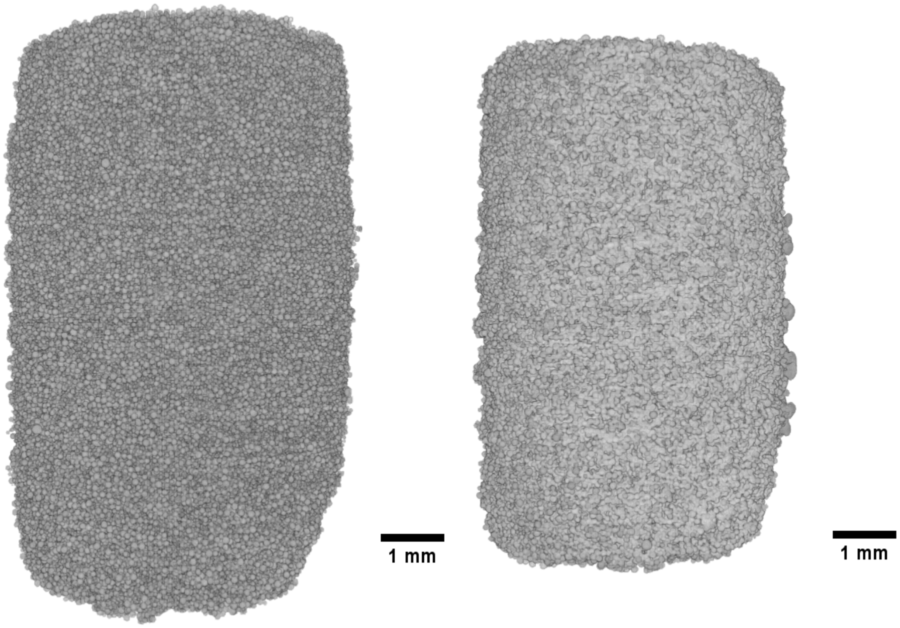

Figure D.6: Orthogonal view comparison between sample CT-CH in the green (left) and sintered (right) state

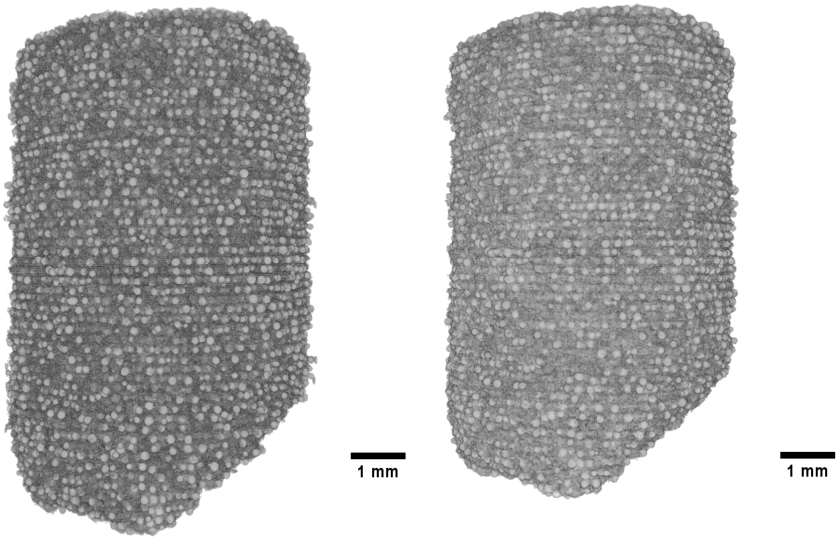

Figure D.7: Orthogonal view comparison between sample CT-DL in the green (left) and sintered (right) state

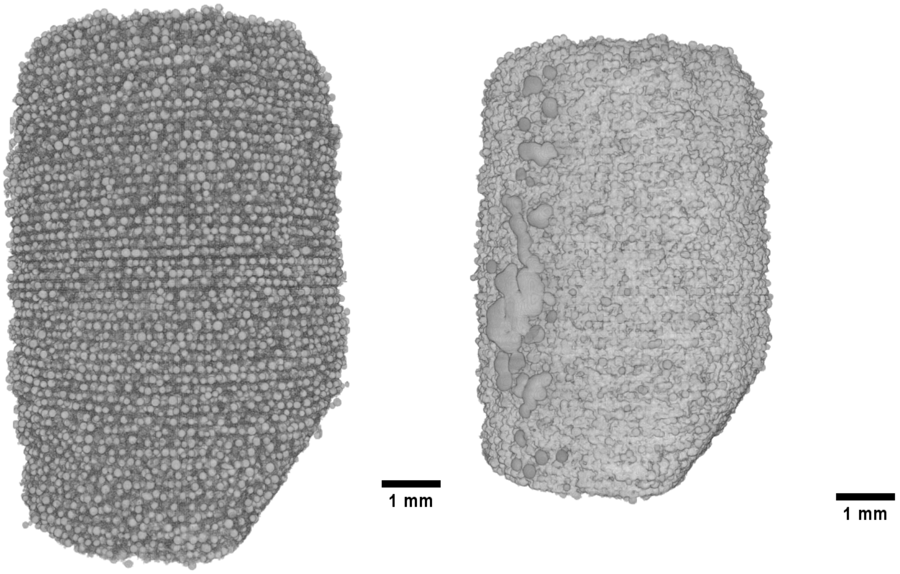

Figure D.8: Orthogonal view comparison between sample CT-DH in the green (left) and sintered (right) state

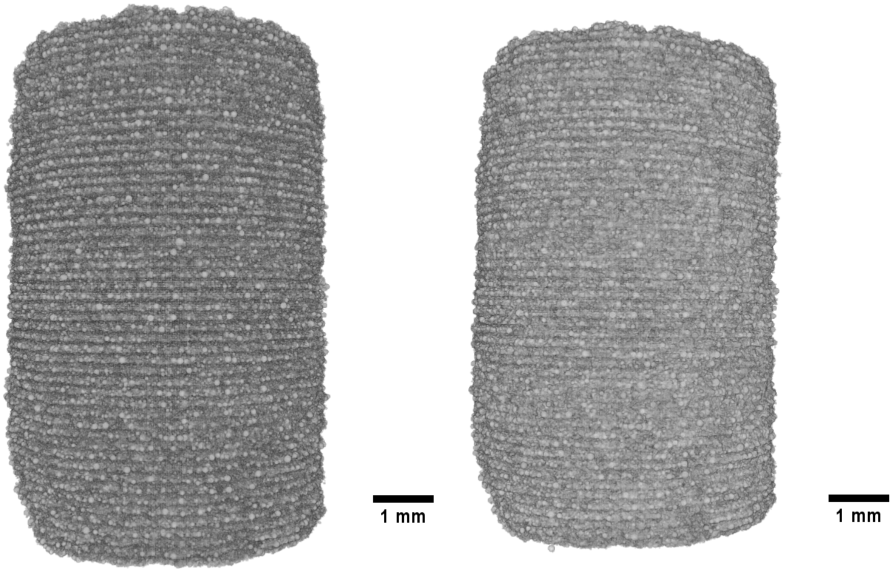

Figure D.9: Orthogonal view comparison between sample CT-EL in the green (left) and sintered (right) state

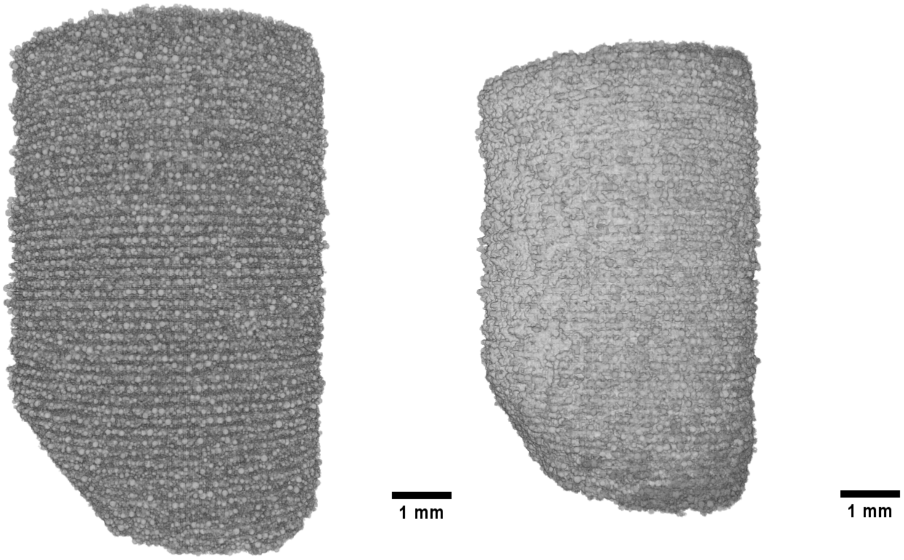

Figure D.10: Orthogonal view comparison between sample CT-EH in the green (left) and sintered (right) state

Appendix E

Master Sinter Curve Analysis Results

E.1 Differential Scanning Calorimetry Data

Plots of the DSC data obtained from samples made from all powder types as well as a solid sample. The plots show specific heat capacity (Cp) as well as heat flow. Plots show the uncompensated data (all samples) as well as data compensated using the solid sample.

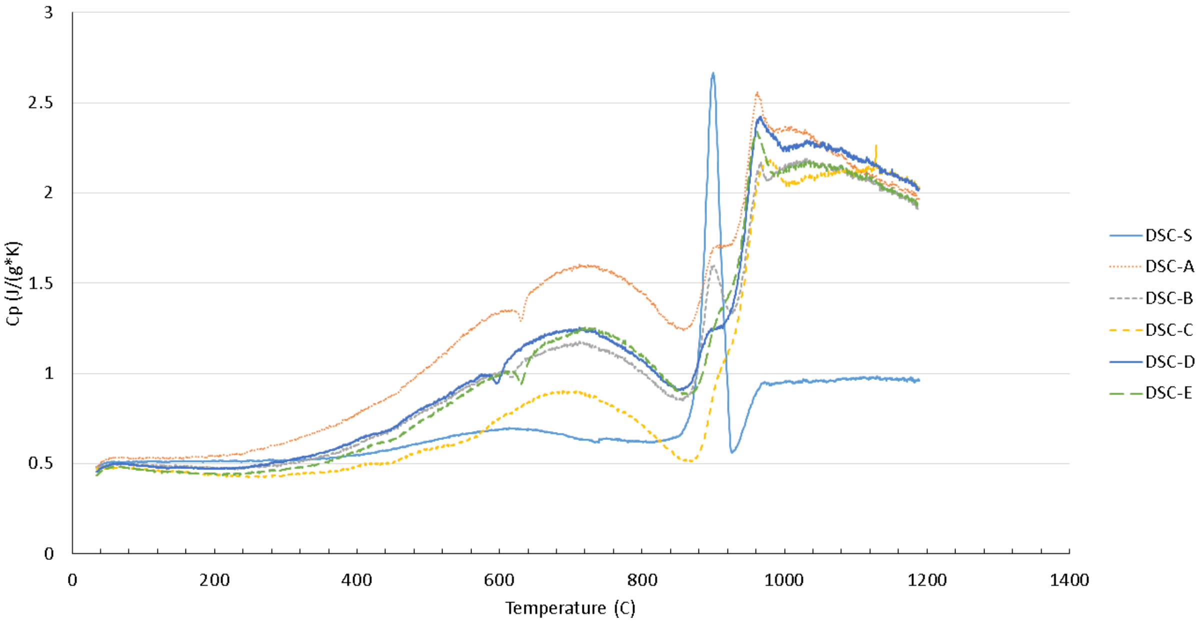

Figure E.1: Specific heat capacity (Cp) versus temperature of the un-compensated data

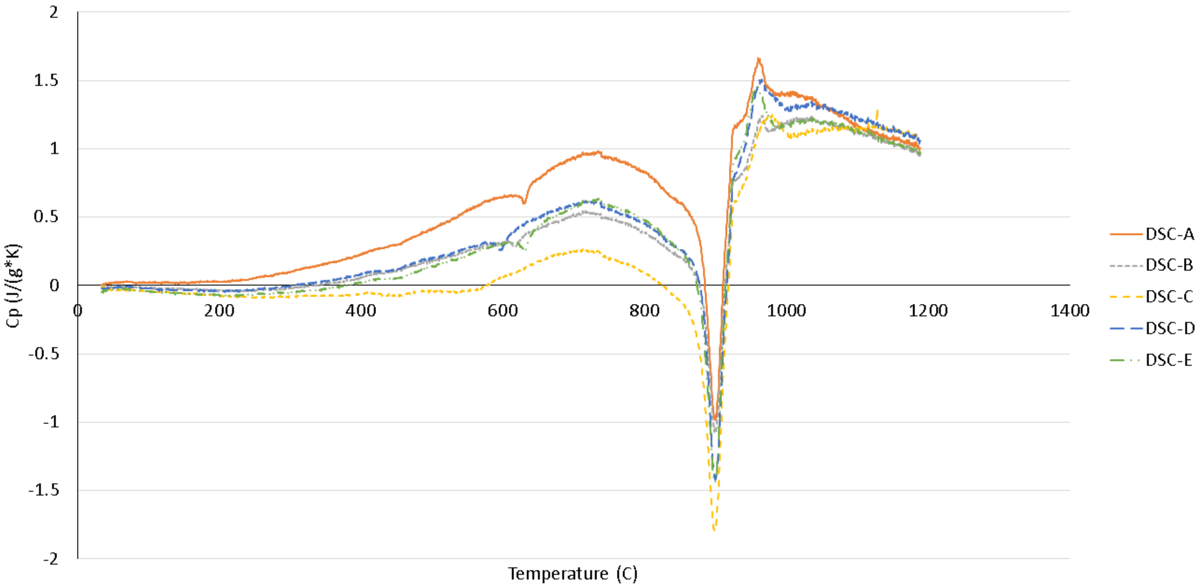

Figure E.2: Specific heat capacity (Cp) versus temperature of the compensated data

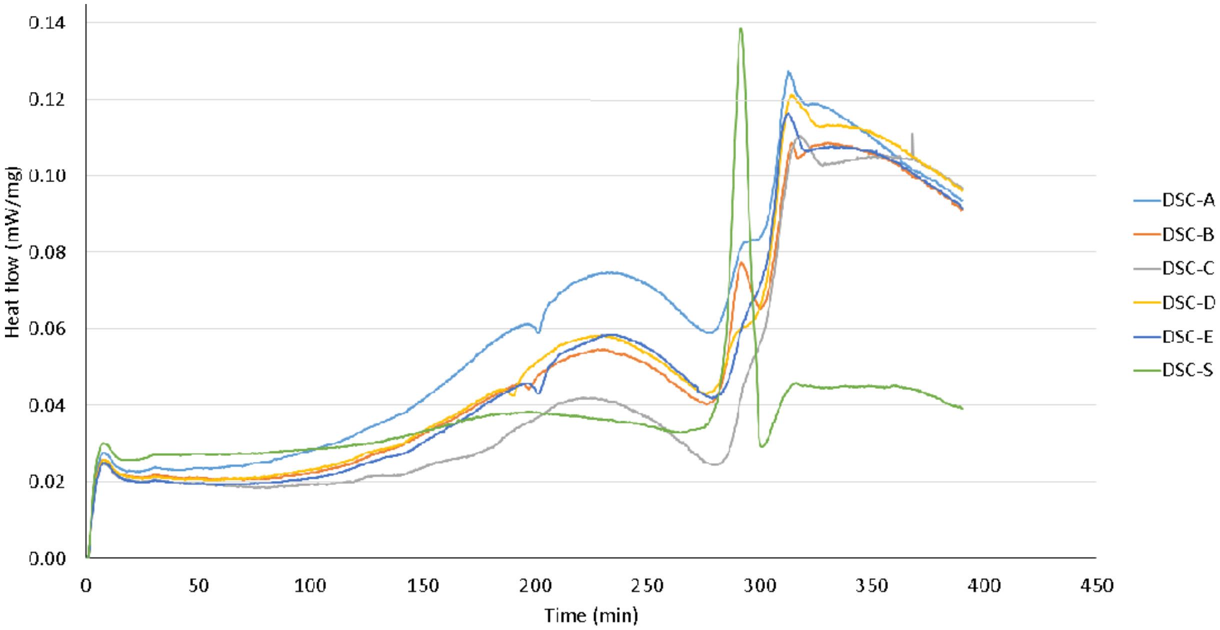

Figure E.3: Heat flow versus time of the un-compensated data

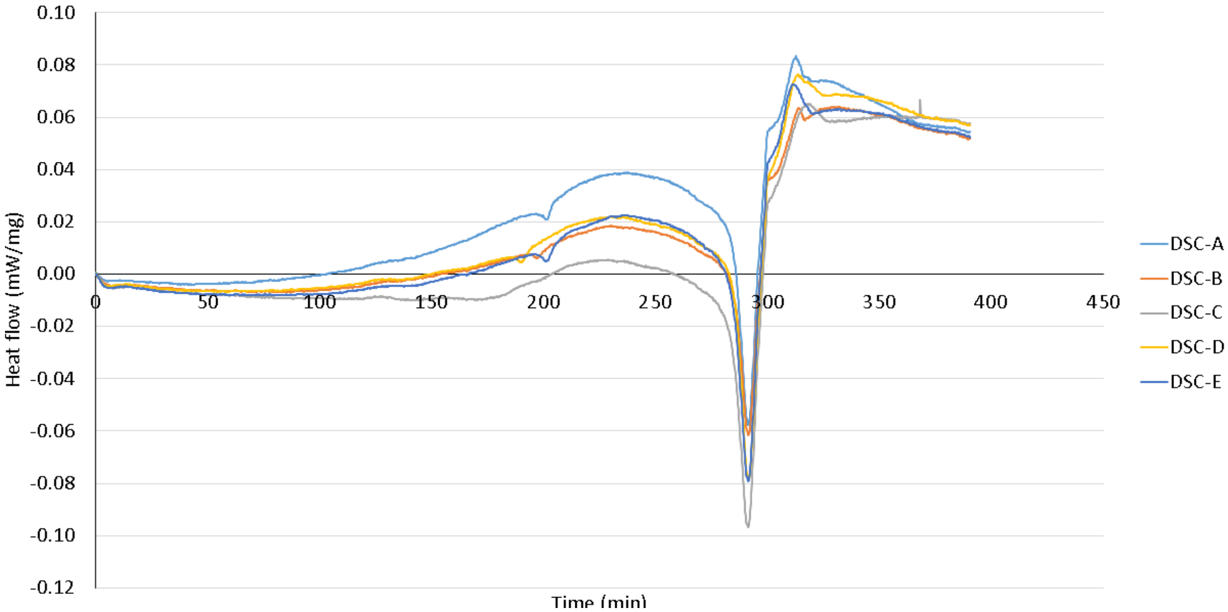

Figure E.4: Heat flow versus time of the un-compensated data

E.2 Apparent Activation Energy

Apparent activation energy versus RMSE plots for the type C, d and E powder types. The plots do not show a reasonable local minimum and were not used for the creation of MSCs.

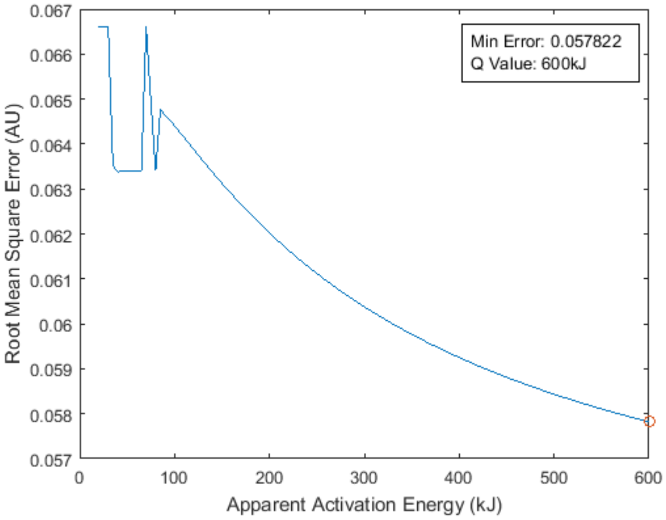

Figure E.5: Activation energy versus RMSE for the type C powder parts

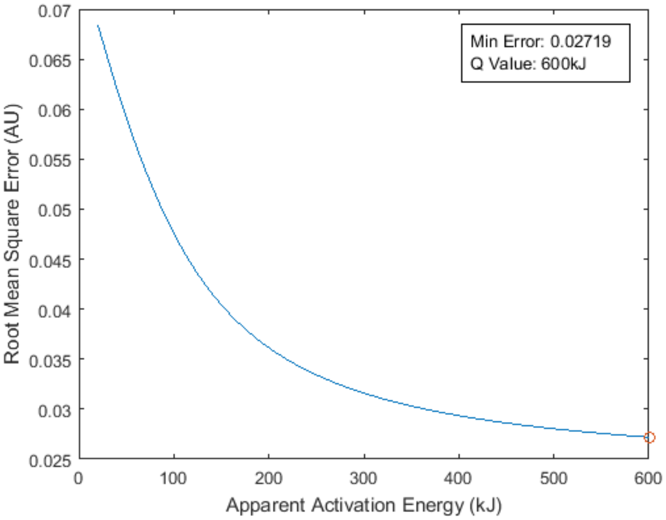

Figure E.6: Activation energy versus RMSE for the type D powder parts

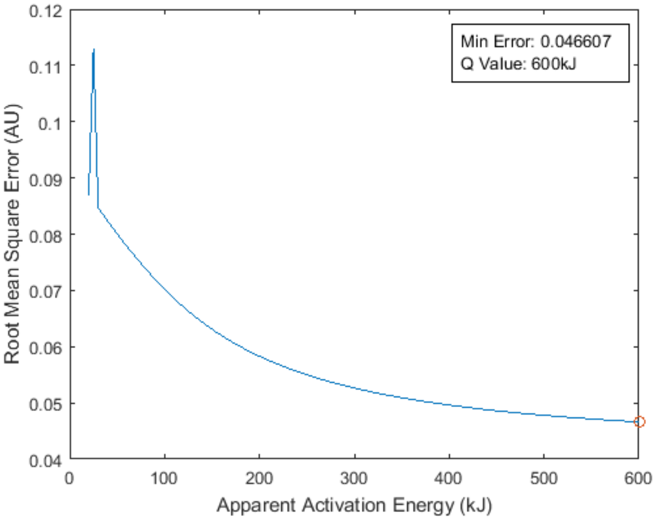

Figure E.7: Activation energy versus RMSE for the type E powder parts

Appendix F

Computed Tomography Analysis Methodology

F.1 Region of Interest Position and Size

Full sample pore and particle size analysis was not feasible on each of the 20 datasets analyzed for this study due to the computational requirements of analyzing large domains. It was determined that a region of interest (ROI) of 1.25 1.25 2.25 mm3 was the maximum size that was feasible for the study. The tall dimension was aligned with the print dimension to maximize the number of print layers contained in the domain. To have the best chance of comparing the same volume before and after part shrinkage associated with sintering, the ROIs were centered at the parts approximate center of mass. The ROIs were a consistent size across all green parts, but for each sintered part, they were shrunk proportionally to the overall part shrinkage. A representative volume analysis was performed in what was visibly determined to be the most heterogeneous dataset, CT7, in terms of pore and solid configurations. ROIs were chosen according to the above description, and ranged in size from 0.35 0.35 2.25 mm3 to 1.75 1.75 2.25 mm3. ROIs were compared in terms of bulk relative density and mean pore size. To get an understanding of how well this centrally located ROI would represent the part, an internal ROI of this size, positioned near the top of the sample, was also analyzed.

Table F.1 contains the results of all such ROI analysis. All centrally positioned ROIs, regardless of dimensions, had relative density values within 1% of the largest ROI tested. Mean pore diameter values for this set of ROIs also varied little around that of the largest ROI, staying within 1.7 m. However, when moving the ROI position towards the top of the sample, a significant increase in relative density is seen, while the mean pore diameter remains within 1 m.

Table F.1: Results from representative volume analysis on sample CT-DH (green).

ROI Name	Location Location	Dimensions (mm)	Relative Density	Mean Pore Diameter (μm)
CT-DH-92x92x592	Central	0.35 x 0.35 x 2.25	0.533	41.8
CT-DH-132x132x592	Central	0.50 x 0.50 x 2.25	0.542	41.0
CT-DH-192x192x592	Central	0.73 x 0.73 x 2.25	0.531	43.0
CT-DH-264x264x592	Central	1.00 x 1.00 x 2.25	0.531	43.0
CT-DH-330x330x592	Central	1.25 x 1.25 x 2.25	0.528	42.7
CT-DH-460x460x592	Central	1.75 x 1.75 x 2.25	0.538	42.7
CT-DH-330x330x592	Top	1.25 x 1.25 x 2.25	0.579	41.8

F.2 Pore Network Analysis

Analysis of the CT image sets consisted of finding four major parameters: relative density, particle size, pore size and sinter neck diameter. All values were found volumetrically, on a per-layer basis, with the average of those giving the overall value for the entire part.

The relative density was calculated by comparing the area of the particle space (found by segmentation), to that of the overall layer. Pore size was found by segmenting the 3D pore volume into individual pores respectively, using the watershed-based technique of pore network extraction, first described in [JH1]. The resulting networks contained pore diameter, volume, and position, as well as the diameter of constrictions (throats) between neighboring pores. Pore diameters were calculated as the maximal inscribed sphere, and throat diameters were calculated as the size of the largest sphere that could travel between neighboring pores. Particle size was found through effectively the same means as was used to find pore size, but with the reverse segmentation of the domain being used (highlighting the particles rather than the pores.

Sinter neck diameter was found by analyzing the measured constriction diameters in the resulting particle networks. A surprising result was that sinter necks were measured in the green (unsintered) parts, typically in the 0-40 m range. This is because the air-gap between two merely touching spheres stays within 2 voxels for a considerable fraction of the particle height, and therefore could easily be improperly segmented into a sinter neck. A geometric analysis of this phenomenon considering spheres of diameter 50 m and larger, resulted in the determination that any sinter neck measurements below 50 m should be treated as unreliable, as air gaps of less than 2 voxels often get lost in the segmentation process. Therefore, only sinter necks measured above 50 m were included in any reported statistics.